toward larger solute concentrations, which leads to a reduction of the supersaturation with respect to the (incoherent) equilibrium solvus line (fig. 1), and, hence, to a reduction of the driving force for precipitation.

Often only after extended aging do the metastable phases α'' and β' decompose further until the final equilibrium phases α' and β are obtained. The precipitated equilibrium phase β is then incoherent with small associated strain fields but with a rather large $\sigma_{\alpha\beta}$. Often the solute concentration in the metastable precipitate $c_p^{\beta'}$ is smaller than in the equilibrium precipitate (c_p^{β}).

THEORETICAL CONSIDERATIONS

This section will deal with theoretical considerations of the time evolution of various precipitation parameters, e.g. the mean radius $\bar{R}(t)$, the number density of precipitates $N_v(t)$, $\Delta c(t)$.

Precipitation in supersaturated metastable solid solutions is initiated via formation of stable nuclei. Within the frame-work of classical nucleation theory the nucleation rate

$$J = K_1 \cdot e^{-t_w/t} \cdot \exp - \frac{\delta G^*}{kT} \qquad (2.1)$$

is mainly controlled by the work of formation $\delta G^* = \frac{4\pi}{3} \cdot R^{*2} \cdot \sigma_{\alpha\beta}$ of a critical nucleus with radius R^*. R^* is essentially controlled by the interfacial energy $\sigma_{\alpha\beta}$ and by the supersaturation Δc (1):

$$R^* = K_2 \cdot \frac{\sigma_{\alpha\beta}}{T} \cdot \frac{1}{\ln(\Delta c + 1)} \qquad (2.2)$$

(K_1 and K_2 are constants which can be found e.g. in ref. 2; t_w is the incubation period). A nucleated spherical particle of radius R and solute concentration c_p embedded in a supersaturated matrix of mean solute concentration $\bar{c}(t)$ will grow at a rate (cf. (3))

$$\frac{dR}{dt} = \frac{\bar{c}(t) - c_R}{c_p - c_R} \cdot \frac{D}{R} \qquad (2.3)$$

(D: effective diffusivity)

The solute concentration c_R at the interphase boundary is given by Gibbs-Thomson equation:

$$c_R = c_e \cdot \exp \left\{ \frac{k_2 \cdot \sigma_{\alpha\beta}}{T} \cdot \frac{1}{R} \right\} \qquad (2.4)$$

According to equs. 2.3 and 2.4 the growth rate of a particle with radius R can be either positive, zero (for $R = R^*$ since then $c_R = \bar{c}(t)$), or negative, depending on $\bar{c}(t)$ and R.

If the nucleation rate is not too high (i.e. δG^* is sufficiently large) only a few precipitates are formed during the nucleation period thus leaving the matrix supersaturation still at a rather high level. In this case $dR/dt > 0$ for almost all particles, and the particles grow substantially by depleting the matrix according to equ. 2.3 (this precipitation stage is called "growth regime").

Once the supersaturation of the matrix has been reduced so much that the critical radius R^* becomes larger than the radius of the smaller precipitates of the particle size distribution function $f(R,t)$ established, these will then start to redissolve, i.e. $dR/dt < 0$ (the growth of larger precipitates at the expense of smaller dissolving ones is often called "coarsening" or "ripening").

In reality, particularly during the early stages of precipitation, the physical processes attributed to the three stages "nucleation, growth and coarsening" overlap. This overlap leads to rather complicated kinetics with respect to the time evolution of $\bar{R}(t)$, the particle number density $N_v(t)$, and the size distribution function $f(R,t)$.

In principle, equs. 2.1, 2.2 and 2.4 together with the continuity equation ("mass balance equation") contain the ingredients for a computation of the entire course of a precipitation reaction within the frame work of existing nucleation and growth theories. Unfortunately, the integration of these equations, which has to be carried out by considering simultaneously the continuous time evolution of the size distribution function, cannot be performed analytically.

Recently, we have solved this problem by devising an algorithm (2) which allows a numerical integration of the equations of motion. In this algorithm, termed "numerical model" (N-model), the time evolution of $f(R,t)$ is computed without any approximation. Thus, the N-model allows the time evolution of $\bar{R}(t)$, $R^*(t)$, $N_v(t)$ and $\Delta c(t)$ to be computed accurately during the entire course of precipitation.

Basically, the computations are started with the input parameters c_e, c_p and T which are usually known from the phase diagram, as well as $\sigma_{\alpha\beta}$ and D. In fact, there are two further input parameters required. However, the particular choice of these two parameters and their influence on the computed precipitation behavior is beyond the scope of this paper and not relevant to the following discussion. Details can be found in references 2, 4. Since both $\sigma_{\alpha\beta}$ and D are a priori unknown, they serve as free parameters. From a comparison of the N-model with experimental kinetic data, $\sigma_{\alpha\beta}$ and D can be determined rather accurately. This is demonstrated in the next section.

KINETICS OF PRECIPITATION - COMPARISON BETWEEN N-MODEL AND EXPERIMENTAL DATA

Cu-1.9 at%Ti aged at 350 °C.

Fig. 2 and fig. 3 show the time variation of the precipitate number density N_v and the mean radius $\bar{R}$ for Cu-1.9 at% Ti isothermally aged at 350°C (c_0 = 1.9 at%, c_e = 0.22 at% Ti, c_p = 20 at% Ti). The experimental data which were obtained from a FIM study (5) are compared with the predictions from the N-model. The experimental data points are well described by the N-model for adjusted D and $\sigma_{\alpha\beta}$ values of 2.5 x 10^{-15} cm^2/sec and 0.067 J/m^2, respectively. D and $\sigma_{\alpha\beta}$ were determined from a comparison of the experimental data with the computed ones using the following procedures:

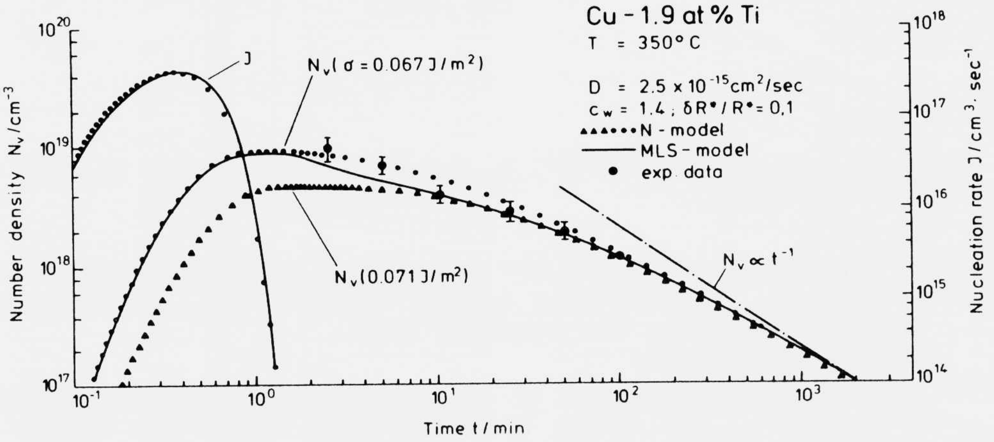

Fig. 2: Variation of N_v and of J with aging time for Cu-1.9 at%Ti as computed with the N-model and the MLS-model for $\sigma_{\alpha\beta}$ = 0.067 J/m^2; for this value of $\sigma_{\alpha\beta}$ the computed $N_v(t)$-curve agrees well with the experimental data; poor agreement is obtained for $\sigma_{\alpha\beta}$ = 0.071 J/m^2. The MLS-model which is not explained in this paper can be found in ref. (2).

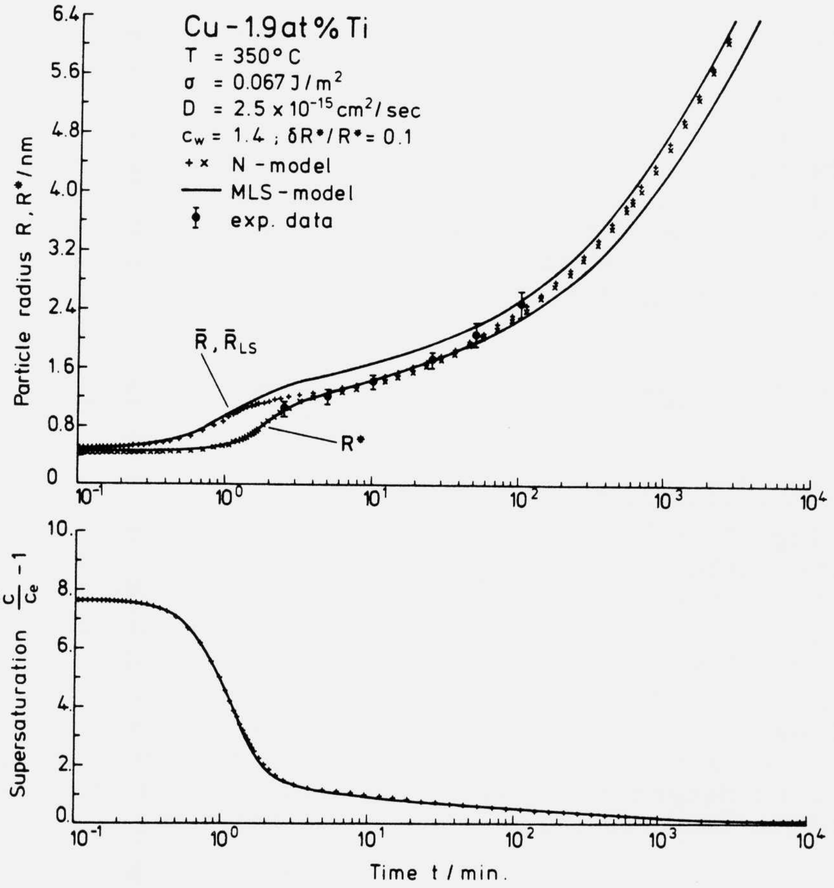

Fig. 3: Variation of R, R*, R_{LS} and of the relative supersaturation.

i) $\sigma_{\alpha\beta}$ is varied until the calculated maximum number density $N_{v,max}$ occuring during the whole precipitation reaction equals the measured one.
In a second step
ii) D can be determined by shifting the calculated curves $N_v(\log t)$ and $\bar{R}(\log t)$ until they match the corresponding experimental curves (2, 4).

The N-model also predicts the time evolution of the nucleation rate J(t) (fig. 2) and both the critical radius R*(t) and the supersaturation Δc (fig. 3) as well as the particle size distribution function (to be found in ref.2). Thus, the general course of the precipitation reaction can be described as follows: During the early nucleation period ($t \lesssim 0.5$ min) both J and N_v increase, whereas Δc and, hence,

R^* (equ. 2.2) remain roughly constant. At this stage the size distribution function $f(R,t)$ is very narrow. Since c_R is still close to $\bar{c} \approx c_0$, the growth rate (equ. 2.3) of nucleated precipitates is also close to zero, i.e. $\bar{R}$ remains about constant. After $t \gtrsim 0.5$ min those precipitates nucleated first become considerably larger than R^* and $f(R,t)$ becomes much broader. This is the beginning of the growth period which is characterized by -i) the largest growth rate ever observed during the course of precipitation; -ii) a ratio $\bar{R}/R^*$ which becomes significantly larger than 1; -iii) the maximum number density ($N_{v,max}$) of particles which remains about constant; -iv) an enforced decrease of Δc and consequently -v) a decrease of J from its maximum value; for this alloy, J never reaches its steady state value. At the end of the growth regime ($t \approx 1.2$ min) the supersaturation has dropped significantly and $\bar{R}$ grows rather slowly. This effect causes R^* to converge towards $\bar{R}$ as well as to make $dN_v/dt < 0$. During the subsequent transition period ($t \gtrsim 1.2$ min), the growth rate of $\bar{R}$ is primarily controlled by the dissolution of particles with $R < R^*$ and only to a lesser extent by the uptake of solute atoms from the matrix, the supersaturation of which is still about 20 %.

In modern theories of the kinetics of first order phase transitions, it is usual to express the growth of the solute clusters or precipitates in the form of power-laws $\bar{R} \sim t^a$ with the exponent $a = a(t)$ being time dependent. In fig. 4 $a(t) = \frac{\partial \ln\bar{R}}{\partial \ln t}$ is plotted versus t for Cu-1.9 at%Ti. It is evident that the largest time exponent ($a = 0.5$, recalling the parabolic growth law derived by Aaron et al. (3) under some special assumptions; for more details, see ref. 2) is found during the growth regime, although only for a time span of about 0.8 min. At the end of the growth regime $a(t)$ drops to small values. Then $a(t)$ increases again during the extended transition regime and approaches asymptotically ($t \gtrsim 4 \cdot 10^4$ min/350°C) its final value $a = 1/3$. Only at this stage do the kinetics follow the well known $\bar{R} \propto t^{1/3}$ growth law derived by Lifshitz and Slyozov (6) and by Wagner (7) for the asymptotic behaviour ($t \to \infty$; $\Delta c \to o$) of the coarsening reaction (LSW-theory).

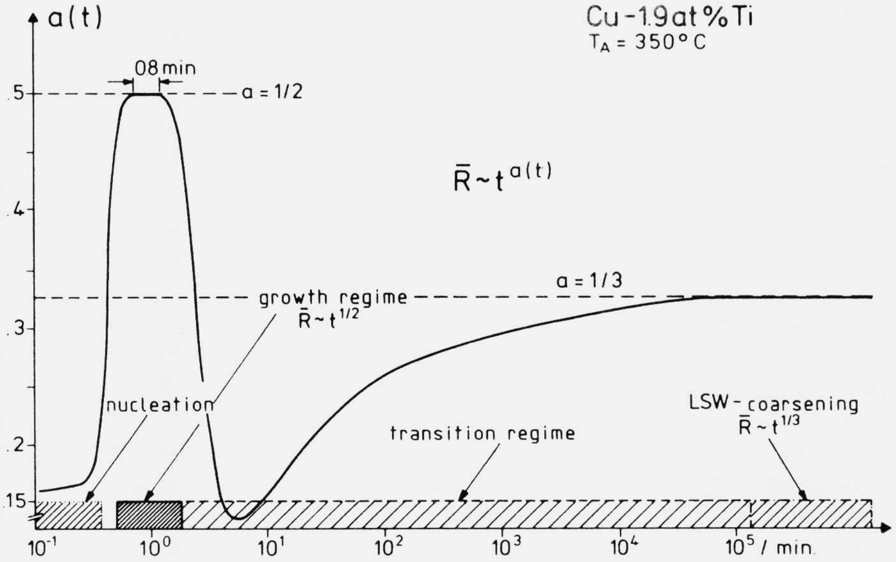

Fig. 4: Variation of the exponent $a = \frac{\partial \ln R}{\partial \ln t}$ with aging time at 350°C in Cu-1.9 at%Ti.

We have analyzed experimental kinetic data from a variety of different two- phase alloys in terms of the N-model. Table 1 presents the interfacial energies $\sigma_{\alpha\beta}$ together with the width of the (coherent) miscibility gap for each given alloy. It is evident that there is a pronounced correlation between $\sigma_{\alpha\beta}$ and the gap width, i.e. the larger the width of the gap, the larger is $\sigma_{\alpha\beta}$.

Table 1: CORRELATION BETWEEN THE WIDTH OF THE MISCIBILITY GAP AND THE COHERENT INTERFACIAL ENERGIES $\sigma_{\alpha\beta}$

Alloy at%		Aging temperature °C	Composition/type of precipitates	Width of coherent miscibility gap at%	Coherent interfacial energy $\sigma_{\alpha\beta}$ J/m²
Ni-14 Al	[1]	550	γ'Ni_3Al	~ 15	~ 0.016
Ni-36 Cu-9 Al	[2]	550	γ'-$(Cu\ Ni)_3Al$	~ 20	~ 0.052
		540	not-determined	~ 20	~ 0.050
		580	not-determined	~ 20	~ 0.052
Cu-1.9 Ti	[3]	350	β'-Cu_4Ti	~ 20	~ 0.067
Cu-2.7 Ti	[4]	350	β'-Cu_4Ti	~ 20	~ 0.067
Cu-1.5 Co	[5]	500	> 95 at% Co	~ 95	~ 0.171
Fe-1.4 Cu	[6]	400, 500	> 98 at% Cu	≈ 100	~ 0.250
Fe-0.64 Cu	[6]	400	> 98 at% Cu	≈ 100	~ 0.250

[1] Wendt und Haasen, 1983 (FIM)

[2] Liu und Wagner, 1984 (FIM)

[3] v. Alvensleben und Wagner, 1984 (FIM, TEM)

[4] Eckerlebe, Kampmann und Wagner, 1985 (SANS)

[5] Gust, Kampmann et al., 1986 (magnet.)

[6] Kampmann, 1986 (SANS)

Fe-1.38 at%Cu aged at 500 °C.

Experimental data concerning the evolution of the size distribution $f(R,t)$, the mean size $\bar{R}(t)$ and the number density of Cu enriched clusters in supersaturated Fe-1.38 at%Cu during isothermal aging at 500 °C were obtained from both nuclear and magnetic small angle neutron scattering [8]. The data for $N_V(t)$ and $\bar{R}(t)$ are shown (full dots) in Fig. 5.

Prior to an interpretation of the experimental kinetic data in terms of the N-model, we calculated both the coherent and incoherent equilibrium solubilities of Cu in Fe, as well as the coherent and incoherent interfacial energies (σ_{coh} = 0.27 J/m²; σ_{inc} = 0.50 J/m²) for bcc and fcc Cu-particles, respectively. (These data - c_e^{coh}, c_e^{inc}, σ_{coh}, σ_{inc} - have been obtained from thermodynamic analyses which were based on free energy calculations for the Fe-Cu phase diagram by Kubaschewski [9].)

It is well known that the Cu-particles nucleate in the α-iron matrix as coherent clusters with a bcc structure and - as we have established by TEM - only once they have grown to radii R ~ 2.8 nm they transform into their equilibrium fcc structure though by losing coherency. For an interpretation of the experimental data, the bcc → fcc structural transformation has to be incorporated into the N-model. This is accounted for by replacing in equ. 2.4 and 2.3 c_e^{coh} and $\sigma_{\alpha\beta}^{coh}$ through c_e^{inc} and $\sigma_{\alpha\beta}^{inc}$ for those particles of the size distribution which have grown beyond the transformation radius. As is shown in Fig. 5a, consideration of the structural transformation (full lines) leads to a momentary acceleration of the precipitation kinetics with reference to a computation where the transformation is disregarded (dashed curves in Fig. 5a).

According to Fig. 5a nucleation is finished after about 15 min; at this stage, $\bar{R}$ is still smaller than 0.6 nm. After the nucleation period the precipitates grow essentially by depleting the still highly supersaturated matrix (up to $\bar{R} \approx 0.8$ nm after 30 min). By inspection of the time evalution of $N_V(t)$ and $\bar{R}(t)$ displayed in Fig. 5a, it becomes evident that theory predicts a significantly slower transition to the coarsening regime beyond t = 30 min than has been observed experimentally even though the bcc → fcc transformation was taken into account in the computations. As the numerical simulation describes correctly the decomposition kinetics without limiting assumptions with respect to the mathematical treatment, we had to conclude that the discrepancy between the theory and experiment results from

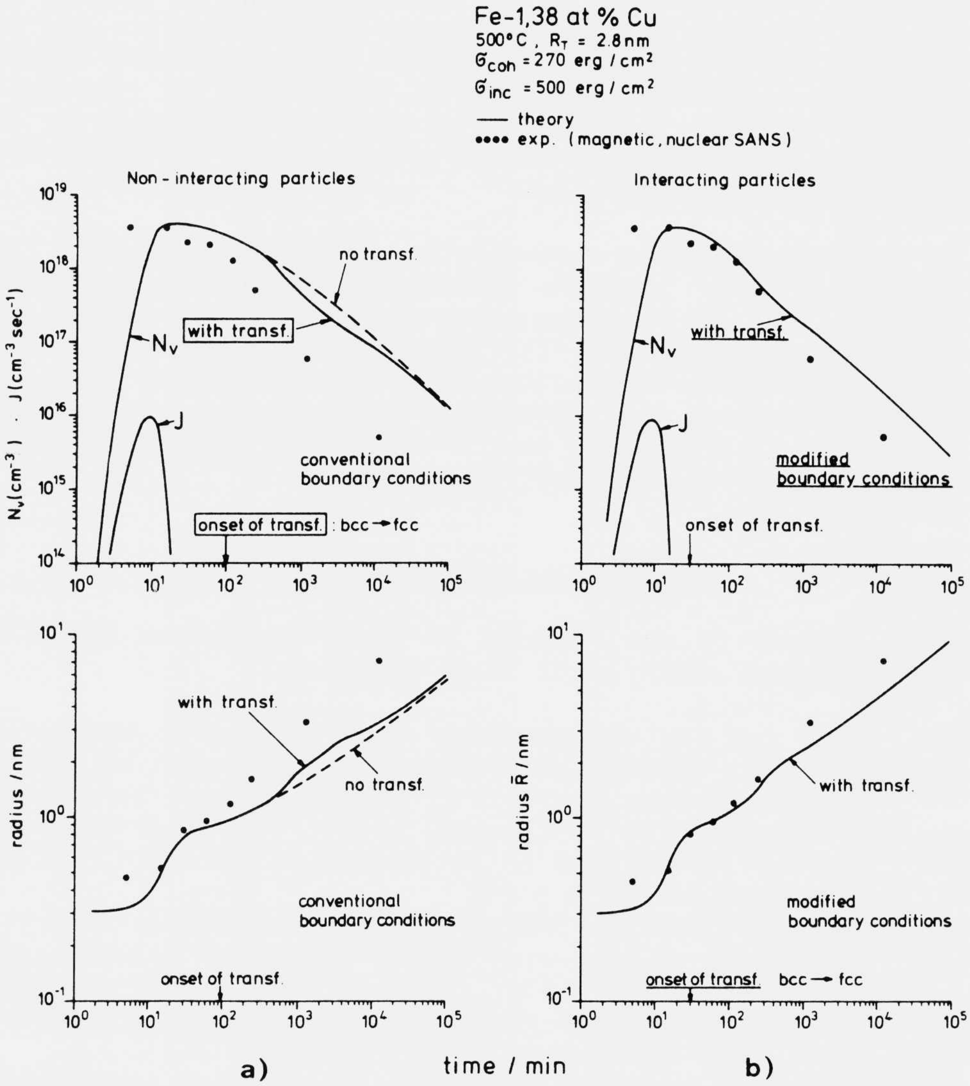

Fig. 5: Time evolution of N_v, J and $\bar{R}$ during decomposition of Fe-1.38 at%Cu at 500 °C.

a) Computations without accounting for mutual particle interactions. The full curves are the predicted kinetics if the loss of coherency at the onset of the bcc → fcc transformation is considered.

c) Computions with modified boundary conditions accounting for both particle interaction and bcc → fcc transformation.

the fact that there is a rather strong interaction amongst adjacent copper particles in the Fe-Cu system which, in fact, is not considered in the theory outlined in section 2. We have recently incorporated this interaction into the N-model by an appropriate modification of the boundary conditions which are necessary for an integration of the equations of motion. As is shown in Fig. 5b, consideration of the particle interaction yields a much better agreement between theory and experiment.

In essence, with reference to the original N-model, the consideration of particle interaction yields the following results: -i) the decomposition kinetics become faster (as revealed by Fig. 5b), -ii) during later aging stages the size distribution of the particles becomes broader than the one predicted by the LSW-theory, and -iii) $\bar{R}$ is still found to coarsen in proportion to $t^{1/3}$ but with a higher rate constant than for non-interacting particles.

SOME STILL OPEN QUESTIONS

With respect to the kinetics of phase separation, quite a few questions remain still to be answered:

i) What are the decomposition kinetics during the early stages in heavily supersaturated alloys for which δG^* becomes smaller than ~ 5 kT (the so-called "non-linear spinodal regime")? (In ref. (2) it was shown that the N-model is confined to metastable alloys with nucleation barriers $\delta G^* \geqq 5$ kT.)

ii) Why are different precipitate microstructures observed in similar alloys with almost identical precipitated volume fractions (e.g. isolated precipitates in CuNi-Al, interconnected "mottled" structures in CuNi-Cr, 'modulated' structures in CuNi-Fe [10]?

iii) Why are the coarsening kinetics for mottled and modulated structures more sluggish? (Frequently $\langle R\rangle \sim t^{1/4}$ is observed rather than $\langle R\rangle \sim t^{1/3}$ as for spherical randomly distributed precipitates.)

REFERENCES

1. K.C. Russel, in "Phase Tranformations", Ch. 6, ASM Metals Park, Ohio, 1970, p. 219.

2. R. Kampmann and R., Wagner, in "Decomposition of Alloys: the early stages". Eds. P. Haasen, V. Gerold, R. Wagner and M.F. Ashby. Pergamon Press 1983, p. 91.

3. H.B. Aaron, D. Fainstain and G.R. Kotler, J. Appl. Phys. 41, 1970, p. 4404.

4. R. Kampmann, H., Eckerlebe and R. Wagner, in: Proc. of the Materials Research Society Symposa, Volume 57, Boston 1985, p. 525 - 542.

5. L. v. Alvensleben and R. Wagner, see Ref. 2, p. 143.

6. I.M. Lifshitz and V. V. Slyozow, Phys. Chem. Sol., 19, 1961, p. 35.

7. C. Wagner, Z., Elektrochem. 65, 1961, p. 581.

8. R. Kampmann and R. Wagner, in: Atomic Transport and Defects in Metals by Neutron Scattering, Eds. C. Janot, W. Petry, D. Richter and T. Springer, Berlin: Springer-Verlag, 1986, p. 73.

9. O. Kubaschewsky, J.F. Smith and D.M. Bailey, Z. Metallkde. 68, 495 (1977).

10. R. Wagner, R. Kampmann, B. Jiang and P.A. Beaven, in: Proc. Int. Conf. Cu '86-Copper Tomorrow-Technology-*Products* Research. Edit. S. Ceresara, Barga di Lucca, Italy, 1988. In the press.

DESIGN OF M_2C CARBIDES FOR SECONDARY HARDENING

MICA GRUJICIC
Department of Materials Science and Engineering
Massachusetts Institute of Technology, Cambridge
Massachusetts 02139

1. INTRODUCTION

High Co-Ni secondary hardening steels exhibit outstanding combination of strength and toughness. The first steels of this kind to be developed were HP94X steels followed by HY180(1) and AF1410(2). Table 1 lists typical compositions and mechanical properties. A high strength to toughness ratio can be achieved only if the lath-martensitic dislocation substructure is retained at normal aging temperatures (480-550°C) thus ensuring a fine dispersion of alloy carbides is formed during secondary hardening. The highly dislocated substructure of the matrix provides an abundance of preferred nucleation sites, favoring a heterogeneous model of carbide formation. It is also possible, however, that high recovery resistance (low rate of dislocation climb) helps carbide particles maintain their fine size.

The final heat treatment of steels of this class which ensures a good combination of strength and toughness entails a high temperature tempering (480-510°C) for a few hours. As a result a transient cementite phase precipitated early during the tempering is completely dissolved and the fracture toughness is thereby improved. Simultaneously, however, the material suffers a loss in strength due to overaging of M_2C. Aging is quite fast in these alloys; for instance, at 510°C, AF1410 reaches maximum hardness after 15min. Hence, when designing M_2C to maximize material strength, one should follow principles for particle strengthening of overaged materials. These principles have been discussed in Section 2. Alloy design of multicomponent systems such as Fe-Co-Ni-Cr-Mo-C, (base system for steels listed in Table 1), is still empirical, but guided by phase diagram informations. While the behavior of alloying elements in simple ternary systems is generally well understood the extensive interactions between elements in a multicomponent system makes the

TABLE 1

Nominal compositions and Mechanical Properties of Ultra-High Strength Steels

Alloy	C	Co	Ni	Mo	Cr	YS, ksi	K_{IC},ksi/in.
HP 9-4-20	0.20	4	9	1	1	175	-120
HY180	0.10	8	10	1	2	180	-230
AF1410	0.16	14	10	1	2	230	-190
SRG1	0.25	14	10	4	0		

role of each of them, in promoting good combination of strength and toughness, unclear. Often the role of an element depends on its amount and the amounts of other elements in the alloy. In Section 3 we present a brief summary of experimental findings regarding the roles of different elements in major phase equilibria in these alloys.

Precipitation of M_2C carbide is not the only reaction taking place in the course of tempering for secondary hardening. Several other reactions (cementite precipitation and ultimate dissolution, precipitation of competing phases, etc.) occur prior to or concurrently with the formation of M_2C. In Section 4 we present a detail thermodynamic analysis of these basic reactions, while taking into consideration their para- or coherent equilibrium character where appropriate. This analysis was done using the THERMOCALC computer program and database for computation of phase equilibria in multicomponent systems (3).

2. DESIGN PRINCIPLES

As mentioned earlier, a typical heat treatment designed to optimize the strength to toughness ratio, is associated with an overaged condition of the strengthening M_2C dispersion. According to theories of particle strengthening (see for example Argon (4)), the strength of an overaged material is inversely proportional to an average particle spacing, or equivalently it scales with $\sqrt{f}/r$ where f is the particle volume fraction and r is the particle size. When designing M_2C carbides for secondary hardening one should thus strive for finest, closely spaced dispersion of strengthening particles. This can be achieved by increasing the driving force for nucleation, which in turn is achieved by increasing the supersaturation. A large driving force gives rise to large nucleation rate and in turn to large particle number density. According to theories of precipitation hardening, peak strength corresponding to the underage/overage transition, occurs at a fixed particle size. Hence, a larger particle number density, gives rise to a higher peak strength ensuring a higher strength in the overaged condition.

An additional benefit of a larger driving force for nucleation of the strengthening phase is a smaller nucleus size. According to the theories of phase transformations in highly supersaturated systems (5,6) such as the systems at hand, smaller nucleus size guarantees a smaller particle size after aging. This in turn ensures that the particle size in an overaged material is closer to the critical particle size associated with peak strength.

Another aspect of fine dispersions of M_2C at the end of aging treatment pertains to the control of the rate of coarsening of this phase. According to the theories of phase transformations in systems with large supersaturations it is the kinetics of coarsening rather than of diffusional growth which dominates the kinetics of the overall particle growth. While designing M_2C phase then one should also consider optimizing its composition to give a higher coarsening resistance.

As mentioned earlier, it is the dissolution of cementite which necessitates prolonged tempering treatment. If alloys with cementite of lower stability could be designed they would require shorter times for its complete dissolution, and consquently give rise to desirable smaller particle size of the M_2C strengthening phase at the end of aging treatment.

3. CHEMISTRY OF ULTRA-HIGH STRENGTH STEELS

As shown in Table 1 the major alloying elements in steels of this class are Ni,Co,Cr,Mo and C. Here we discuss the alloy design concepts which have led to additions of each of these elements.

Addition of 10wt% of nickel has been found to be important for lowering the ductile-to-brittle transition temperature although this is not always accompanied by a higher notch ductility (1).

It is believed that the most important role of cobalt is to retard the recovery of the martensitic dislocation substructure and the lath martensite during aging, thus ensuring a fine dispersion of secondary hardening precipitates. When accompanied by 10wt% Ni, Co is an effective solid solution hardener provided it is present in excess of 8wt%. At lower level of cobalt, 4wt% and less and in the presence of 10wt% of nickel, an increase in cobalt content gives rise to an anomalous decrease in hardness and yield strength. Cobalt lowers the hardenability. It increases M_s temperature but does not lower the amount of twinned martensite, an undesirable microstructural constituent. In the absence of Ni, Co addition to Fe-Mo-C alloy has been found to inhibit secondary precipitation of Mo_2C and to enhance interlath cementite precipitation (7). This in turn has been shown to give rise to a significant deterioration in tensile ductility and fracture toughness in these alloys.

Molybdenum additions give rise to solution strengthening, increased hardenability and apparent retardation of temper embrittlement. Yet, in steels of this class the major role of molybdenum is in promoting secondary hardening reactions in which alloy M_2C carbides are formed.

Chromimum is generally added to increase hardenability and for solid solution strengthening. While being a moderate carbide former, its role appears to be quite important regarding the precipitation of fine scale M_2C carbides and increasing its relative stability relative to other carbides M_6C, $M_{23}C_6$, etc. There is evidence (7) that Cr promotes the formation of interlath austenite, giving rise to an enhanced toughness. It also accelerates the aging kinetics shifting the hardness peak associated with secondary hardening towards lower temperatures and shorter times. When replacing Mo, at the same level of other alloy additions, Cr lowers the solutionizing temperature.

Carbon is an effective interstitial solution strengthener, which decreases the M_s temperature, and increases the amounts of retained austenite and twinned martensite. The latter is quite detrimental to toughness properties. Increased carbon give rise to a higher volume fraction of the secondary hardening dispersion. However, a carbon addition much in excess of 0.2 wt%, is detrimental to weldability.

4. THERMODYNAMICS OF ULTRA-HIGH STRENGTH STEELS

Figure 1, reproduced from Little et al. [8], shows an isochronal (5hrs) tempering behavior of AF1410 steel. In it the various stages of phase evolution during tempering, are delineated. This behavior is characteristic of steels of this class.

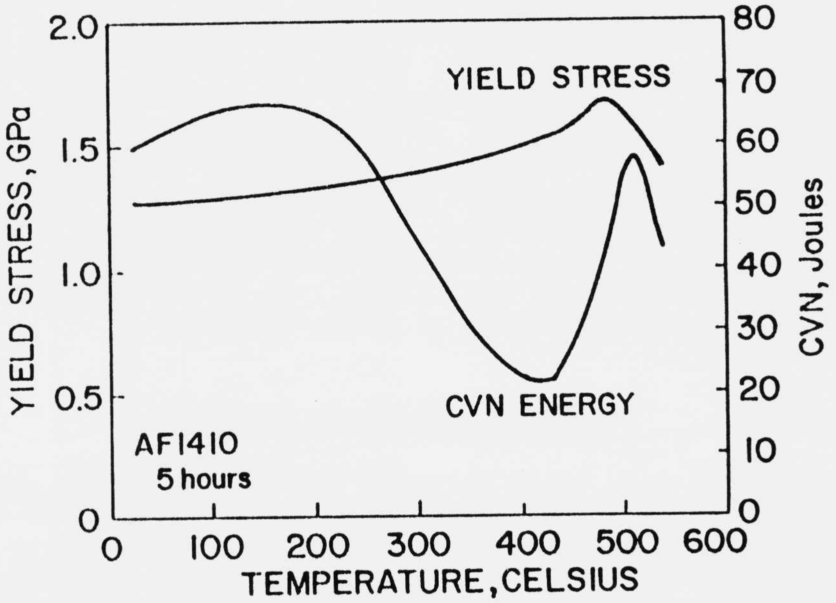

Fig. 1 Isochronal (5hrs) tempering behavior of the standard AF1410 Steel

Tempering at temperatures up to ~200°C produces an increase in yield strength and notch toughness. This is believed to be due to a fine scale precipitation of cementite, most likely involving solely carbon long-range diffusion (paraequilibrium transformation mode). Further growth and coarsening of cementite particles at temperatures, between 300 and 430°C results in a continued increase in yield stress and a pronounced degradation in notch toughness and tensile ductility. The peak in tensile strength, accompanied by a substantial recovery and an ultimate peak in notch toughness in the range between 450 and 510°C is associated with a fine scale precipitation of coherent M_2C carbides, at the expense of cementite which redissolves. Improved toughness in this region is probably due to interlath precipitation of austenite.

High temperature treatment above ~540°C is characterized by a simultaneous deterioration in both strength and toughness, as a result of overaging of the M_2C carbide, which is gradually replaced by more stable competing phases, $M_{23}C_6$, M_6C and austenite.

Some of the basic reactions mentioned above take place during an isothermal treatment such as the conventional heat treatment for AF1410, 5hr/510°C, designed to give an "optimum" combination of strength and toughness. While the empirical approach to alloy design commonly practiced nowadays might result in some additional enhancement in strength and toughness, it is clear that the development of a new class of ultra-high strength steels with a superior combination of strength and toughness must start with a study of reactions discussed above, which underlie the structure/property relationship in steels of this class. In the following we present a thermodynamic analysis of these reactions.

5. PRECIPITATION OF CEMENTITE

It has been shown recently [9] that cementite which forms early during secondary hardening treatment has a metal alloy content which is identical to that of the alloy, indicating that this cementite precipitation reaction relies solely on the redistribution of carbon (paraequilibrium mode of transformation). It is not clear yet whether this reaction goes to completion before measurable alloy partitioning takes place or before M_2C nucleation sets in. Whichever is the case, it is clear that this reaction causes a significant reduction in carbon content in the matrix, giving rise, as shown in figure 2, to a reduction in driving force for nucleation of the M_2C phase, which is responsible for strengthening. As discussed in Section 2, this driving force is an essential parameter, controlling particle size and number density of M_2C particles, and should in principle be maximized. The problem of carbon depletion in ferrite due to paraequilibrium precipitation of cementite, has been recently analyzed by Grujicic [10]. The solid circles in figure 2 correspond to the carbon content of ferrite in paraequilibrium with cementite. The open circles in figure 2 correspond to the nominal carbon content of the three steels. It is seen that the effect of cementite precipitation is very important, causing the M_2C driving force to drop as much as 35%. This drop is somewhat smaller in chromium free SRG1 steel, suggesting that replacing chromium with molybdenum is beneficial. Such a composition change would also affect the kinetics of the cementite dissolution reaction which has to be brought to completion during aging to achieve the desired toughness. Chromium is a more effective cementite stabilizing element than molybdenum and has higher diffusivity in ferrite, suggesting that the extent of alloy partitioning to cementite should be higher in chrominum containing (HY180 and AF1410) steel than in chrominum free (SRG1) steel. Effective Cr/Mo diffusivity in HY180 and AF1410 is about 2.5 times larger than Mo diffusivity in SRG1 [9].

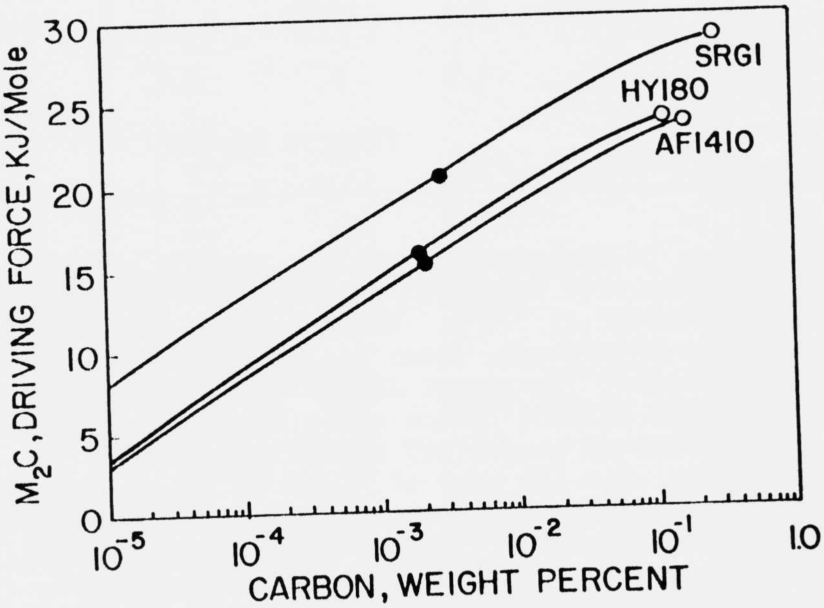

Fig. 2 Effect of carbon content on the driving force for nucleation of M_2C phase from supersaturated ferrite in three ultra-high strength steels, (Table 1). Open circles refer to nominal carbon contents, while full circles refer to the carbon contents set by a ferrite/cementite paraequilibrium.

6. PRECIPITATION OF M_2C

As mentioned earlier, high strength in steels of this class is achieved through fine scale precipitation of M_2C phase. As shown in Table 2, M_2C phase is not the only equilibrium precipitate phase at 510°C, the typical

TABLE 2

Phase Equilibrium at 510°C in three ultra-high strength steels

	PHASE MOLE PERCENT			
	M_2C	$M_{23}C_6$	M_6C	Austenite
HY180	0	1.6	.7	19.3
AF1410	0.4	2.6	.1	16.7
SRG1	4.2	0	2.9	15.2
	FERRITE BALANCE			

temperature of secondary hardening. $M_{23}CC_6$ and M_6C, and austenite are also present. In fact, in HY180, M_2C is an metastable phase at 510°C. Nevertheless, it is well estabished that this phase, forms and grows to a volume fraction of few percents, (an amount larger than the equilibrium amount for HY180 and AF1410) before other phases (with the exception of parequilibirum cementite) can be observed. This can be rationalized with the help of Figure 3, which shows the driving force for nucleation of various carbide phases from supersaturated ferrite. M_2C is the phase with the largest driving force for precipitation. The corresponding driving force for the separation of austenite, not shown in figure 3 is smaller ranging from 2.7 in HY180 to 3.2 KJ/mole in SRG1.

Fine scale M_2C precipitates are believed to be coherent and this has to be taken into account when considering thermodynamic equilibria envolving this phase. Recently Grujicic et al. (11) have developed a model for coherent phase equilibrium in multicomponent systems, which was then applied to the steels of interest here. Figure 3 shows that as a result of the coherent strain energy the driving force for nucleation of M_2C phase has been significantly lowered, and becomes more comparable with the driving forces for nucleation of other carbide phases. Owing to their complex structure, which cannot easily be related to ferrite, these other carbides phases precipitate exclusively incoherently.

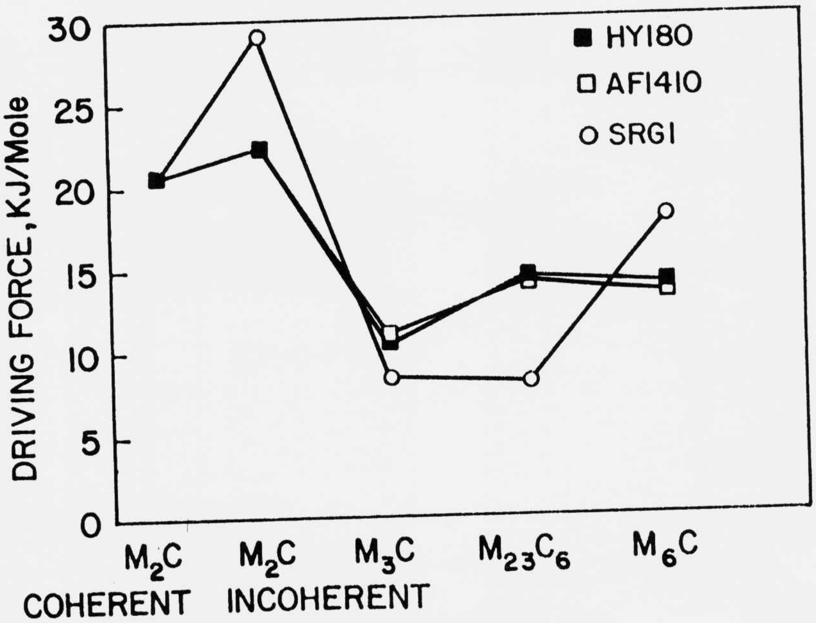

Fig. 3 Comparison of the driving force for nucleation of various carbide phases from supersaturated ferrite in the three ultra-high strength steels

Since, in general, incoherent interfaces are associated with larger energies, nucleation of incoherent phases is more difficult than that of coherent phases, at comparable driving forces.

As discussed in the previous section a complete or partial substitution of chromium by molybdenum can be beneficial. Figure 4, shows the effect of such a substitution the driving force for nucleation of incoherent M_2C phase. In Figures 4-6, increase in weight percent of Mo from zero to 4 along x-axis is accompanied by a simultaneous decrease in Cr weight percent from 2.2 to zero. In the case of alloy Fe-14Co-10Ni-.25C-Mo-Cr these Cr and Mo additions correspond to a 2:1 atomic ratio of chromium plus molybdenum to carbon, the same ratio as in M_2C phase. Figure 4 suggests that a complete chromium substitution with molybdenum is preferred because if results in a higher M_2C driving force. It should be also noticed that an increase of carbon content from .16 to .25 wt% does not have any significant effect on the driving force, while increasing the Co between 8 and 14 wt% decreases slightly the driving force at any chromium or molybdenum level.

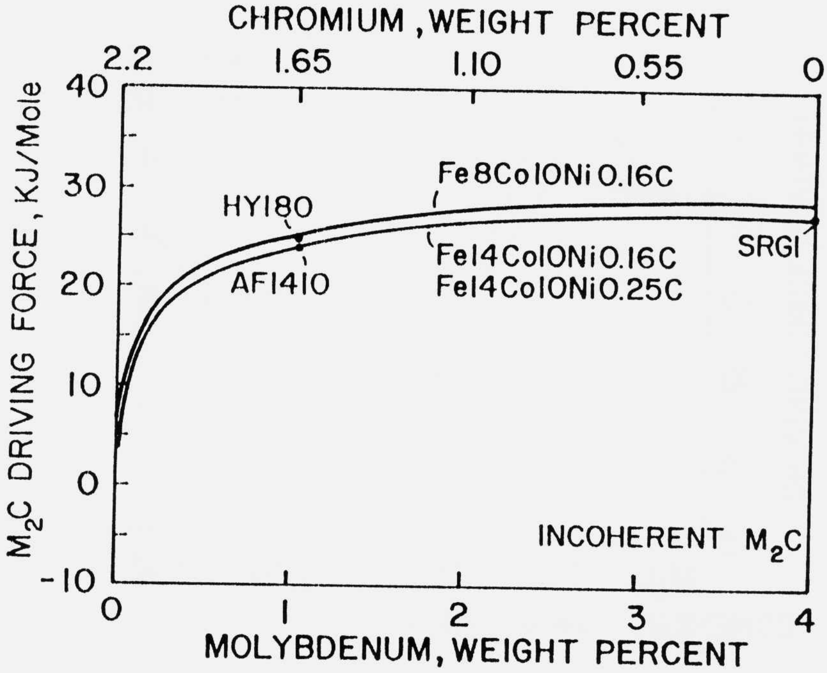

Fig. 4 Effect of additions of Co, C, Cr and Mo on the driving force for precipitation of incoherent M_2C phase. Solid point refer to the three ultra-high strength steels.

Similar conclusions regarding the effect of carbon and cobalt can be drawn in the case of the precipitation of a coherent M_2C phase, Figure 5. Here, however, there is an optimum combination of Cr and Mo which gives rise to a maximum driv ing force. It is also worth noting that, despite the different chemistry, in all three steels, HY180, AF1410 and SRG1, the driving forces for coherent M_2C nucleation are very similar.

The strength level achieved through coherent precipitation of M_2C carbides is directly related to the mole fraction of this phase. The mole fraction of coherent M_2C formed in the three steels is shown as a function of the chromium and molybdenum contents in Figure 6. The mole fraction of M_2C is most sensitive to the amount of carbon in the alloy and does not var much with cobalt, chromimum or molybdenum additions within the limits marked in Figure 6.

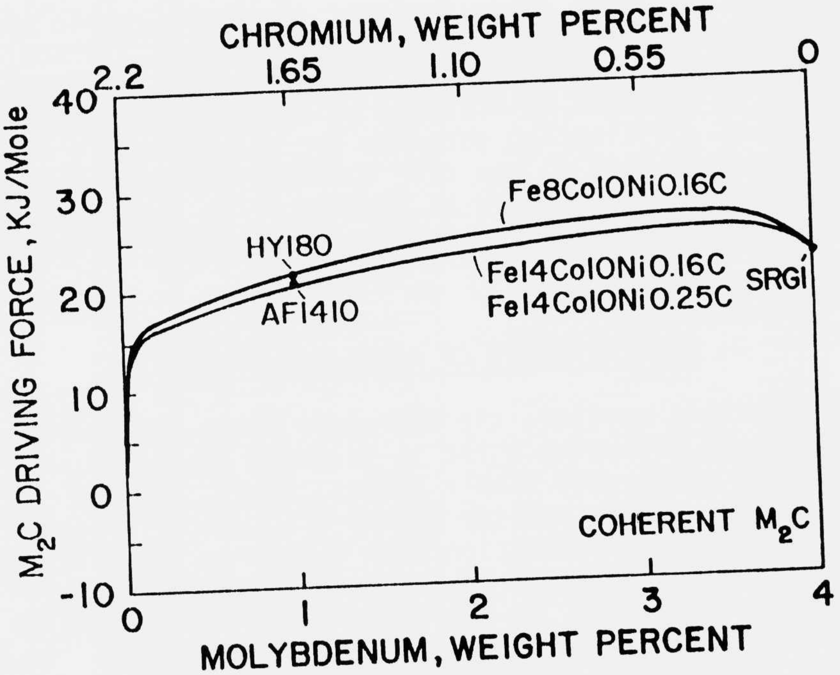

Fig. 5 Effect of additions of Co, C, Cr and Mo on the driving force for precipitation of coherent M_2C phase

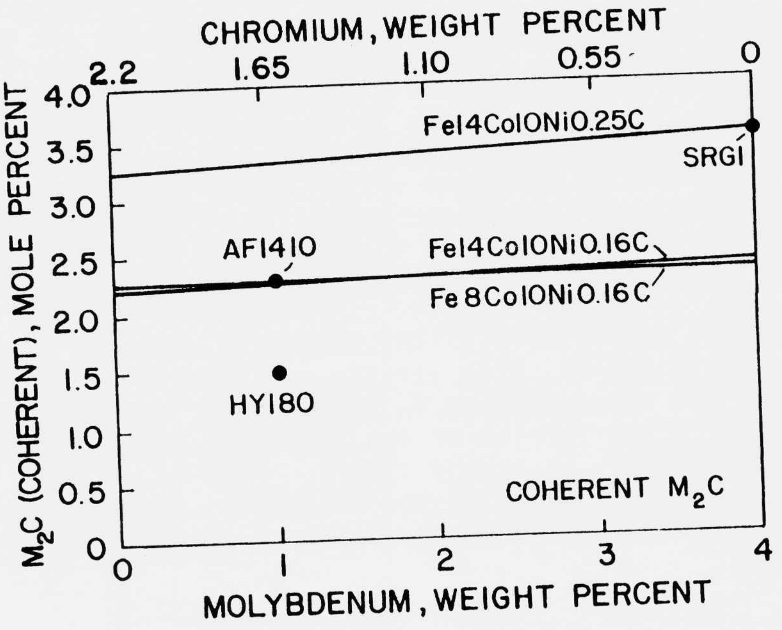

Fig. 6 Effect of additions of Co, C, Cr and Mo on the mole fraction of coherent M_2C phase

Another important characteristic of the M_2C phase which directly affect its contribution to the strength, is its coarsening resistance. Coarsening of multicomponent carbides has been recently modelled by Grujicic et al. (12). Figure 7 shows the effect of substituting chromium for molybdunum in a 14Co 10Ni0.25C matrix (13) on the rate constant for particle coarsening. In general there is an optimum Cr/Mo ratio which gives rise to the highest coarsening resistance of the M_2C phase.

7. PRECIPITATION OF COMPETING PHASES

As mentioned earlier, the M_2C phase tends to overage after prolonged tempering while it is being gradually superceded by other more stable phases, $M_{23}C_6$, M_6C and austenite. The stable carbide phases are typically coarse and, as discussed in connection with Figure 1, give rise to a simultaneous degradation of both strength and toughness. Austenite precipitation, on the other hand, can be beneficial provided the austenite has sufficient stability. It is therefore important to test the thermodynamic stability of a two-phase mixture ferrite and coherent M_2C, with respect to the precipitation of other phases. It is believed that the region associated with the optimum combination of strength and toughness corresponds to a two-phase ferrite/M_2C microstructure mixture, when carbide dissolution has just been completed and the formation of stable carbides has not yet started. Thermodynamic stability of ferrite/M_2C mixture is shown in Figure 8, where the driving force for nucleation of stable phases from this mixture is shown for a series of Fe14Co10Ni. 16CMoCr alloys. It is worth noting that there is a range of Cr and Mo additions within which austenite is most likely to form during prolonged tempering. The precipitated austenite can be beneficial to the materials ductility and toughness, provided its stability is sufficiently high.

A typical composition of the austenite shown in Figure 8 is 4 wt% Co, 39 wt% Ni, with varying small additions of C, Cr and Mo. The corresponding T_0 temperature, the temperature at which austenite and ferrite of the same composition have equal free energies, is around -100°C. This is an indication of a good stability of the austenite, necessary for an improved ductility and toughness, by transformation-induced plasticity.

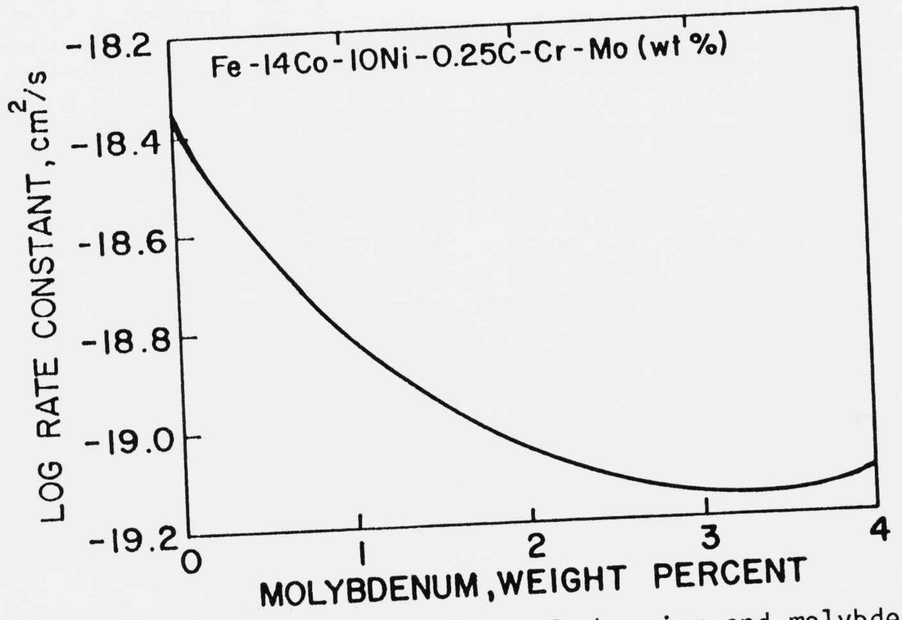

Fig. 7 Effect of combined additions of chromium and molybdenum on the rate of coarsening of the M_2C phase in a Fe-14Co-10Ni-0.25C-(Mo-Cr) alloy

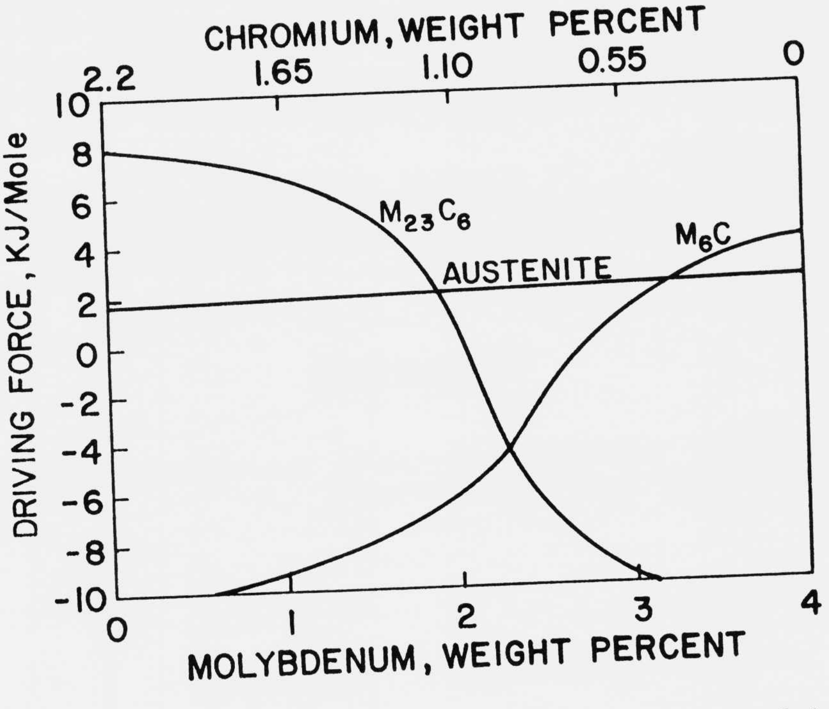

Fig. 8 Effect of combined additions of chromium and molybdenum on the driving force for nucleation of M_6C, $M_{23}C_6$ and austenite from a two-phase ferrite/coherent M_2C mixture in a Fe-14Co-10Ni-0.16C-(Mo-Cr) alloy

8. CONCLUSION

On the basis of the thermodynamic analysis presented above, we can now proceed with selecting the composition of a high Co-Ni secondary hardening steel to give the maximum combination of strength and superior toughness.

The results shown in Figure 5 suggest that lower cobalt additions might be preferred with respect to an enhancement of the driving force for nucleation of the strengthening M_2C phase. However, on the other hand higher cobalt additions might be necessarty to ensure an effective retardation of dislocation recovery, a prerequisite for a fine scale heterogeneous nucleation of the M_2C phase. Since the effect of cobalt on the driving force for nucleation of M_2C (Fig. 5), appears to be minor, we adopt the high Co addition (14wt.%) for our steel.

To ensure maximum strength, carbon content should be set to its maximum value, 0.25 wt%.

Additions of 3 wt% Mo and 0.55 wt% Cr. appear to be optimum with respect to achieving maximum driving force for nucleation (Fig. 5) and optimum mole fraction (Fig. 6) of the strengthening M_2C phase, accompanied by a large tendency for precipitation of a toughening austenite phase.

To summarize, the proposed composition of a new high-strength secondary hardening steel, optimized for maximum strength and good toughness is Fe-14Co-10Ni-3Mo-0.55Cr-0.25C (wt%).

ACKNOWLEDGMENT

This work has been supported by the National Science Foundation under Grant #DMR-84-18718.

REFERENCES

(1) G.R. Speich, D.S. Dabkowski and L.F. Porter, Metall. Trans. (1973) 303.

(2) General Dynamics, U.S. Patent No. 4,076,525 (1978).

(3) B. Sundman, B. Jansson an J.O. Andersson, Calphad, 9 (1985) 153.

(4) A.S. Argon, in Encyclopedia of Materials Science and Engineering, ed. M.B. Bever, Pergamon Press, Ltd, 1986 p. 3543-3547.

(5) J.S. Langer and A.J. Schwartz, Phys. Rev. A21 (1980) 948.

(6) R. Kampmann and R. Wagner, in Decomposition of Alloys, ed. P. Haasen et al., Pergamon Press, New York, New York (1984), p. 91.

(7) R.A. Clark and G. Thomas, Metall. Trans. A, 6A (1975) 969.

(8) C.D. Little and P.M. Machmeier, General Dynamics Report, No. AFML-TR-75-148, (1975).

(9) G. Haidemenopoulos, Doctoral Thesis in Progress, MIT, 1987.

(10) M. Grujicic, Research in Progress, MIT 1987.

(11) M. Grujicic and G.B. Olson, to be published in Calphad, 1988.

(12) M. Grujicic, H.M. Lee, S.M. Allen, Proc. Int'l Conf. User Applic. Alloy Phase Diagrams, ed. L. Kaufman, ASM Int'l., (1987), pp. 195-201.

(13) H.M. Lee, Doctoral Thesis in Progress, MIT, 1987.

CHARACTERIZATION OF 4% MOLYBDENUM SRG EXPERIMENTAL STEEL

MICHAEL SCHMIDT*, RAYMOND HEMPHILL

Tool and Alloy R&D, Carpenter Technology Corp.,
Reading, PA, 19612-4662

INTRODUCTION

Presently, a ferrous-base high strength/high toughness alloy does not exist which exhibits 55-60 HRC and 60-120 ksi$\sqrt{\text{in.}}$ Such an alloy, if it existed, could be used extensively in defense-related programs as support and structural components for aircraft and aerospace vehicles and possibly for armor components. Recognizing the need for such a material, the National Science Foundation (NSF) has awarded a grant to the Massachusetts Institute of Technology (MIT) to develop a martensitic steel with the previously described strength and toughness levels.

The personnel involved in this "Innovations in High Strength Steel Technology" program believe that the program objectives can be achieved by modifying the composition of AF 1410 (nominal composition: 0.16% C, 14% Co, 10% Ni, 2% Cr, 1% Mo, balance Fe). This alloy is a high strength (48-50 HRC), high fracture-resistant (150+ ksi$\sqrt{\text{in.}}$) steel developed by Little and Machmeier(1,2) for use in highly stressed airframe structural components. Presently, this alloy is being used in the arrestor hook landing mechanism for carrier-based F-18 aircraft.

Work performed at the Massachusetts Institute of Technology studied potential alloy modifications of AF 1410 to provide the optimum driving force for carbide precipitation during aging. This work was done using the Swedish computer software known as Thermo Calc. One of the findings of this work was that a 4% molybdenum, Cr-free modification of AF 1410 would have the highest thermodynamic driving force for M_2C carbide precipitation during aging; therefore, this modification of AF 1410 was of interest for studying carbide precipitation behavior. This work also indicated that the 14% cobalt 10% nickel alloy content of AF 1410 would be satisfactory from a austenite-ferrite viewpoint and should not give excessive reverted austenite during aging. A 0.25% C, 4% Mo, 14% Co, 10% Ni composition was selected as the first alloy to be evaluated in this program.

MATERIALS AND METHODS

Two heats of the 4% Mo steel were melted in a 17 lb. vacuum induction furnace, cast under argon into a 2.75 inch square tapered ingot and allowed to air cool. The compositions listed in Table 1 show that heat V00009 had a carbon content of 0.29% which was outside the C melt limits of 0.23/0.27. Therefore, a second heat of steel was melted with a carbon level of 0.23%. All residual levels were kept very low by melting a base charge of electrolytic iron and by using high purity alloy additions. Since, both heats had essentially the same composition except for the C content, a decision was made to process both V00009 and V00069 in order to study the effect that C content has on the microstructure and aging characteristics of a 4% Mo, Cr-free version of AF 1410.

TABLE 1

COMPOSITION OF THE TWO EVALUATED HEATS

Element	Heat V00009*	Heat V00069*
C	.29	.23
Mn	<.01	<.01
Si	<.01	<.01
P	<.005	<.005
S	.002	.003
Cr	.01	.06
Ni	10.20	10.24
Mo	3.88	3.96
Co	14.06	14.17

* 17 lb. VIM heats cast into 2.75" sq. tapered ingots.

Both heats were then thermomechanically processed identically. The ingots were homogenized at 2200°F for 6 hours and forged to 1.25 inch square bars from 2200°F. Each bar was cut in half and reheated for approximately 1 hour in a furnace held at 1800°F. The bars were forged to 0.75 inch square from 1800°F and the forgings were allowed to air cool.

The microstructure of each heat was evaluated in the as-forged condition. A longitudinal surface from each forging was prepared for metallographic examination using standard techniques. The prepared samples were etched in a solution of 10% aqueous sodium meta-bisulfite (10% SMB) using a full immersion technique. Microstructures at the centerline and mid-radius locations were examined and representative photomicrographs were taken. Since significant solidification segregation was apparent at the centerline of heat V00009, a Cameca CMX electron microprobe was used to quantify the compositional differences at the bar center as compared to the balance of the cross section. An accelerating voltage of 20 kV, a filament current of 0.04 milliamps, and an absorbed current of 10 nanoamps were used during this analysis.

Based on the as-forged microstructure, a solution treating study was conducted prior to overaging of the forged bars. The general concept of this study was to examine the steel based on the following criteria:

i. dissolve the grain boundary pinning alloy carbides in order to promote the formation of equiaxed grains via recrystallization,

ii. maintain a fine grain structure.

Samples from heat V00009 were heated to 1600, 1800, 2000, and 2200°F for 1 hour in a neutral salt bath and oil quenched. The hardness and microstructure of the solution treated samples were evaluated. A longitudinal surface from each sample was prepared for metallographic examination and etched with 10% SMB. Representative photomicrographs were taken of the observed structures. Additionally, the grain size of samples was rated using the ASTM comparative method at a magnification of 100X.

Based on the initial solution treating study, it appeared that the optimum solution treating temperature from the viewpoint of criteria listed in the previous paragraph was between 1800 and 2000°F. Therefore, a second more focused study was conducted to pinpoint this optimum temperature. Triplicate samples from heat V00009 were solution treated at 1800, 1850, 1900, 1950 and 2000°F for 1 hour in a neutral salt bath and oil quenched. One sample from each solution treating practice remained in the as-quenched condition, while the remaining two samples were aged at either 900°F for 5 hours or 1250°F for 8 hours. The aging treatments were performed in order to determine what effect any variation in the solution treating practice might have on either the peak aging or overaging response. Rockwell C hardness testing was conducted on all samples, and the microstructures of the overaged samples were evaluated. A longitudinal surface was prepared for metallographic examination, the samples were etched with 10% SMB, representative photomicrographs were taken, and the ASTM grain size was rated using the comparative method at a magnification of 100X.

Based on the results from the solution treating studies conducted on as-forged material representing heat V00009, both sets of forged bars were solution treated at 1825°F prior to overaging. The complete thermal cycle entailed solution treating at 1825°F for 1 hour followed by an oil quench and overaging at 1250°F for 8 hours followed by an air cool.

An aging study was performed on both heats. The goals of the aging study were to examine the effects that solution treating temperature, C content, and aging time had on the aging response of a 4% Mo, Cr-free modification of AF 1410. Representative samples from both heats were solution treated at 1800 and 2100°F in neutral salt for 1 hour and oil quenched. All samples were refrigerated in a solution of dry ice and methanol for 1 hour prior to aging at 400, 800, 850, 900, 950, 1000, 1100, 1200 or 1300°F for times of 1, 5 or 8 hours. Rockwell C hardness testing was conducted on all samples.

Charpy V-notch impact testing was conducted on both heats. Longitudinal specimen blanks were removed from each bar and rough machined to 0.020 inch oversize prior to heat treating. The rough machined blanks were solution treated in neutral salt at 1800, 1950 or 2100°F for 1 hour and oil quenched prior to aging at 950°F for 5 hours. Due to a lack of material, only the 1800°F condition was tested on heat V00009. All samples were machined to finish size, notched and duplicate room temperature testing was conducted. Following testing the hardness of select specimens was evaluated and select fracture faces were examined with an Amray 1000 SEM operating at 20 keV. Representative backscatter electron (BSE) and secondary electron (SE) images were recorded.

Based on the impact test results from material in the 950°F, 5-hour-aged condition, additional samples from heat V00069 were fabricated and tested in the as-solution treated condition. Select hardness testing and SEM fractography were also conducted on these samples. Representative backscatter electron and secondary electron images were recorded.

The effects of solution treating temperature on impact toughness were examined since work by Schmidt and Gore(3) and Garrison and Moody(4) has shown that the use of high solution treating temperatures can have a favorable effect on the toughness of AF 1410 steel by reducing the number of sub-micron size microvoid-nucleating particles. Thus, the use of the 1800°F treatment would provide the optimum grain size for toughness; whereas, the 2100°F treatment is designed to provide a coarser grain structure and complete carbide solutioning.

RESULTS AND DISCUSSION

Representative photomicrographs of the as-forged microstructures from both heats are contained in Figure 1. The structures at the mid-radius location (Figures 1a and 1c) show that both heats contained elongated, non-recrystallized grains. The presence of grain boundary carbide is clearly visible in both of these structures; however, heat V00009 appears to contain a larger volume fraction of this phase. It is believed that these carbides precipitated at the grain boundaries during the final hot working practice from 1800°F. By precipitating at the grain boundaries, these carbides - which are believed to be M_6C based on the alloy contents of the two heats - effectively prevented proper recrystallization of the grain structure during final hot working.

Compared to the mid-radius, the centerline of both heats exhibited a finer grain structure which again showed signs of being incompletely recrystallized (Figures 1b and 1d). The low C heat (V00069) showed signs of a slight increase in the amount of carbide out of solution at the centerline versus the mid-radius location; whereas, the high C heat (V00009) showed evidence of gross alloy segregation at the centerline location. Analysis of representative mid-radius and centerline locations from V00009 using an electron microprobe revealed an enrichment in Mo and a slight depletion in Fe (Table 2). The severity of Mo segregation in this material was surprising based on the small size of the ingot. This problem would only be accentuated if an attempt were made to scale up to a larger

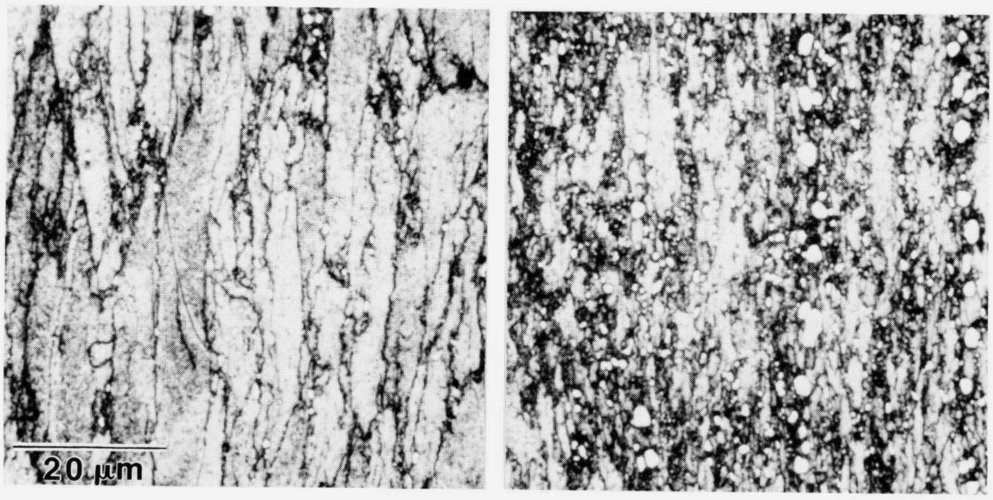

a. V00009 (mid-radius) b. V00009 (centerline)

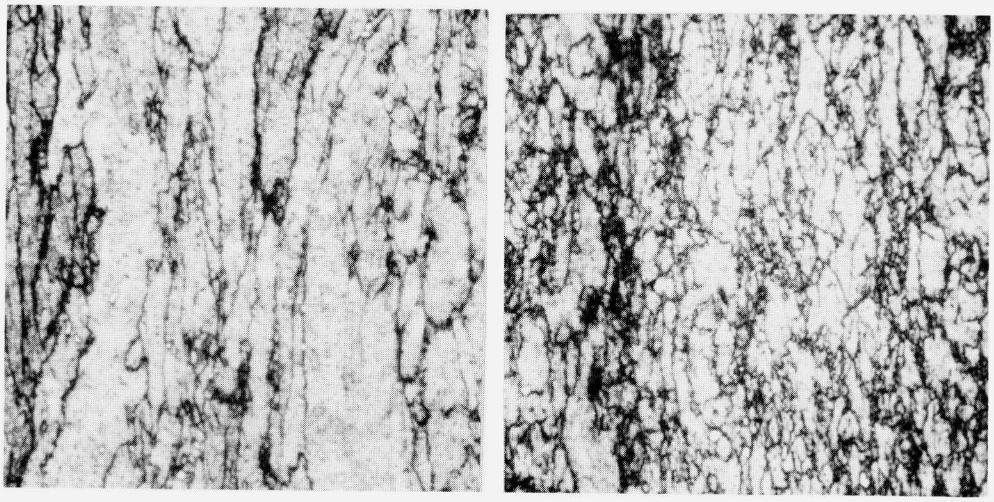

c. V00069 (mid-radius) d. V00069 (centerline)

FIGURE 1. Optical photomicrographs of the as-forged microstructure at the mid-radius and centerline of 0.75 inch square bars from heats V00009 (0.29% C) and V00069 (0.23% C). Samples were etched with 10% SMB.

commercial heat lot quantity. It is envisioned that powder metallurgical processing would be required to obtain a uniform composition.

The results of the hardness testing conducted on as-forged samples from V00009 solution treated at 1600-2000°F

TABLE 2

RESULTS OF THE ELECTRON MICROPROBE ANALYSIS (95% CONFIDENCE LIMITS) CONDUCTED ON V00009

Element	Mid-Radius	Centerline
Fe	71.27-72.81	68.03-70.61
Mo	3.46- 3.90	5.70- 7.40
Ni	9.10- 9.62	8.86- 9.28
Co	12.76-13.56	12.50-12.96

in 200°F increments are contained in Table 3, while the microstructures are documented in Figure 2. Following solution treating at 1600°F, the hardness is 48 HRC; however, as shown in Figure 2a most of the grain boundary pinning carbide has not been taken into solution, and as such, the grain structure is still predominantly non-recrystallized. As the solution treating temperature is raised to 1800°F, the as-quenched hardness increases to 53 HRC and the structure is completely recrystallized (Figure 2b), although a significant volume fraction of carbide is still out of solution. Solution treating at 2000°F results in nearly complete carbide dissolution (Figure 2c) and an as-quenched hardness of 55 HRC; however, significant grain coarsening has occurred. A further increase in the solution treating temperature only serves to further coarsen the structure (Figure 2d).

TABLE 3

HARDNESS TEST RESULTS FROM THE INITIAL SOLUTION TREATING STUDY ON V00009

Treatment*	Hardness (HRC)
1600°F (salt) - 1h, OQ	48.0
1800°F (salt) - 1h, OQ	53.0
2000°F (salt) - 1h, OQ	55.0
2200°F (salt) - 1h, OQ	55.0

*Conducted on as-forged material

Based on the results from the initial solution treating study, the optimum solution treating temperature

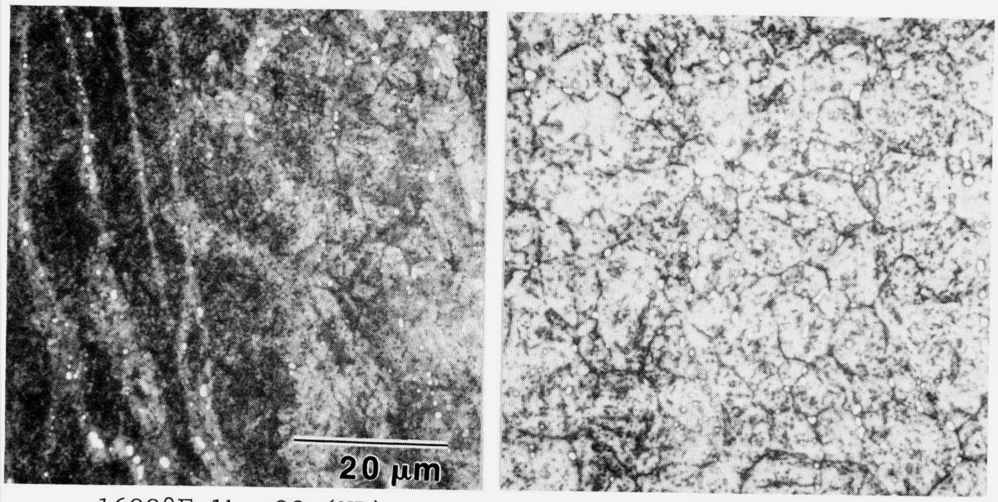

a. 1600°F-1h, OQ (NR) b. 1800°F-1h, OQ (8/9)

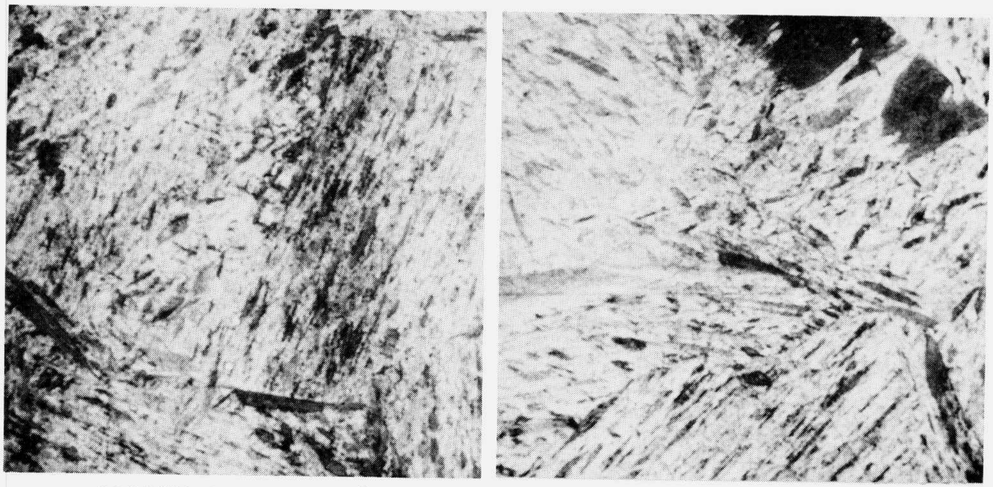

c. 2000°F-1h, OQ (4/5) d. 2200°F-1h, OQ (0/1)

FIGURE 2. Optical photomicrographs (same magnification) showing the effect of solution treating temperature on the as-quenched microstructure of V00009 (0.29% C). Samples were etched with 10% SMB. ASTM grain size rating in parentheses (NR = not rateable).

from the viewpoint of dissolving some of the alloy carbide but maintaining a relatively fine grain size is between 1800 and 2000°F. Therefore, a second, more focused solution treating study was performed on as-forged material representing heat V00009. The Rockwell C hardness data from material solution treated at 1800-2000°F in 50°F increments and then tested in the as-quenched, 900°F-5 hour aged and 1250°F-8 hour aged conditions are contained in Table 4. These data show that the as-quenched hardness gradually increases from 53 to 55 HRC as the solution treating temperature is raised from 1800 to 2000°F. The data corresponding to material in the 900°F-5 hour aged condition show that the hardness increases from 58.5 to 60 HRC when the solution treating temperature is increased from 1800 to 1950/2000°F. The fact that the as-quenched and 900°F-5 hour aged hardness levels are increased by 2 and 1.5 HRC points, respectively, indicates that some additional alloy solutioning is occurring as the solution treating temperature is raised from 1800 to 2000°F.

TABLE 4

ROCKWELL C HARDNESS TEST RESULTS FROM THE FOCUSED SOLUTION TREATING STUDY CONDUCTED ON V00009

	Hardness (HRC)		
Solution Practice	As-Quenched	900°F-5h, AC	1250°F-8h, AC
1800°F-1h, OQ	53.0	58.5	41.5
1850°F-1h, OQ	52.5	59.0	41.5
1900°F-1h, OQ	53.5	59.5	42.0
1950°F-1h, OQ	54.5	60.0	41.5
2000°F-1h, OQ	55.0	60.0	41.5

With regard to the effect of solution treating temperature on the hardness of overaged material, the data in Table 4 show that the 1250°F-8 hour aged hardness of V00009 is insensitive to variations in solution treating temperature within the 1800 to 2000°F range. However, the photomicrographs in Figure 3 show the coarsening of the structure that occurs as the solution treating temperature is increased from 1800 to 2000°F. More importantly, this series of photomicrographs shows a tendency for carbide formation and growth at the grain and sub-grain boundaries of overaged material as the solution treating temperature is increased from 1800 to 2000°F. For example, traces of carbide are visible at some of the boundaries in material solution treated at 1900°F (Figure 3b - see arrows), while evidence of extensive carbide growth at a packet boundary is shown in Figure 3c (2000°F solution treatment). The presence of these carbides at grain and sub-grain boundaries is undesirable from a toughness viewpoint; however,

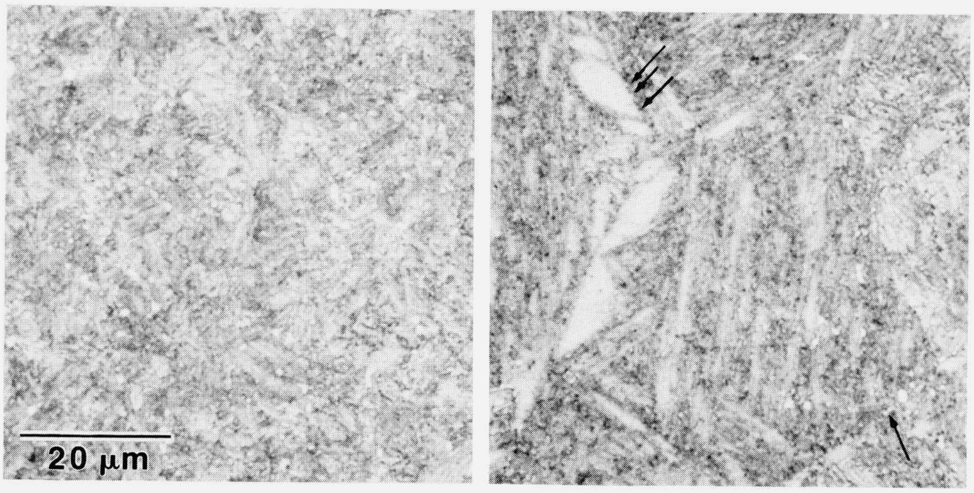

a. 1800°F-1h, OQ (8/9) b. 1900°F-1h, OQ (6/7)

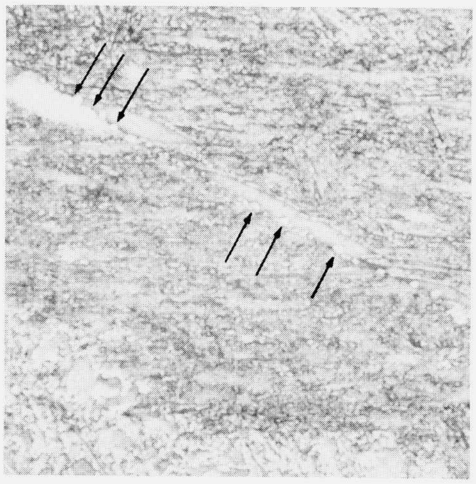

c. 2000°F-1h, OQ (4/5)

FIGURE 3. Optical photomicrographs (same magnification) showing the effect of solution treating temperature on the 1250°F-8 hour overaged microstructure of V00009. Samples were etched with 10% SMB. ASTM grain size rating in parentheses.

the key question is how pronounced is this condition when aging in the 850-950°F temperature range.

Based on the results from the focused solution treating study, 1825°F was chosen as the solution treating temperature to be used on the as-forged bars prior to overaging. This temperature was chosen since it appeared to be the optimum temperature from the viewpoint of being high enough to promote significant solutioning of excess carbide, and thus allow recrystallization of the grain structure, yet low enough in order to maintain a relatively fine grain structure.

The results of the Rockwell C hardness testing conducted during the aging study are contained in Tables 5 and 6 for material solution treated at temperatures of 1800 and 2100°F, respectively. These data in turn were used to construct plots that detailed the effects of solution treating temperature (Figure 4), carbon content (Figure 5) and aging time (Figure 6) on the aging response of the 4% Mo, Cr-free modification of AF 1410.

TABLE 5

AGING RESPONSE (HRC) FOR MATERIAL SOLUTION TREATED AT 1800°F*

	V00009 (.29% C)			V00069 (.23% C)		
Aging Temp.	Aging Time (h)			Aging Time (h)		
(°F)	1	5	8	1	5	8
As-Quenched	52.0	52.0	52.0	48.0	48.0	48.0
400	50.5	50.5	51.5	48.5	48.5	48.5
800	53.5	55.0	54.5	51.5	52.5	53.0
850	55.0	56.5	57.0	53.0	54.5	55.5
900	56.5	58.5	58.5	55.0	56.0	56.0
950	57.5	57.0	56.0	55.5	53.5	52.5
1000	56.5	54.0	53.0	53.0	48.5	47.5
1100	51.5	46.5	45.0	45.5	40.0	39.0
1200	43.5	42.0	41.0	39.5	37.0	36.5
1300	42.5	40.0	39.5	38.0	36.5	35.5

*Heat treatment: 1800°F (salt)-1h, OQ; -100°F (dry ice and methanol)-1h, AW; aged as indicated.

The effect of an 1800 versus a 2100°F solution treating practice on the aging response of material representing heat V00069 (0.23% C) aged for 5 hours is shown in Figure 4. The use of these two solution treating practices represents two different heat treating philosophies. An 1800°F solution treatment represents the conventional tool steel heat treating philosophy of solution treating at the maximum temperature at which the steel will remain fine grained; whereas, a 2100°F treatment represents the philosophy that full solutioning of all alloy carbides is the best starting point for aging a material. The plots contained in Figure 4 show that increasing the solutioning treating temperature of V00069 from 1800 to 2100°F does not alter the temperature at which peak aged hardness occurs (i.e. 900°F); however, the use of a 2100°F solution treatment does result in an upward vertical shift in the aging curve of approximately 1.5 HRC points for aging temperatures ≤1100°F. This effect can be attributed to the increased alloy (i.e. C and Mo) in solid solution that is available for the precipitation hardening reaction. For aging temperatures >1100°F this trend is not true. The effect of higher solution treating temperature (i.e. 2100 vs. 1800°F) promoting a slight increase in age hardening response is also apparent in material representing heat V00009 (see Tables 5 and 6).

TABLE 6

AGING RESPONSE (HRC) FOR MATERIAL SOLUTION TREATED AT 2100°F*

	V00009 (.29% C)			V00069 (.23% C)		
Aging Temp.	Aging Time (h)			Aging Time (h)		
(°F)	1	5	8	1	5	8
As-Quenched	54.0	54.0	54.0	51.0	51.0	51.0
400	52.0	51.0	51.0	49.0	49.0	49.0
800	55.0	55.0	56.5	51.5	54.0	54.0
850	56.5	57.5	59.0	53.5	56.0	56.5
900	59.0	59.5	58.5	57.5	57.5	57.0
950	60.0	57.5	56.5	57.0	55.5	54.0
1000	58.0	55.0	53.5	54.5	50.5	47.5
1100	51.5	47.0	46.0	46.5	41.0	39.5
1200	44.0	41.5	40.5	40.5	37.0	36.0
1300	42.0	40.0	39.5	37.5	34.5	34.5

*Heat treatment: 2100°F (salt)-1h, OQ; -100°F (dry ice and methanol)-1h, AW; aged as indicated.

The effect of 0.29 versus 0.23% C on the aging response of 4% Mo, Cr-free AF 1410 solution treated at 1800°F for 1 hour and oil quenched followed by aging at

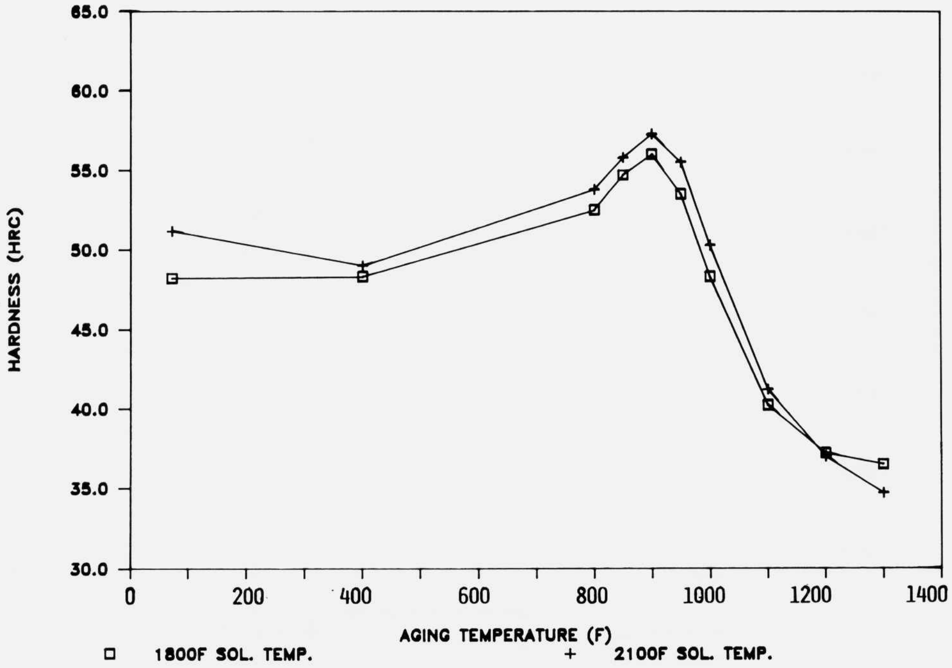

FIGURE 4. Plots of aging response for heat V00069 (0.23% C) showing the effect of solution treating temperature. Heat treatment: 1800 or 2100°F (salt)-1h, OQ; -100°F (dry ice and methanol)-1h, AW; aged at temperature (air)-5h, AC.

temperature for 5 hours is shown in Figure 5. These data show that increased C results in an upward vertical shift in the aging curve. This shift is more pronounced for aging temperatures in excess of 1000°F. For example, the average shift in aged hardness for the 0.29 versus the 0.23% C material was 3.0 HRC points for aging temperatures <1000°F but for aging temperatures ≥ 1000°F an average shift of 5.5 HRC points was observed. No apparent shift in the temperature at which peak aged hardness occurs was observed.

The data contained in Tables 5 and 6 show that C had similar effects with regard to shifting the magnitude of the aging response of material solution treated at 2100°F or for material aged at temperature for either 1 or 8 hours. It should be noted though that the magnitude of increase in aging response varied slightly for these other conditions.

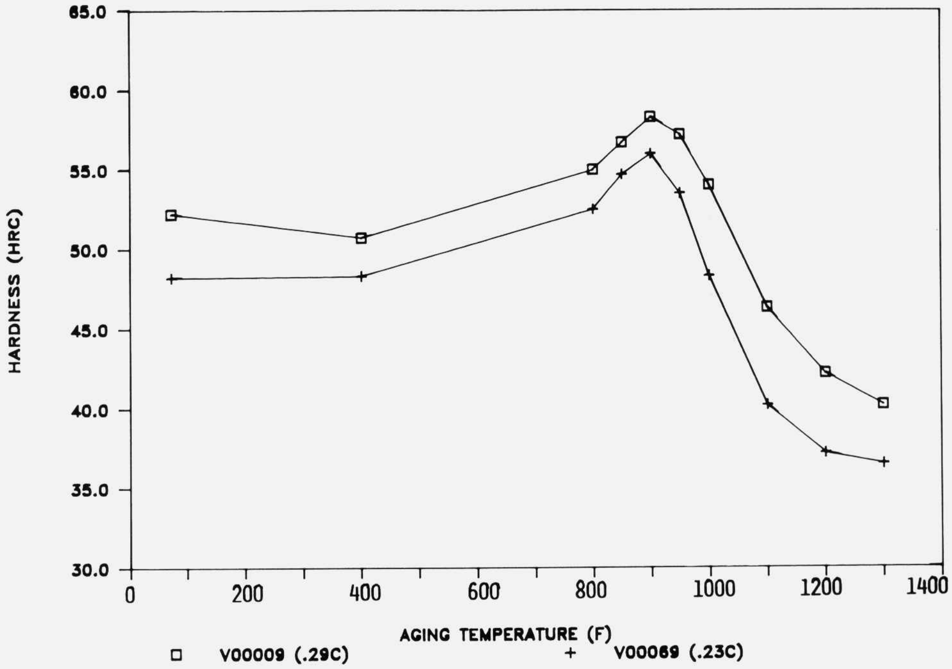

FIGURE 5. Plots of aging response for heats V00009 (.29% C) and V00069 (.23% C) showing the effect of C content. Heat treatment: 1800°F (salt)-1h, OQ; -100°F (dry ice and methanol)-1h, AW; aged at temperature (air)-5h, AC.

The effect of aging time on the aging response of heat V00069 (.23% C) solution treated at 2100°F is shown by the plots contained in Figure 6. In general, these data show that aging for either 5 or 8 hours provides a similar aging response, particularly for aging temperatures ≤900°F, while a 1 hour age shifts the aging curve to the right by approximately 50°F. For example, the combined data in Tables 5 and 6 show that peak aged hardness occurred at 950°F when using a 1 hour age; whereas, aging for 5 or 8 hours promoted peak aged hardness at 900°F. In one case (heat V00009 solution treated at 2100°F) an 8 hour age resulted in peak aged hardness at 850°F. Overall the difference in aged hardness when aging for either 5 or 8 hours is ≤2.0 HRC regardless of the temperature used; however, aging times of 1 hour can result in aged hardness values that are up to 5.0 HRC points greater when aging at temperatures in excess of 950°F.

The major finding of the aging study was that both

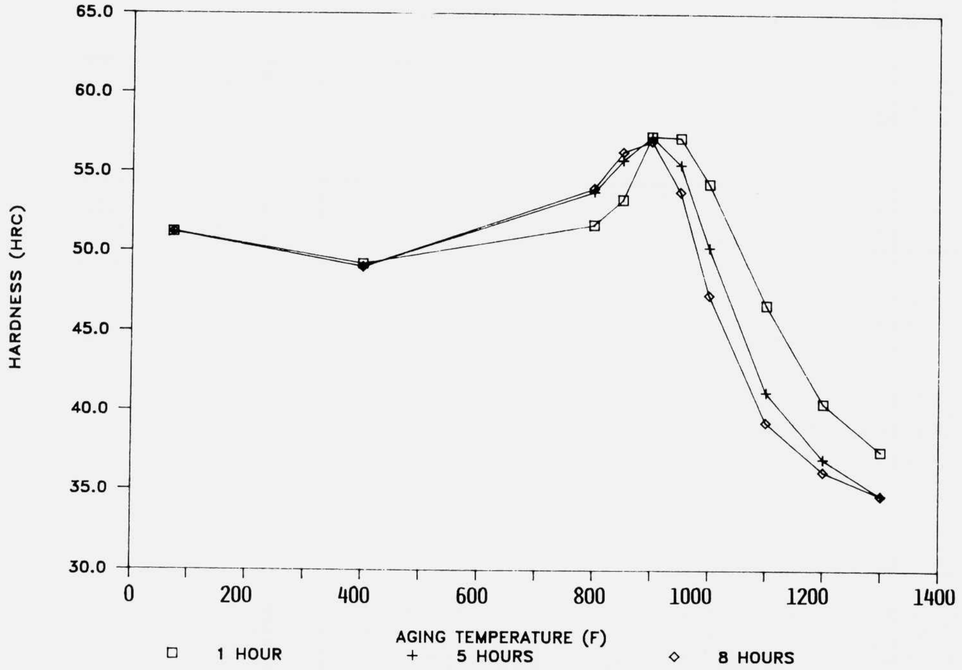

FIGURE 6. Plots of aging response for heat V00069 (0.23% C) showing the effect of aging time.
Heat treatment: 2100°F (salt)-1h, OQ; -100°F (dry ice and methanol)-1h, AW; aged at temperature (air)-1, 5 or 8h, AC.

alloys are capable of achieving the program objective of 55 HRC minimum. The data contained in Tables 5 and 6 show that this objective can be achieved by using either an 1800°F or a 2100°F solution treating practice and by using a variety of aging treatments.

The results of the Charpy V-notch impact testing that was conducted on material solution treated at 1800, 1950 or 2100°F for 1 hour and oil quenched followed by aging at 950°F for 5 hours are contained in Table 7. Examination of the data corresponding to V00069 show that the impact toughness decreases from 3 ft.-lbs. at 54.0 HRC to 1.5 ft.-lbs. at 55.5 HRC when the solution treating temperature is increased from 1800 to 2100°F. These results are discouraging, since it was anticipated that toughness levels in excess of 10 ft.-lbs. might be obtained with this alloy. The data in Table 7 also show that the 0.29% C heat exhibited reduced toughness (i.e. 1.5-2.0 ft.-lbs. at 57.5 HRC) when compared to the 0.23% C heat.

TABLE 7

LONGITUDINAL, ROOM TEMPERATURE CHARPY V-NOTCH IMPACT TEST RESULTS ON AGED MATERIAL

Solution Practice[b]	V00009 (0.29% C)		V00069 (0.23% C)	
	CVN (ft.-lbs.)	HRC	CVN (ft.-lbs.)	HRC
1800°F-1h, OQ	2, 1.5	57.5	3, 3	54.0
1950°F-1h, OQ	–[c]	–	2, 2	54.5
2100°F-1h, OQ	–[c]	–	1.5, 1.5	55.5

[a] Aging treatment: 950°F (air)-5h, AC

[b] Samples treated in neutral salt

[c] Insufficient material available for testing

TABLE 8

LONGITUDINAL, ROOM TEMPERATURE CHARPY V-NOTCH IMPACT TEST RESULTS ON SOLUTION-TREATED MATERIAL FROM V00069

Solution Practice	CVN (ft.-lbs.)	HRC
1800°F (salt)-1h, OQ	3, 3	51.0
1950°F (salt)-1h, OQ	12, 12	51.5
2100°F (salt)-1h, OQ	17, 19	52.5

The fracture mode associated with the material solution treated at 1800°F consisted of a combination of intergranular decohesion due to undissolved grain boundary carbides and some areas of transgranular microvoid coalescence (Figure 7). Carbides approximately 0.5-1 μm in diameter were observed at the base of numerous microvoids (Figure 7b). Energy dispersive x-ray analysis of these carbides indicated that they were enriched in Mo. Based on the available data it is believed that these carbides are M_6C.

Figure 8a shows that the fracture morphology associated with material solution treated at 2100°F prior to aging at 950°F is nearly 100% brittle intergranular fracture with pronounced secondary cracking (Figure 8b). Visual evidence of intergranular phases could not be detected via SEM examination. Figures 8a and 8b show evidence that some of the cleavage facets exhibited signs of increased ductility compared to other cleavage facets.

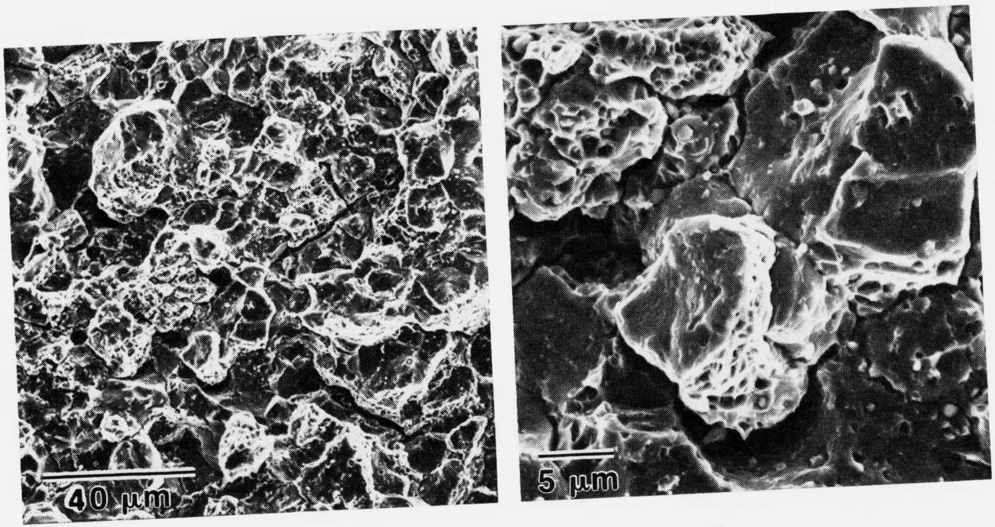

a. SE Image

b. SE Image

FIGURE 7. Representative SEM fractographs of a Charpy V-notch specimen from heat V00069 (0.23% C) solution treated at 1800°F and tested in the aged condition.
Heat treatment: 1800°F (salt)-1h, OQ; 950°F (air)-5h, AC
CVN: 3.0 ft.-lbs. HRC: 54.0

Higher magnification imaging of these areas revealed that they failed by a combination of quasi-cleavage and microvoid coalescence (Figure 8c).

Based on the data contained in Table 7 and Figures 7 and 8, a decision was made to test material in the as-quenched condition in order to determine if the aging treatment is responsible for the poor impact toughness observed in the evaluated material. The results of this testing are contained in Table 8. These data show that for a solution treating temperature of 1800°F similar toughness is obtained at a lower hardness level (51.0 versus 54.0 HRC) in the as-quenched condition. Examination of a representative fracture surface via SEM revealed that the fracture mechanism (i.e., intergranular decohesion due to undissolved grain boundary carbides and some transgranular microvoid coalescence) associated with the as-quenched material (Figure 9) is identical to that of the 950°F-5 hour aged material (Figure 7). Thus, the observed similarities between the toughness and fracture mechanism of as-quenched and quenched-plus-aged material solution treated at 1800°F suggest that the remnant undissolved

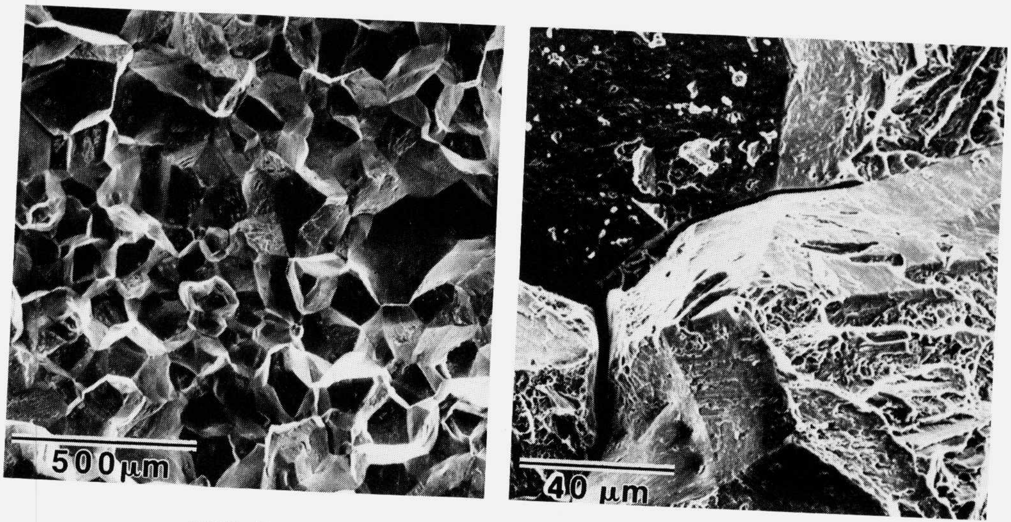

a. BSE Image

b. SE Image

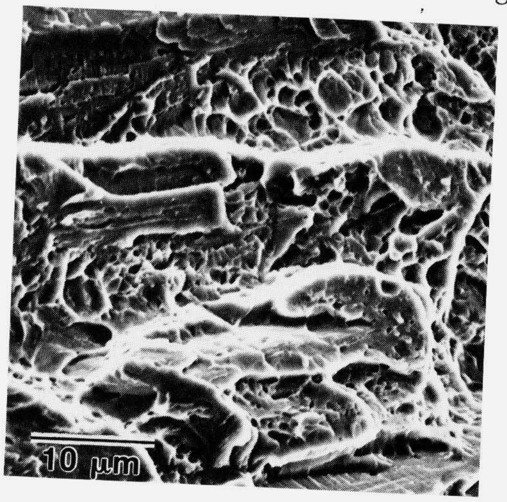

c. SE Image

FIGURE 8. Representative SEM fractographs of a Charpy V-notch specimen from heat V00069 (0.23% C), solution treated at 2100°F and tested in the aged condition.
Heat treatment: 2100°F (salt)-1h, OQ; 950°F (air)-5h, AC
CVN: 1.5 ft.-lbs. HRC: 55.5

carbides present in the microstructure are controlling the fracture process.

The data in Table 8 show that the impact toughness of as-quenched material increases as the solution treating

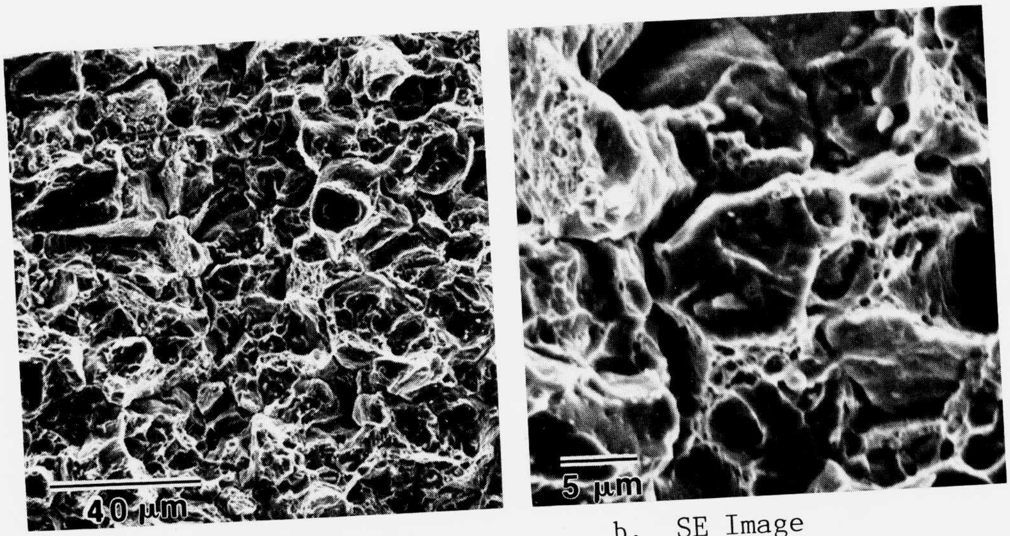

a. SE Image

b. SE Image

FIGURE 9. Representative SEM fractographs of a Charpy V-notch specimen from heat V00069 (0.23% C) solution treated at 1800°F and tested in the as-quenched condition.
Heat treatment: 1800°F (salt)-1h, OQ
CVN: 3.0 ft.-lbs. HRC: 51.0

temperature is increased above 1800°F. For example, the average impact toughness is 18.0 ft.-lbs. at 52.5 HRC for material solution treated at 2100°F versus 3.0 ft.-lbs. at 51.0 HRC for material solution treated at 1800°F. Compared to material aged at 950°F for 5 hours following a 2100°F solution treatment, the toughness of the as-quenched material is improved by over an order of magnitude. Analysis of the fracture surface of as-quenched material solution treated at 2100°F revealed a coarse, but ductile appearing fracture (Figure 10a). Higher magnification imaging revealed that the main fracture mechanism was classical microvoid coalescence (Figure 10b). The flatter looking portions of the fracture shown in Figure 10a also appeared to fail by microvoid coalescence; however, the appearance of these areas at higher magnification imaging was atypical for microvoid coalescence.

The data in Table 8 and Figures 9 and 10 show that dissolution of Mo-rich carbides formed during overaging at 1250°F results in improved impact toughness in the as-quenched condition. However, in the 950°F aged condition the use of high solution treating temperatures results in embrittlement of the grain boundaries when the material is

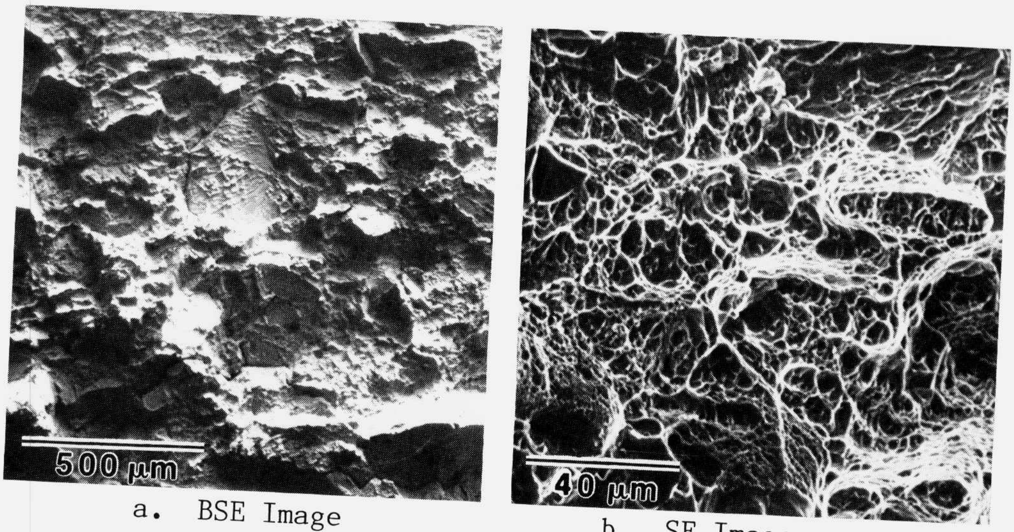

a. BSE Image
b. SE Image

c. SE Image

FIGURE 10. Representative SEM fractographs of a Charpy V-notch specimen from heat V00069 (0.23% C) solution treated at 2100°F and tested in the as-quenched condition.
Heat treatment: 2100°F (salt)-1h, OQ
CVN: 19.0 ft.-lbs. HRC: 52.5

aged. It is possible that this grain boundary embrittlement is the result of the formation of a carbide film during aging. While no direct evidence exists to support this statement, it should be recalled that numerous grain boundary carbides in the 0.5-1.5 µm size range were observed in overaged material solution treated at temperatures $\geq$1900°F (Figures 3b and 3c). It is recommended that Auger spectroscopy and TEM/STEM analysis be conducted to determine the cause of the severe grain boundary embrittlement observed in this material when aging at 950°F.

SUMMARY

The program goal of 55/60 HRC was achieved with a 0.25% C, 4% Mo, 14% Co, 10% Ni, balance Fe alloy. Increasing the solution treating temperature from 1800 to 2100°F resulted in a 1.5 HRC increase in peak aged hardness. Raising the C content from 0.23 to 0.29% increased the peak aged hardness by 3.0 HRC points. Thus, C is more effective in increasing peak aged hardness than raising the solution treating temperature above 1800°F. Aging times in excess of 1 hour (i.e. 5 and 8 hours) were observed to lower the temperature at which peak aged hardness occurred by approximately 50°F (i.e. from 950 to 900°F).

The 4% Mo, Cr-free modifications of AF 1410 that were evaluated in this study would have major practical limitations caused by Mo segregation. In addition the two alloys evaluated in this study have poor Charpy V-notch impact toughness following aging at 950°F. When tested in the solution treated condition, the use of higher solution treating temperatures resulted in improved impact toughness due to the dissolution of Mo-rich carbides which formed during overaging. It is believed that these carbides acted as sites for microvoid nucleation. Further work using both Auger spectroscopy and TEM/STEM is required to understand the mechanism responsible for the embrittlement that occurs when aging at 950°F.

ACKNOWLEDGEMENTS

The authors would like to express their sincere gratitude to the management at Carpenter Technology Corporation for their support of this research program; to Mr. J. Bowman for the SEM analyses; to Mrs. B. Messersmith for the microprobe analyses; to Mr. R. Razzano for performing the mechanical testing; to Mr. D. Englehart for general services; to Dr. G. Olson from MIT for the many hours of thought provoking discussion pertaining to the data generated in these studies; and to Mrs. D. Dunkelberger and Mrs. D. Heckman for their aid in

the preparation of this manuscript.

REFERENCES

1. P. M. Machmeier, et.al. "Development of a Strong Martensitic Steel Having Good Fracture Toughness," Metals Technology, August 1979, p. 291.

2. C. D. Little and P. M. Machmeier, "High Strength Fracture Resistant Weldable Steels," United States Patent 4,076,525, February 28, 1978.

3. M. L. Schmidt and M. Gore, "Solution Treatment Effects in AF 1410 Steel," paper presented at the U.S. Army 34th Annual Sagamore Materials Research Conference, Lake George, NY, August 30 - September 3, 1987.

4. W. M. Garrison and N. R. Moody, "The Influence of Inclusion Spacing and Microstructure on the Fracture Toughness of the Secondary Hardening Steel AF 1410," Met. Trans., Vol. 18A (1987), p. 1257.

Section II: Toughness

SHEAR FRACTURE OF ULTRAHIGH STRENGTH LOW ALLOY STEELS

GEORGE KRAUSS
Advanced Steel Processing and Products Research Center,
Colorado School of Mines, Golden, Colorado 80401

INTRODUCTION

One class of ultrahigh strength (UHS) steels consists of carbon steels which are austenitized, quenched to form martensite, and tempered at 200°C or below. These steels may contain several weight percent of alloying elements such as manganese, chromium, molybdenum and nickel, primarily to increase hardenability and to permit the hardening of heavy sections at moderate cooling rates which minimize distortion or quench cracking. Ultimate tensile strengths of the low alloy steels hardened and tempered at low temperatures range from 1380 MPa (200 ksi) to 2280 MPa (330 ksi) or more, depending on carbon content and the details of the heat treatment.

In parallel to the high strength of hardened UHS steels, toughness is moderate to low. As noted below, these steels are not always brittle, and even when very low energy is absorbed during fracture, the fracture occurs by ductile mechanisms.

The microstructures of the carbon low alloy UHS steels in the hardened condition are complex. Elements of structure which may influence deformation and fracture include the prior austenite grain boundary network (sometimes containing segregated impurity atoms, grain boundary carbide allotriomorphs, or particles which by design or inadvertently pin austenite grain boundaries), inclusion particles, carbide particles undissolved during austenitizing, martensite laths or plates, various arrangements of martensite laths or plates, retained austenite, transition carbides within martensite plates, and dislocation and twin substructures within the martensite.

A landmark paper by Lai et. al. (1) brought fracture mechanics directly into the complexity of structure and fracture of 1517 MPa (220 ksi) 4340 steel. Considerable discussion was generated when it was shown that plane strain fracture toughness testing showed improved toughness relative to CVN impact toughness testing of specimens austenitized at 1200°C. Among other suggestions, the beneficial effect of a reduction in the number of undissolved carbides (1) by high temperature austenitizing, and the detrimental effect of concentrations of embrittling elements at the coarse austenite grain boundaries (2) were proposed to explain the Lai et. al. results. As important as effects of structure on toughness, was the comparison of the fracture toughness and CVN impact test by Ritchie et. al. (2). They demonstrated that the differences between the tests were a function of notch root radius on toughness. The sharp crack of the fracture toughness test produces high tensile stresses close to the crack tip. If the characteristic or critical distance for fracture to a fracture sensitive structural element, as for example a coarse embrittled grain boundary, is large, the fracture toughness will be high. In the CVN test, the large root radius creates a stress field which acts over much greater distances, at the plastic elastic interface ahead of the notch. Within this large process zone, any set of fracture sensitive features, even widely separated embrittled grain boundaries, would result in low impact toughness.

From the mid-1970's our understanding of structure and fracture in UHS steels has steadily grown. The embrittlement phenomena leading to stress-induced fracture received most of the attention. For example, tempered martensite embrittlement (TME) restricts the tempering range for UHS steels and concurrently reduces strength and toughness. Also, the same conditions which promote TME exacerbate hydrogen embrittlement of high strength steels (3). Structural factors which have been related to TME and brittle fracture of UHS steels include segregated impurity atoms (especially phosphorus) (3-5), various types of carbide arrays formed during heat treatment (6,7), the thermal decomposition of retained austenite (8,9), upper bainitic microstructures (10), and inclusion particles (11). However, even with the reduction of segregation-prone impurity elements and inclusions, there are more than enough inherent features of hardened UHS steels to produce low toughness fracture at high strength levels.

The large list of microstructural features which influence deformation and fracture of UHS steels can be divided into two groups: particles at which cracks initiate, and features which control the deformation and strain hardening of the hardened matrix. The types of particles related to various brittle fracture mechanisms of UHS steels have been well characterized in the above cited work, but the structural features which control strain hardening have received little attention to date. The purpose of this paper, after the identification and separation of brittle fracture mechanisms, is to discuss the low toughness ductile fracture of UHS steels, sometimes referred to as shear instability. The particle arrays at which microvoid initiation occurs and the structural features of the tempered martensite matrix, i.e. dislocation/transition carbide substructures and retained austenite, which influence strain hardening will be discussed relative to ductile fracture in UHS steels of medium and high carbon content.

TOUGHNESS AND SHEAR FRACTURE

Figure 1 shows the CVN impact toughness of three medium carbon steels and a high carbon steel as a function of tempering temperature. High and low phosphorus heats of each steel were tested. The compositions of these steels are listed in Table I.

TABLE I - Compositions of Alloys in Figure 1

Steel	C	Mn	Si	P	S	Cr	Mo	Al
4130 LP	0.30	0.57	0.25	0.002	0.005	1.00	0.19	0.05
4130 HP	0.30	0.58	0.26	0.017	0.007	0.99	0.19	0.05
4140 LP	0.41	0.58	0.26	0.002	0.006	0.97	0.19	0.05
4140 HP	0.41	0.57	0.26	0.018	0.006	0.99	0.20	0.05
4150 LP	0.52	0.58	0.26	0.002	0.005	1.00	0.20	0.05
4150 HP	0.50	0.58	0.24	0.019	0.005	0.99	0.19	0.05
52100LP	1.03	0.45	0.26	0.009	0.022	1.51	---	---
52100HP	1.09	0.46	0.26	0.023	0.017	1.52	---	---

The microstructures of interest in this paper are those which are produced by tempering between 150 and 200°C. After tempering in this temperature range, an optimum balance of high strength and toughness is achieved for a given carbon level, and the microstructure consists of retained austenite and tempered martensite. Tempering at higher temperatures not only lowers strength but also lowers impact toughness, as shown in Figure 1. The CVN test with its set specimen size, large notch root radius, and high loading rate varies significantly from plane strain fracture toughness testing, as discussed in the INTRODUCTION, but CVN

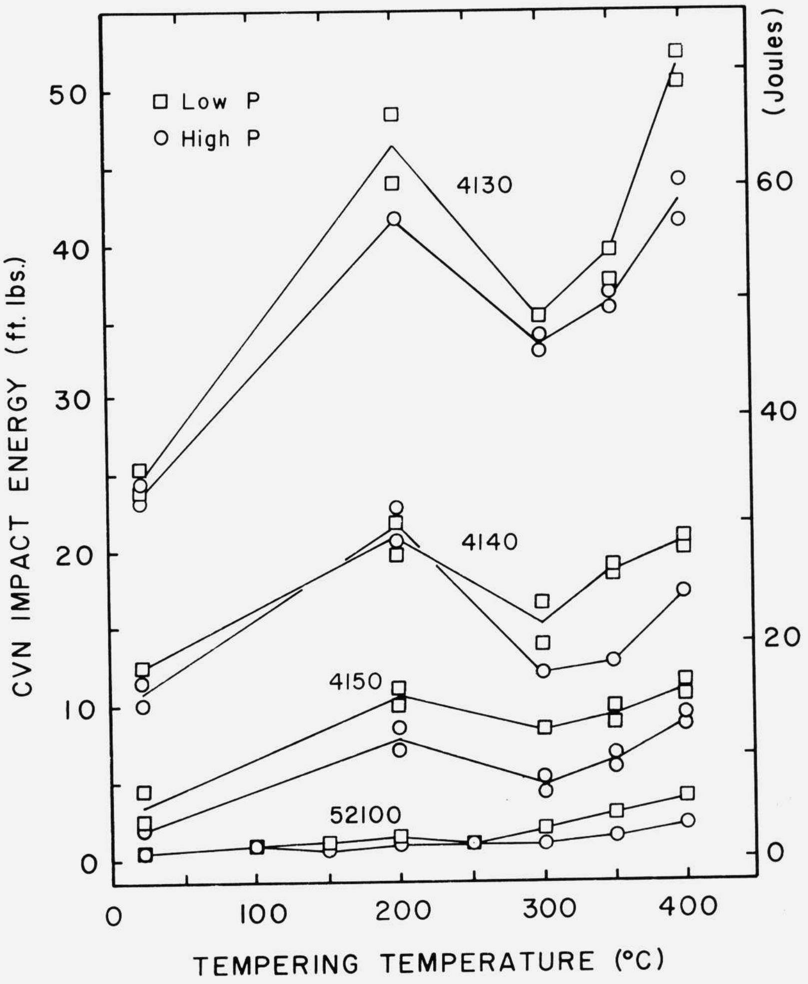

Figure 1. CVN Impact Energy for several low alloy carbon steels quenched to form martensite and tempered as noted. Compositions are listed in Table I.

and fracture toughness data often, but not always tend to correlate. Figure 2 shows that CVN energy absorbed and K_{IC} for quenched and tempered 52100 steel track closely (12). Low toughness fracture occurs after tempering at low temperatures and a divergence of toughness due to phosphorus segregation occurs with increasing temperature (13).

The fracture of specimens tempered between 150 and 200°C, especially when the complicating effects of phosphorus are minimized and carbon is held in the medium range, tends to occur by shear along the slip line field at the root of the Charpy V-notch. Figures 3 (a), (b), and (c) show schematically the development of the process zone in a CVN specimen relative to P_{GY} or general yielding of the specimen and Figures (d), (e) and (f) show fracture associated with elastic, elastic-plastic, and ductile fracture modes. The UHS steels tend to fail by brittle elastic and elastic-plastic fracture modes. The brittle fractures develop with a minimum of plastic deformation, usually in some manifestation of TME where an extensive intergranular or transgranular carbide network, sometimes with an impurity-reduced interface cohesive strength, lowers fracture strength. By careful selection of tempering temperature, steel carbon content, and reduction of phosphorus content, the brittle, stress-limited modes of UHS steel fracture can be minimized.

Thus when structural conditions which cause brittle, elastic fracture are avoided, fracture in medium carbon UHS steels develops under elastic-plastic conditions, and ductile fracture occurs by microvoid nucleation, void growth, and void coalescence (16). Specifically, in CVN specimens, plastic deformation occurs and fracture initiates by flow localization along slip lines at the root of the notch before following the centerline of the specimen. Figure 4 shows almost symmetrical development of slip line shear cracks in a 4130 steel tempered at 300°C, and Figure 5 shows a shear zone looking down on the notch region of a 4340 specimen tempered at 200°C. Fracture in the 4130 steel continued by zig-zag ductile tearing (17) and in the 4340 steel by fine scale microvoid coalescence (18).

The slip line initiation fracture zone reflects changes in microstructure, strength, and stress state. For example, the size of the shear zone in 4130 and 4140 specimens tempered at 200°C is much larger than in as-quenched

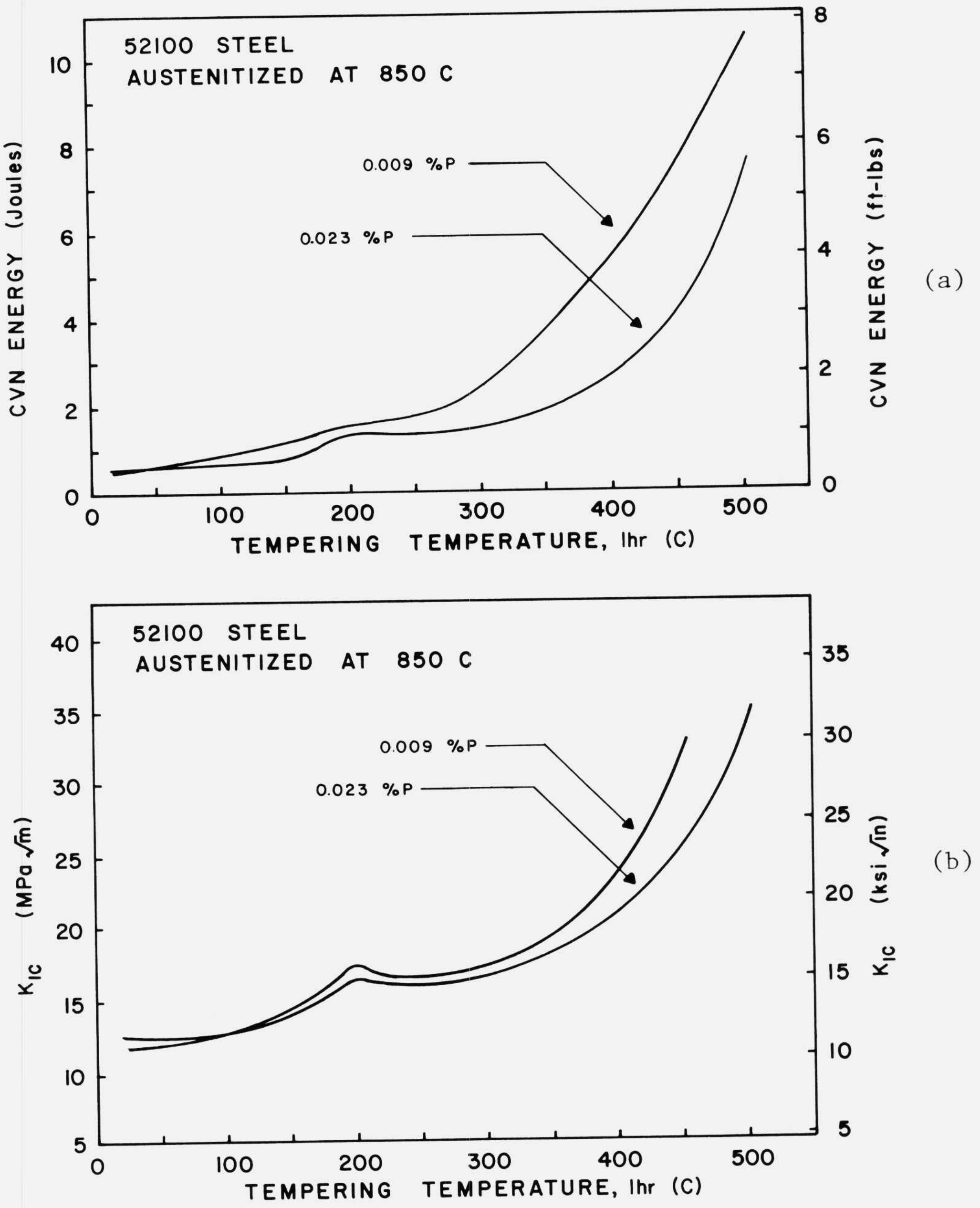

Figure 2. Toughness as a function of tempering temperature of 52100 steel oil quenched from 850°C. (a) CVN Impact Energy, (b) Fracture toughness (12).

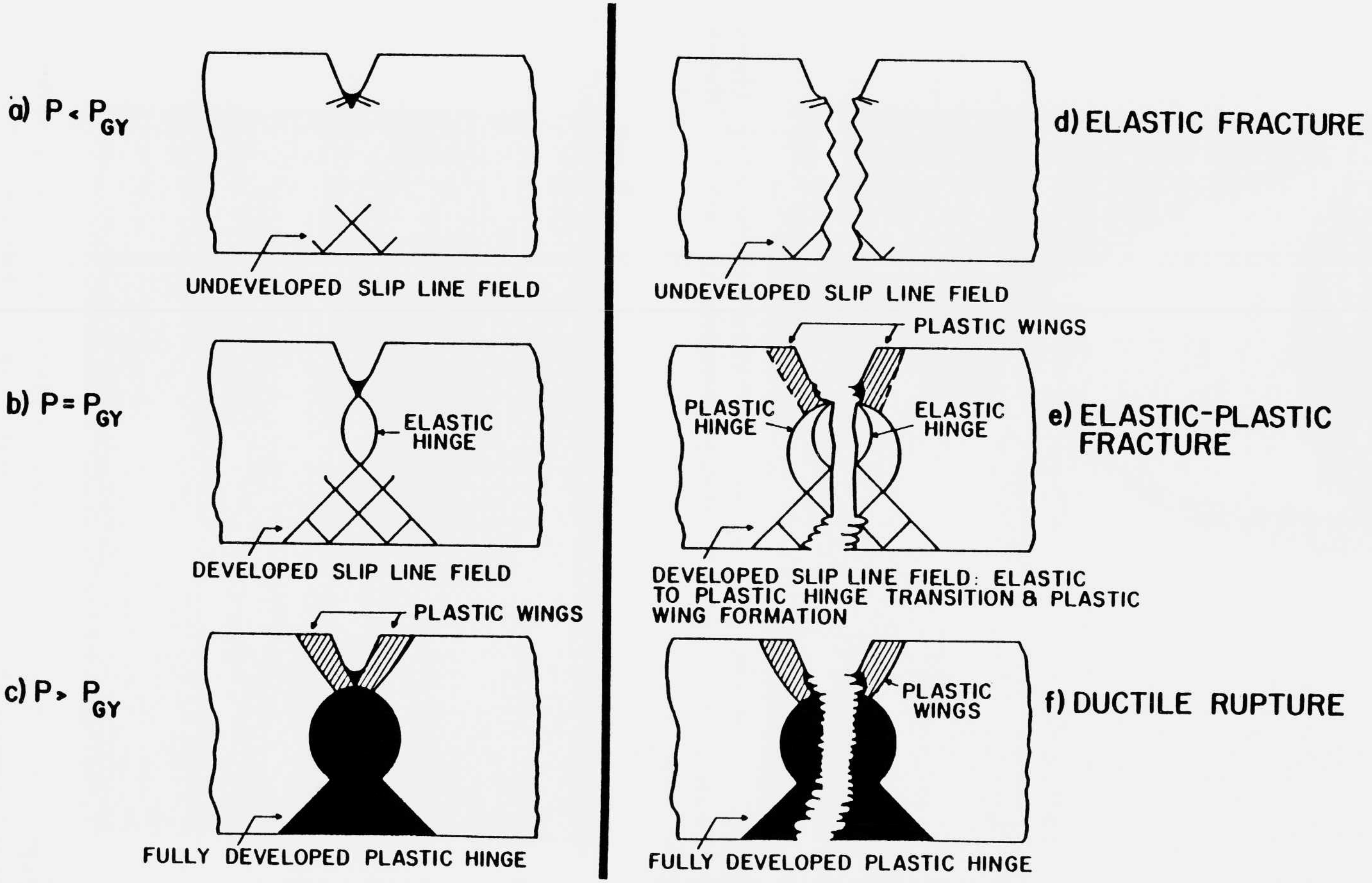

Figure 3. The extent of process zone development in CVN specimen as a function of load, (a) to (c), and various types of fracture (d) to (f) (14,15).

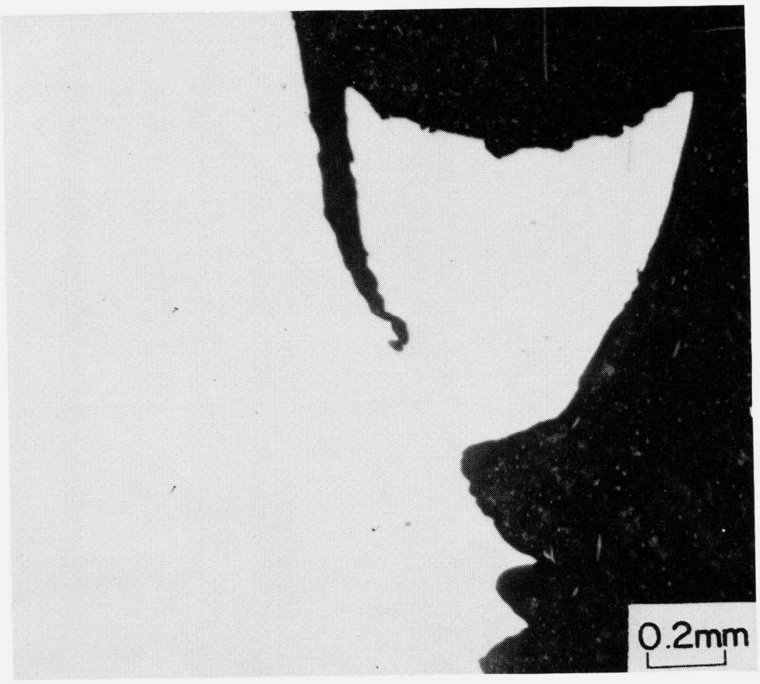

Figure 4. Example of shear initiation along slip lines at notch root in LP4130 steel tempered at 300°C. Notch is at top (17).

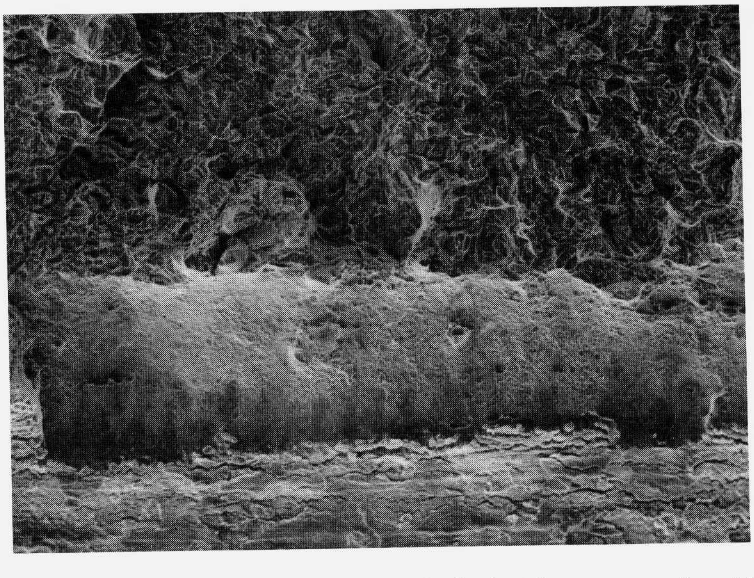

Figure 5. Top view of shear initiation zone in 4340 steel tempered at 200°C. Notch is at bottom. SEM micrograph (18).

specimens of the same steels (7,17). The shear zones in CVN specimens broken at room temperature decrease in size with increasing carbon content. In 52100 CVN specimens, quenched from 850°C and tempered between 150 and 200°C, there is no shear zone even though, as shown below, the fracture occurs by very fine microvoid initiation and coalescence on the specimen centerline. Firrao et. al. (19) evaluated initiation shear lip formation as a function of notch root radius and austenitizing temperature in CVN type 4340 specimens. Sharp cracks or notches do not show shear lips, but any notch radius above 0.07mm produced initiation shear lips with the size of the lip increasing with root radius. The shear lip size was directly related to crack initiation resistance by means of J-integral toughness. Specimens step quenched from 1200°C showed no shear lips, the fracture initiation surfaces being characterized primarily by brittle intergranular fracture. Finally in the lower strength, lower carbon UHS steel 4130, Zia-Ebrahimi et. al. (20) identified a variant of ductile crack initiation which required ductile tearing plus shearing in the slip line field below the notch.

PARTICLES AND SHEAR FRACTURE

The shear fracture initiation of UHS steels appears to be related to dispersions of fine spheroidized particles. Figure 6 shows particles extracted from a shear initiation surface of 4130 steel (17). Many of the shear dimples or microvoids contain spherical particles about 0.1μm or less in diameter. These particles appear to have been retained during austenitizing of the 4130 steel. The microvoids range in size from 0.2μm to several microns. The voids span several martensite laths and appear to form independent of the morphology and orientation of the martensite laths and packets.

Figure 7 shows a carbon extraction replica taken from the overload fracture surface of a high carbon steel intercritically austenitized to retain a high density of spheriodized carbide particles (21). The fracture surface consists of fine shallow dimples, each of which contains a spheroidized carbide particle. This type of specimen has very low impact and fracture toughness, but nevertheless fails in a ductile mode.

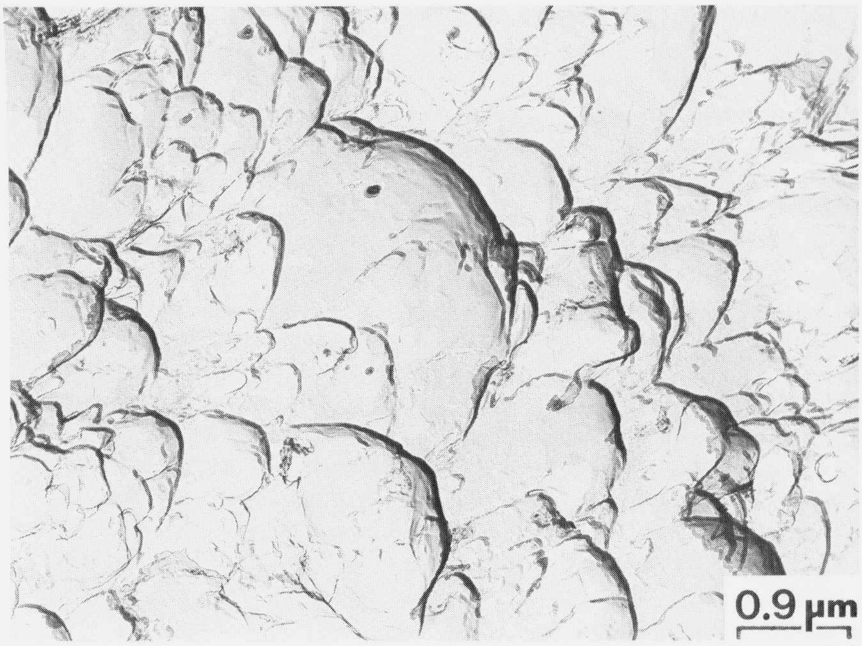

Figure 6. Extracted spherical carbides and microvoids on dimples from shear initiation zone of 4130 steel specimen. TEM micrograph of carbon extraction replica (17).

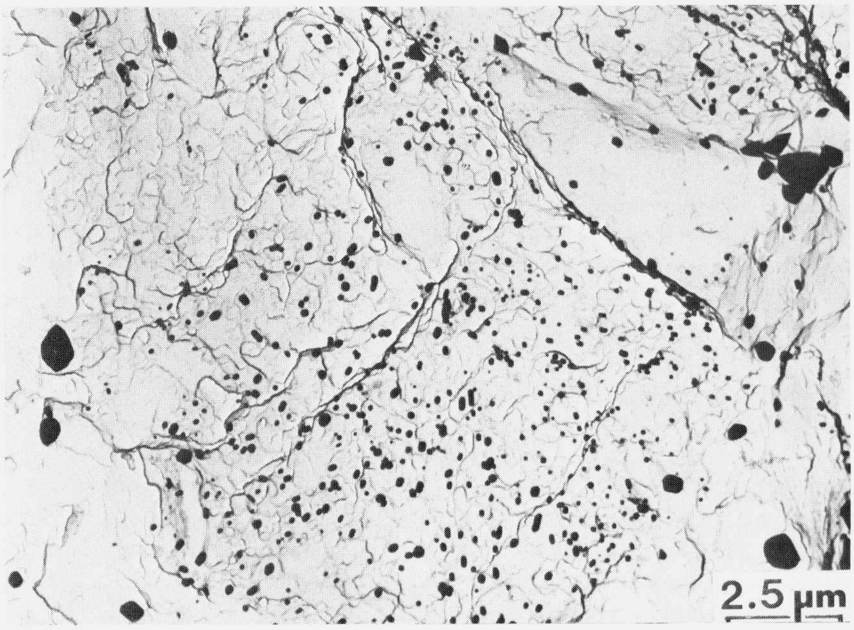

Figure 7. Extracted spherical carbides and microvoids from fracture surface of 0.85C steel. TEM micrograph of carbon extraction replica (21).

Generally the shear fracture of UHS is associated with high densities of fine, dispersed particles. There is however evidence that distributions of coarser particles superimposed on finer particle distributions can affect the toughness associated with ductile rupture of UHS steels. In one set of experiments, Garrison (11,22) found that the best fracture toughness in a set of 0.4 pct C steels, quenched from 900°C and tempered at 200°C, other structural features being equal, was associated with the alloy which had the coarsest and most widely spaced sulfide inclusion particles. He suggests that the critical crack tip opening displacement scales as:

$$\delta_{IC} \simeq X_o \left(\frac{R_v}{R_\ell}\right)\Bigg|_{R_o} \qquad (1)$$

where X_o is the average three-dimensional distance between sulfides, R_v is the void radius, R_ℓ is the radius of the sulfide nucleating the void, and R_o is the average sulfide size. Thus if the particles are widely spaced and the voids associated with second phase particles grow to large size, the crack tip opening displacement and therefore the toughness of the steel should be relatively high. By similar arguments, even in the absence of coarse particles, uniform fine carbide dispersions with coarse spacing would be expected to have higher toughness. Also, fine particles of planar morphology with a high interfacial area and particles with segregated impurities atoms at the particle-matrix interfaces would be expected to show lower toughness. The former condition accounts for aluminum nitride embrittlement (23) and the latter condition was proposed as the cause for the lower impact toughness of the high phosphorus 4130 steel, Figure 1, relative to the low phosphorus steel, both of which failed by shear initiation (7).

Figure 8 shows the results of another set of experiments performed to evaluate the superposition of coarse particle distributions on finer particle distributions in 52100 steel heat treated to identical hardness of HRC 58 (24,25). The various coarse particle distributions were produced by various isothermal pretreatments. Phosphorus was selected as a variable because of its segregating tendencies and because it has been found to stimulate grain boundary carbide allotriomorphic growth (26). Figure 8 shows a relatively

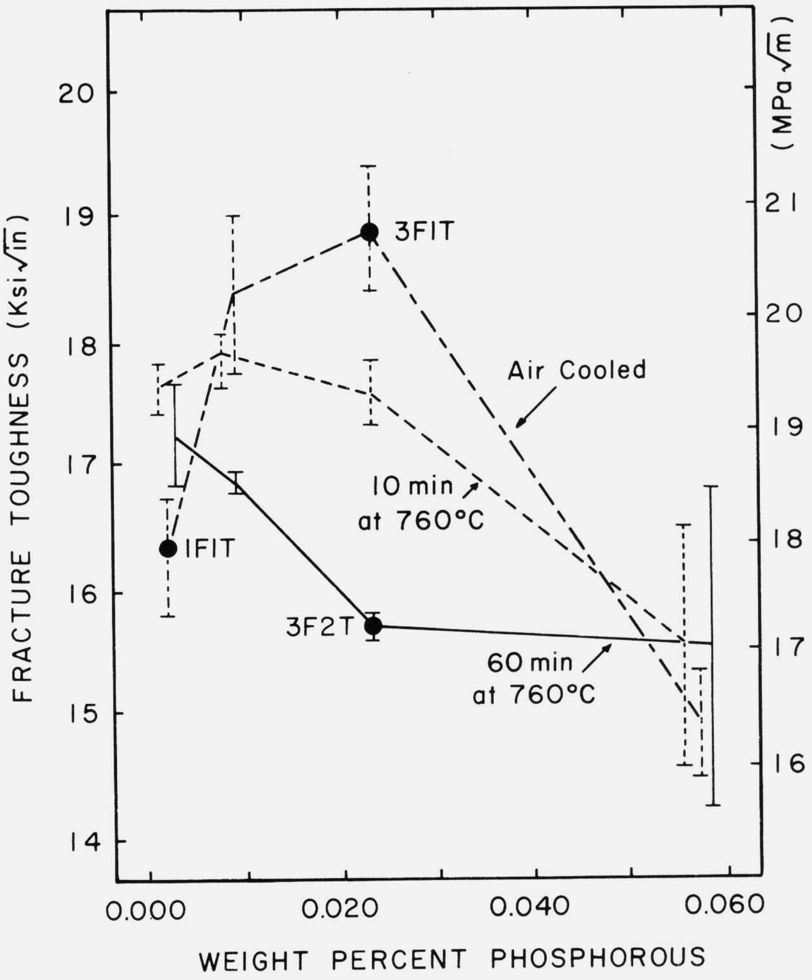

Figure 8. Fracture toughness vs phosphorus content for 52100 steel specimens given various pretreatments to produce different, coarse carbide dispersions and then all quenched from 850°C and tempered at 175°C (24,25).

wide variation in the fracture toughness of a high carbon UHS steel. The higher toughnesses were associated with carbide dispersions with coarse, widely spaced, partially spheroidized carbides superimposed on the fine carbides retained by intercritical austenitizing at 850°C. Low fracture toughness was associated with either continuous or partially continuous networks of grain boundary carbides as in the 0.06 pct phosphorus specimens, or when no coarse carbides were present, as in the 0.002 pct phosphorus specimens. Despite the large variety of microstructures represented in Figure 8, the fracture toughness of this UHS steel shows remarkably little variation. Thus, other factors must contribute to the very low toughness of the hardened 52100 steel as shown in Figures 1 and 7. The next section discusses the effects of matrix structure and strain hardening, which, together with the particle dispersions, create resistance to the shear fracture of UHS steels.

STRAIN HARDENING AND STRUCTURE OF UHS STEELS

A number of structural features influence the flow stresses and strain hardening of UHS steels tempered at low temperatures. The translation of the carbon content into substructural features, as discussed below, dominates the deformation behavior of these steels. Substitutional solid solution strengthening by such elements as chromium, nickel and molybdenum generally has little effect on the maximum strength and hardness achievable by martensitic transformation (27,28), although these elements markedly affect tempering, especially at high temperatures (29). Austenitic grain size (30) and martensite packet size (31,32) also have been demonstrated to have small but significant effects on the strength of martensitic structures. In medium carbon steels, the martensite laths are quite fine and introduce a very high boundary area per unit volume, on the order of 60,000 cm^{-1}, into the microstructure. However, many of these boundaries are low angle (33) and therefore may be considered to contribute merely to the overall dislocation substructure of the martensitic structure. Lath width distributions appear to be insensitive to austenitic grain size (31) and carbon content (34).

Figures 9 and 10 show respectively, the tensile and compressive flow stresses of martensite tempered at 150°C as a function of carbon content (35). The steels tested

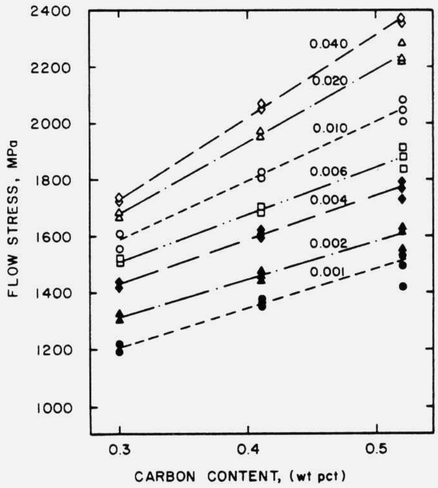

Figure 9. Tensile flow stresses at various true plastic strains for 41XX steels tempered at 150°C (35).

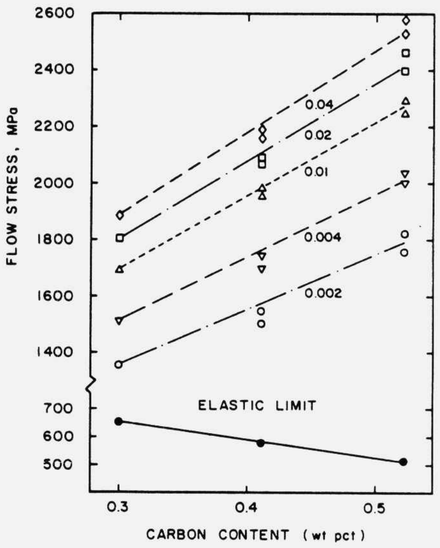

Figure 10. Compressive flow stresses at various true plastic strains for 41XX steels tempered at 150°C. Elastic limits were determined for specimens tempered at 200°C (35).

were 4130, 4140 and 4150, and therefore contained the same amounts of the substitutional alloying elements manganese, chromium and molybdenum. Also, the austenite grain and martensite packet sizes were about the same for all of the steels. In the carbon range shown, flow stresses increase directly with carbon content, and the divergence of the curves taken at low and high offset strains indicates that strain hardening increases with increasing carbon content of the tempered martensite.

In the 41XX experiment, three structural features, all below the resolution of the light microscope, varied with carbon content: the dislocation substructure within the martensite laths, the transition carbide density, and the interlath retained austenite content. Figure 11 shows the features in a specimen of 4130 quenched to martensite and tempered at 150°C. Overlapping eta-carbide (36,37) and retained austenite diffraction spots have been used for this dark field transmission electron micrograph. The retained austenite is resolved as the white bands between the martensite laths. Amounts of 1.4, 3.8, and 5.9 vol. pct. interlath retained austenite were measured by Mossbauer Effect Spectroscopy (38) for the 4130, 4140 and 4150 steels respectively. The dislocation substructure is too dense to be resolved but appears to be intimately tied to the transition carbides which have uniformly precipitated with the martensite laths, Figure 11. A higher magnification view of the eta transition carbide dispersion within a martensite lath, Figure 12, shows that the carbides are present as rows of very fine, discrete particles, only 2 to 4nm in size. With increasing carbon content, the spacing of the transition carbide clusters decreases.

Figure 10 shows that the elastic limit of the 41XX steels decreases with increasing carbon content. This decrease in elastic limit correlated directly with the increase in retained austenite with increasing steel carbon content. Additional work (39,40) shows that elastic limit drops even further as retained austenite increases in hardened 52100 steels and alloy steels containing 0.8 pct C. However in the 41XX steels the retained austenite transformed by stress-assisted mechanisms in the very earliest stages of deformation while the higher carbon steels with more substantial quantities (15 to 30 vol pct) of retained austenite the austenite transformed to martensite by strain-assisted mechanisms at much higher strains. In both cases the transformation of the retained

Figure 11. Fine structure of 4130 steel tempered at 150°C. Darkfield transmission electron micrograph. Courtesy of M. Losz.

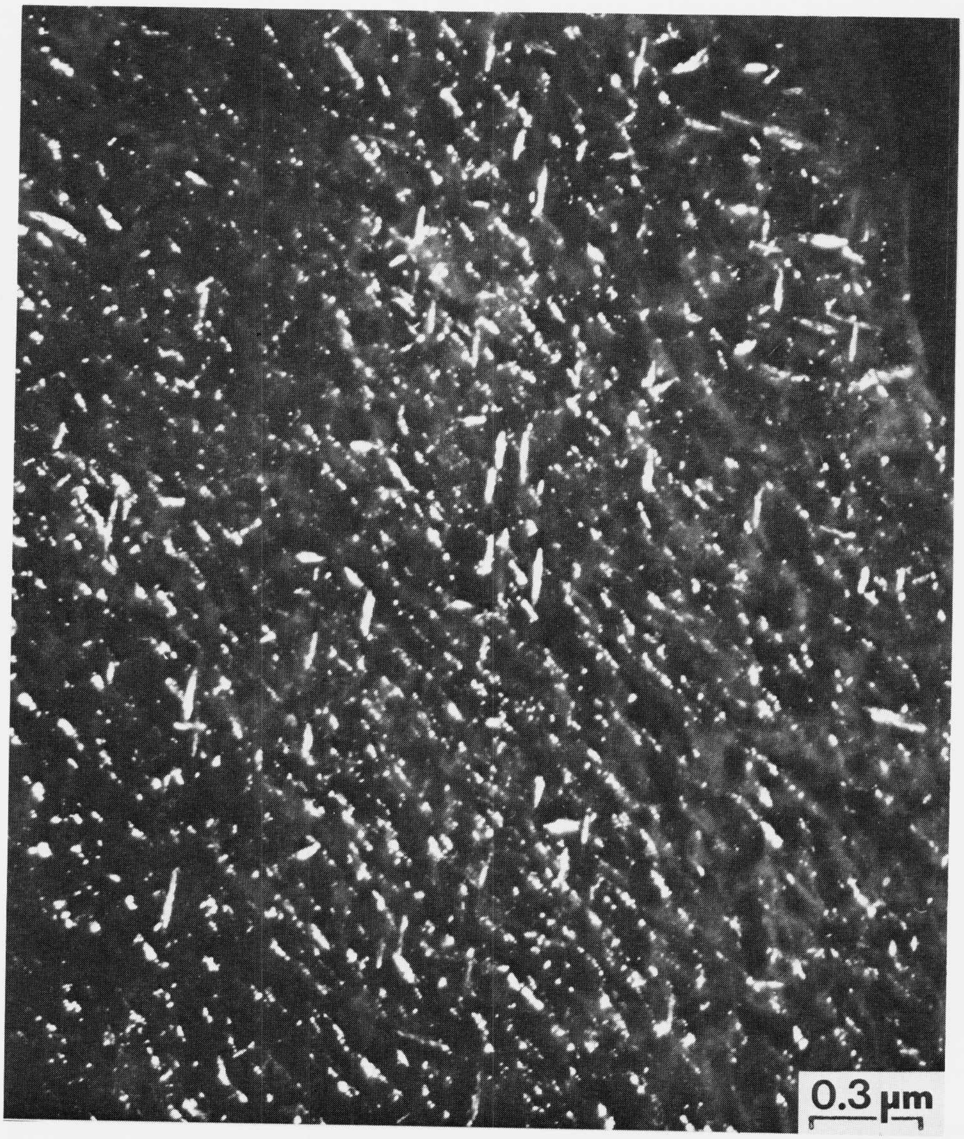

Figure 12. Fine intralath structure within a lath of 4130 martensite tempered at 150°C. Darkfield transmission electron micrograph. Courtesy of M. Losz.

austenite to martensite under deformation increased the strain hardening of the composite austenite-tempered martensitic microstructures (40,41).

SUMMARY DISCUSSION: STRUCTURE, STRAIN HARDENING, AND FRACTURE

Ultrahigh strength carbon steels, in the absence of embrittling networks or arrays of segregated impurity atoms and carbide particles, fail by instability to ductile shear fracture. Thus it is the continuity of second phase particle distributions which determines whether a UHS steel will fail by brittle or ductile micromechanisms. The ductile fracture initiates on planes of maximum shear stress by microvoid formation at both large and small dispersed second phase particles, either carbides or inclusions. Resistance to shear instability and fracture energy absorbed decrease with increasing density or decreasing spacing of dispersed particles. The deformation of the complex microstructure of low-temperature tempered UHS steels controls the rate at which stresses and strains build at particle interfaces. As alloy carbon content increases, retained austenite increases, and the density of the very fine transition carbide-dislocation substructure within the martensite increases, both factors which drive up strain hardening rates. The high strain hardening rates contribute to the very low impact toughness of the high carbon steels tempered in the UHS range of 150 to 200°C, as shown in Figure 1. In fact, in the 52100 steel, the slip line initiated shear elastic-plastic fracture, Figure 3(e) is replaced by largely elastic, stress-controlled fracture, Figure 3(d), even though the micromechanism of fracture in specimens with dispersed particles is still by microvoid initiation and coalescence.

Although the UHS carbon steels have complex microstructures with many structural components, the latter fall into two groups: the particles at which shear fracture initiates and the structural elements which control matrix strain hardening. Both sets of structural factors must be considered to optimize design of new steels or the selection of existing steels and heat treatments for new applications which require high strength and good toughness. Elements of ductile fracture, i.e., microvoid nucleation, growth and coalescence, appear to be well established by mechanics and fractography. However, details of the ductile fracture process still must be tied to the largely unexplored area of strain hardening of the complex matrix structures and the interaction of strain hardening with the particle dispersions which make up high strength tempered martensite. Nevertheless, by virtue of the low tempering temperatures treatments applied to UHS, it is now clear that the UHS microstructures are truly composite microstructures consisting of tempered martensite and retained austenite. Both components of the microstructure contribute significantly to strain hardening and fracture behavior of this unique class of materials.

ACKNOWLEDGEMENTS

Much of this information was developed with my students and colleagues, and I am grateful for their experimental contributions and theoretical insights. Financial support for many of the investigations was provided by the Army Research Office. I thank especially Mimi Vogt for her assistance in preparing this paper.

REFERENCES

1. G.Y. Lai, W.E. Woodd, R.A. Clark, V.F. Zackay and E.R. Parker. The Effect of Austenitizing Temperature on the Microstructure and Mechanical Properties of As-Quenched 4340 Steel. Metallurgical Transactions, vol. 5, 1974, pp. 1663-1670.

2. R.O. Ritchie, B. Francis, and W.L. Server. Evaluation of Toughness in AISI 4340 Alloy Steel Austenitized at Low and High Temperatures. Metallurgical Transactions A, vol. 7A, 1976, pp. 831-838.

3. S.K. Banerji, C.J. McMahon, Jr., and H.C. Feng. Intergranular Fracture in 4340-Type Steels: Effects of Impurities and Hydrogen. Metallurgical Transactions A, vol. 9A, 1978, pp. 237-247.

4. E.B. Kula and A.A. Anctil. Tempered Martensite Embrittlement and Fracture Toughness in SAE 4340 Steel. Journal of Materials, vol. 4, 1969, pp. 817-841.

5. G. Krauss. The Microstructure and Fatigue of a Carburized Steel. Metallurgical Transactions A, vol. 9A, 1978, pp. 1527-1535.

6. J.P. Materkowski and G. Krauss. Tempered Martensite Embrittlement in SAE 4340 Steel. Metallurgical Transactions A, vol. 10A, 1979, pp. 1643-1651.

7. F. Zia-Ebrahimi and G. Krauss. Mechanisms of Tempered Martensite Embrittlement in Medium-Carbon Steels. Acta Metallurgica, vol. 32, 1984, pp. 1767-1777.

8. R.M. Horn and R.O. Ritchie. Mechanisms of Tempered Martensite Embrittlement in Low Alloy Steels. Metallurgical Transactions A, vol. 9A, 1978, pp. 1039-1053.

9. G. Thomas. Retained Austenite and Tempered Martensite Embrittlement. Metallurgical Transactions A, vol. 9A, 1978, pp. 439-450.

10. E.R. Parker. Interrelations of Compositions, Transformation Kinetics, Morphology, and Mechanical Properties of Alloy Steels. Metallurgical Transactions A, vol. 8A, 1977, pp. 1025-1042.

11. W.M. Garrison, Jr. The Effects of Silicon and Nickel Additions on the Sulfide Spacing and Fracture Toughness of a 0.4 Carbon Low Alloy Steel. Metallurgical Transactions A, vol. 17A, 1986, pp. 669-678.

12. D.L. Yaney. The Effects of Phosphorus and Tempering on the Fracture of AISI 52100 Steel. M.S. Thesis, Colorado School of Mines, 1981.

13. C.L. Briant and S.K. Banerji. Tempered Martensite Embrittlement in Phosphorus Doped Steels. Metallurgical Transactions A, vol. 10A, 1979, pp. 1729-1737.

14. M.J. Leap, D.K. Matlock and G. Krauss. Correlation of the Charpy Test to Fracture Mechanics in a Vanadium Modified 1045 Steel in Fundamentals of Microalloying Forging Steels, Edited by G. Krauss and S.K. Banerji, TMS-AIME, 1987, pp. 113-152.

15. M.J. Leap. The Effects of Forging on the Microstructural Development, Strength and Dynamic Fracture Behavior of Microalloyed Ferrite-Pearlite Steels. M.S. Thesis, Colorado School of Mines, 1987.

16. R.C. Bates. Modeling of Ductile Fracture by Microvoid Coalescence for the Prediction of Fracture Toughness in Fracture: Interactions of Microstructure, Mechanism, Mechanics. Edited by J.M. Wells and J.D. Landes, TMS-AIME, 1984.

17. F. Zia-Ebrahimi and G. Krauss. The Evaluation of Tempered Martensite Embrittlement in 4130 Steel by Instrumented Charpy V-Notch Testing. Metallurgical Transactions A, vol. 14A, 1983, pp. 1109-1119.

18. Gu Baozhu and G. Krauss. The Effect of Low Temperature Isothermal Treatments on the Fracture of 4340 Steel. Journal of Heat Treating, vol. 4, 1986, pp. 365-372.

19. D. Firraro, J.A. Begley, G. Silva, R. Roberti, and B. DeBenedetti. The Influence of Notch Root Radius and Austenitizing Temperature on Fracture Appearance of As-Quenched Charpy-V Type AISI 4340 Steel Specimens. Metallurgical Transactions A, vol. 13A, 1982, pp. 1003-1013.

20. F. Zia-Ebrahimi, D.K. Matlock, and G. Krauss. On Ductile Crack Initiation in Notched Bend Specimens. Scripa Metallurgica, vol. 16, 1982, pp. 987-992.

21. P.T. Purtscher and G. Krauss. Fracture Toughness and Microstructure of a Martensitic High Carbon Alloy Steel in Fracture, Interactions of Microstructure, Mechanics, Mechanisms, Mechanics. Edited by J.M. Wells and J.D. Landes, TMS-AIME, 1984, pp. 179-194.

22. W.M. Garrison, Jr. A Micromechanistic Interpretation of the Influence of Undissolved Carbides on the Fracture Toughness of a Low Alloy Steel. Scripta Metallurgica, vol. 20, 1986, pp. 633-636.

23. J.A. Wright and A.G. Quarrell. Effects of Chemical Composition on the Occurrence of Intergranular Fracture in Plain Carbon Steel Castings Containing Aluminum and Nitrogen. Journal of the Iron and Steel Institute, vol. 197, 1962, pp. 299-307.

24. F.S. Shen and G. Krauss. The Effect of Phosphorus Content and Proeutectoid Carbide Distribution on the Fracture Behavior of 52100 Steel. Journal of Heat Treating, vol. 2, 1982, pp. 238-349.

25. F.S. Shen, E.L. Brown, and G. Krauss. The Contribution of Physical Metallurgy to Heat Treatment Particles. Proceedings of Third International Conference on Heat Treatment of Material, Book No. 310, 1984, The Metals Society, 5.24-5.31.

26. T. Ando and G. Krauss. The Effect of Phosphorus Content on Grain Boundary Cementite Formation in AISI 52100 Steel. Metallurgical Transactions A, vol. 12A, 1981, pp. 1283-1290.

27. P.G. Winchell and M. Cohen. The Strength of Martensite. Transactions ASM, vol. 55, 1962, pp. 347-361.

28. M. Cohen. Strengthening Mechanisms in Steel. Transactions Japan Institute of Metals, vol. 9, 1968, Supplement.

29. R.A. Grange, C.R. Hibral, and L.F. Porter. Hardness of Tempered Martensite in Carbon and Low-Alloy Steels. Metallurgical Transactions A, vol. 8A, 1977, pp. 1775-1785.

30. R.A. Grange. Strengthening Steel by Austenite Grain Refinement. Transactions ASM, vol. 59, 1966, pp. 26-48.

31. T. Swarr and G. Krauss. The Effect of Structure on the Deformation of As-Quenched and Tempered Martensite in Fe-0.3 pct C Alloy. Metallurgical Transactions A, vol. 7A, 1976, pp. 41-48.

32. M.J. Roberts. Effect of Transformation Substructure on the Strength and Toughness of Fe-Mn Alloys. Metallurgical Transactions, vol. 1, 1970, pp. 3287-3294.

33. C.A. Apple, R.N. Caron and G. Krauss. Packet Microstructure in an Fe-0.2 pct C Martensite. Metallurgical Transactions, vol. 5, 1974, pp. 593-599.

34. A.R. Marder. The Morphology and Strength of Iron-Carbon Martensite. Ph.D. Dissertation, Lehigh University, Bethlehem, PA, 1968.

35. Gu Baozhu, J.M.B. Losz and G. Krauss. Substructure of Flow Strength of Low-Temperature Tempered Medium Carbon Martensite. Proceedings of the International Conference on Martensitic Transformations, 1986, The Japan Institute of Metals, pp. 367-374.

36. Y. Hirotsu and S. Nagakura. Electron Microscopy and Diffraction Study of the Carbide Precipitated at the First Stage of Tempering of Martensitic Medium Carbon Steel, Transactions Japan Institute of Metals, vol. 15, 1974, pp. 129-134.

37. D.L. Williamson, K. Nakazawa, and G. Krauss. A Study of the Early Stages of Tempering in an Fe-1.2 pct C Alloy. Metallurgical Transactions A, vol. 10A, 1979, pp. 1351-1363.

38. D.L. Williamson, R.G. Schupmann, J.P. Materkowski and G. Krauss. Determination of Small Amounts of Austenite and Carbide in a Hardened Medium Carbon Steel by Mossbauer Spectroscopy. Metallurgical Transactions A, vol. 10A, 1976, pp. 379-382.

39. M.A. Zaccone, J.B. Kelley and G. Krauss. Fatigue and Strain Hardening at High Carbon Martensite-Austenite Composite Microstructures. to be published in Proceedings of Materials '87, The Institute of Metals.

40. M.A. Zaccone. Flow Properties of High Carbon Tempered Martensite. M.S. Thesis, Colorado School of Mines, Golden, Colorado, 1987.

41. G.B. Olson. Transformation Plasticity and the Stability of Plastic Flow. in Deformation, Processing and Structure, Edited by G. Krauss, American Society for Metals, 1988.

THE ROLE OF SHEAR INSTABILITY IN BALLISTIC PENETRATION

JOHN F. MESCALL[1], HARRY ROGERS[2]
(1)U.S. Army Materials Technology Laboratory, Watertown, MA 02172-0001;
(2)Drexel University, Philadelphia, PA 19104.

INTRODUCTION

Our objective in this paper is to illustrate the role of adiabatic shear bands in penetration mechanics and to describe an experimental technique by means of which conditions for the incipient nucleation and subsequent growth of such localized bands may be determined. There is abundant experimental evidence to indicate that ballistic results are strongly influenced by the mechanical properties of the materials involved. A particularly instructive example of this is shown in Figure 1 (taken from Reference 1). Two sets of targets were made from the same steel alloy (4340), processed in the same way (VAR) but heat treated to two extremes of strength level, soft (HRC 20) and hard (HRC 52). These targets were of equal thicknesses and were impacted with blunt cylindrical projectiles over a range of velocities. Projectiles were made of the same material as the targets. Their diameters were equal to target thickness and their length was twice their diameter. Recovered targets were cross sectioned and etched.

Comparison of the results shown in Figure 1 reveals that both hard and soft targets fail in what ballisticians term a plugging mode. However, there are interesting differences. The softer target exhibits massive plastic flow and a deep crater forms prior to eventual perforation at a velocity slightly higher than that shown in Figure 1, (2,600 ft/sec). The harder target resists indentation for a much larger range of velocities. There is only a very shallow indentation at an impact velocity of 1,900 ft/sec (Figure 1b). One might easily infer, then, that the velocity required to perforate the harder target would be substantially higher than the 2,600 ft/sec required to perforate the softer one. It turns out, however, that above a critical velocity, an adiabatic shear band (visible in the cross section of the high strength target in Figure 1c) forms in the hard target and leads to "premature" failure at velocities only slightly higher than the value (2,400 ft/sec) shown in Figure 1c. Figure 2 shows the shear band developed in Figure 1 at a high magnification.

This diminished performance is directly attributable to this new mode of failure and illustrates one of the more subtle nuances of the role of material properties in this context. Generally speaking, increased strength or hardness in armor plate leads to increased ballistic performance. To show that the above reversal is not an isolated instance, consider the data shown in Figure 3. A non-dimensional measure of ballistic limit is plotted versus Brinnell hardness levels for two types of steel with the same chemical composition but processed in two different manners – vis-à-vis vacuum induction melted (VIM) and electroslag remelted (ESR). Targets were one-quarter inch in thickness and all were impacted by similar projectiles. As the target hardness is increased from BHN 250 to approximately BHN 450, target resistance increases dramatically.

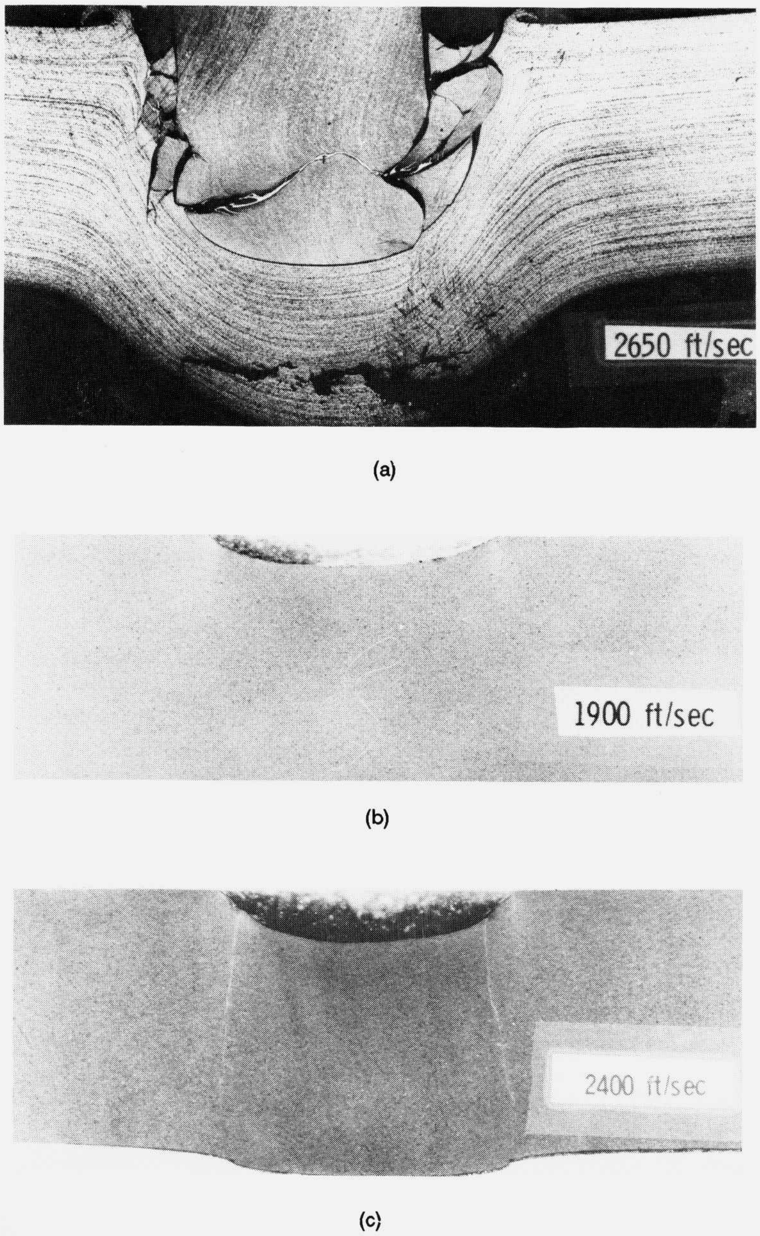

FIGURE 1. Cross sections of 4340 steel targets impacted by high strength blunt steel projectiles. Target hardness in (a) is HRC 20. In (b) and (c) hardness is HRC 52. Note differences in crater depth, differences in failure mode, and absence of shear bands in target of (a) and (b).

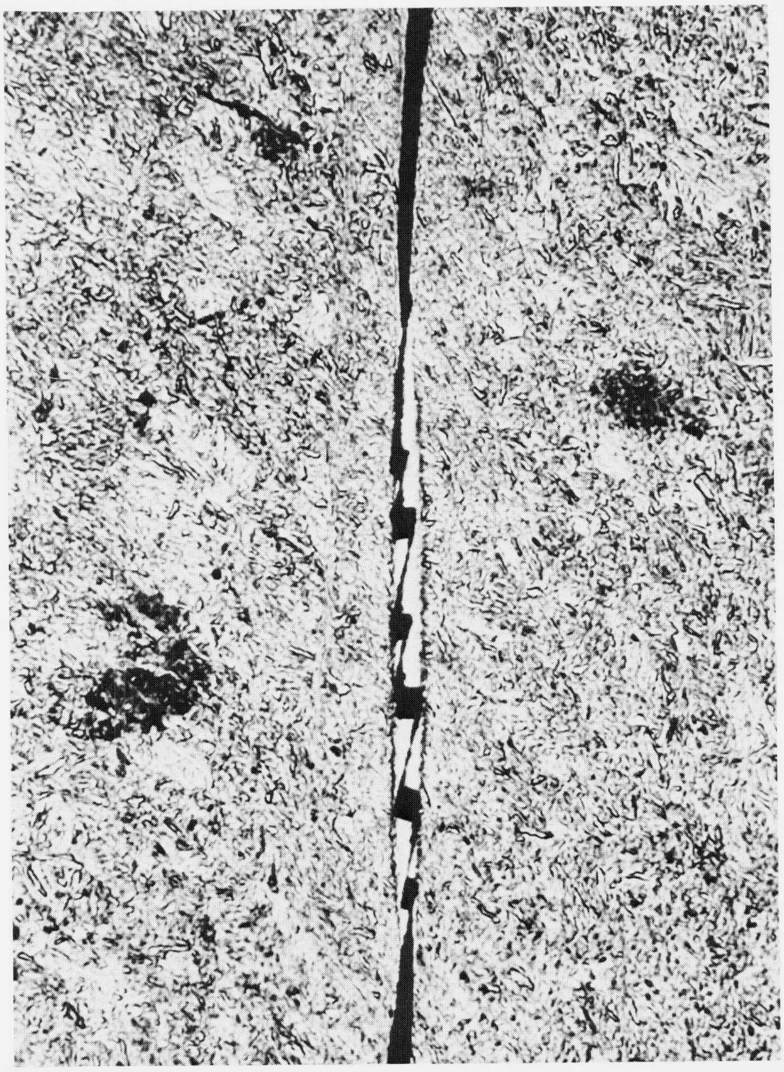

FIGURE 2. High magnification (500X) of white band of target of Figure 1c.

Beyond BHN 450, however, target performance drops even faster. Examination of recovered target cross sections reveals three distinct modes of failure: (a) large plastic flow similar to Figure 1a, (b) plugging in a shear mode similar to Figure 1c, and (c) discing which consists of delamination near the target rear surface along planes parallel to the impact face. Figure 3 shows that for both VIM and ESR steels, the drop in ballistic performance is clearly associated with the change in failure mode from plastic flow to shear band formation. Discing is seen only at very high strength levels and leads to even more reduction in performance. It is conjectured that discing is associated with low values of through-thickness toughness. This form of fracture should be distinguished from "spall" which is similar in appearance but is due to the development of large triaxial stress fields upon reflection of the initial compression shock wave from the free rear surface of the target. Peak stresses required to produce spall in steel targets shown in Figure 1 are roughly 30 kbar (450 ksi) which is considerably higher than the static tensile strengths of the steels of Figure 3. The assurance that such stresses are not achieved for the penetration-target interactions of Figure 3, is based on hydrocode simulations of these events (see, for example, Reference 1 and the Appendix).

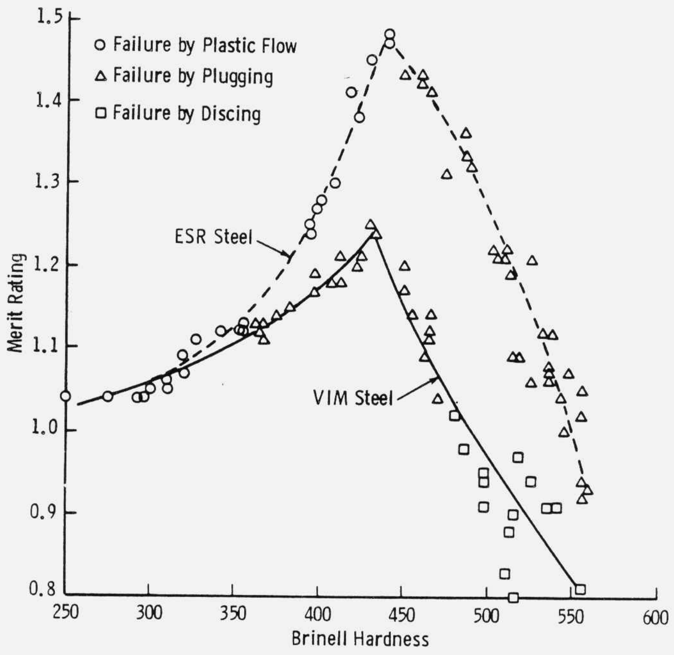

FIGURE 3. Ballistic merit rating versus hardness for targets of vacuum induction melted (VIM) and electroslag remelted (ESR) steels. Note precipitous decrease in ballistic performance once the failure mode involving adiabatic shear banding is encountered.

Clearly then, the material properties most significant for metal targets include dynamic work hardening for the first mode of failure, adiabatic shear onset and growth for the second failure mode, and dynamic toughness in the through-the-thickness sense of discing behavior. We shall address the measurement of the onset of adiabatic shear bands in this paper.

CHARACTERISTIC STRESS FIELDS

One of the unspoken difficulties concerning the identification of important material properties in ballistic problems is the fact that both the materials community and a large portion of the mechanics community are relatively unfamiliar with detailed stress and deformation histories experienced in such problems. This is not surprising if one considers the difficulty in obtaining relevant experimental data in a ballistics environment compared with obtaining corresponding data in static laboratory tests.

Perhaps the most obvious remark concerning characteristic stress fields under ballistic conditions is that they are dominated by very large compressive states which are found (by hydrocode computations as in the Appendix) to be divided into a brief initial stage followed by a long steady-state stage and terminated, in many cases, by low order tension fields. The peak stresses in Stage I are found to persist for a few microseconds and to be compressive with peak values on the order of

$$P = V(p_1c_1Xp_2c_2)/(p_1c_1 + p_2c_2) \qquad (1)$$

where V is impact velocity, p is density, c is sound speed, and P is stress. Convenient/consistent units are cm/μsec, gm/cc, and Mbars. This initial state does not persist for very long because of relief waves which enter from readily available free surfaces on the target impact face. Thus, the stress associated with Equation 1 does not propagate very far into the material, and conditions corresponding to a relatively long steady-state phase soon develop. Associated stress is given by the Bernoulli equation:

$$P = (pV^2)/2 \qquad (2)$$

where, again, P is stress, p is density, and V is the velocity of the projectile-target interface. Notice that for many impact problems there is close to an order of magnitude difference between Equations 1 and 2. In the example of the Appendix, where a high density penetrator (W or DU) attacks a steel target at a velocity of 0.12 cm/μsec (4,000 ft/sec), peak stresses in Phase I are roughly 350 kbar or 5 million psi; whereas, the peak stress in the steady-state phase is closer to 40 kbar (600,000 psi). The interface velocity V of Equation 2 depends strongly upon the relative impedances (density x sound speed) of projectile and target. However, for materials of the same or similar impedance, it turns out that to a good approximation, V is one-half the impact velocity. It should also be noted that in most ballistic impact problems a local process zone develops immediately in front of the penetrator. This zone moves in time, naturally, however, in spatial extent is confined to a region roughly one to two projectile diameters in width. Most of the physically interesting processes occur within this process zone; e.g., acceleration and material failure. Unfortunately, this zone is not physically observable and its details must be obtained via computer simulations, such as the Appendix.

MECHANISMS FOR ADIABATIC SHEAR NUCLEATION

The first reported observation of adiabatic shear bands was made by Zener and Holloman (2) in 1944. They conjectured that this localization of a shearing process arose because of the deformation-induced temperature rise at rapid rates of loading. Thermal softening, thus, overrode strengthening effects due to strain and strain-rate increases. This is still the conventional view of the process, although an alternative mechanism has recently been put forth by Cowie et al. (3). Based on the observation that in unconventional shearing tests performed at static and low strain rates (10^2/sec) they observed similar microscopic deformation patterns, they conclude that thermal softening can no longer be considered a dominant mechanism since there is adequate time for heat dissipation at static test rates. They propose that a void softening mechanism is operative instead.

However, the character of the large compression field described in the previous section coupled with the short time duration of most ballistic events (tens of microseconds) would seem to vitiate this argument on the role of void formation being a dominant mechanism, at least in ballistic scenarios. Clearly, inclusions may debond or crack under the large imposed shear fields, but the consequence of this would be minimal under the very large, nearly hydrostatic compression fields associated with the process zone. Furthermore, the data obtained in Reference 3 on the dependence of the value of instability strain with pressure also minimizes the possibility of void opening as a mechanism in ballistic events.

We conclude, then, that to describe the initiation of the instability known as adiabatic shear we need to consider the relative roles of work hardening and thermal softening. One could also consider strain-rate hardening effects but a sizeable body of data argues that strain-rate hardening effects are slight compared to strain hardening and thermal softening effects. In Reference 4 we showed that a suitable constitutive formulation which captures the essential features under consideration is given by:

$$Y = Y_o(1 + \alpha\gamma)^n \exp[- \beta T/(T_o - T)] \tag{3}$$

where Y is the flow stress, Y_o is an initial yield stress, γ is the effective plastic strain, α and n are strain hardening parameters, β and T_o are thermal softening parameters, and T, the rise in temperature from some ambient state, is given by

$$T = \{ \int^{\varepsilon} s_{ij} \, d\varepsilon^{P}_{ij} \} / (pc_v) \tag{4}$$

where p is material density, c_v is specific heat, s_{ij} are stress deviators, and ε^{P}_{ij} are plastic strain components.

The flow stress described by Equation 3 is illustrated in Figure 4 for a relatively high strength material (upper curves) and for a relatively low strength material (lower curves). The relative amounts of work hardening (Figure 4a) and thermal softening (Figure 4b) are shown separately. The net combined effects are shown in Figure 4c. We note the presence of a maximum (corresponding to an instability point) for both materials, however, the subsequent decline is precipitous for the high strength material, and more gradual for the lower strength material. When implemented in a finite difference hydrocode such as HEMP or DYNA at each cycle of the explicit numerical integration scheme, one computes the plastic strain and work done at each mesh point and then calculates the corresponding expansion or contraction of the yield circle.

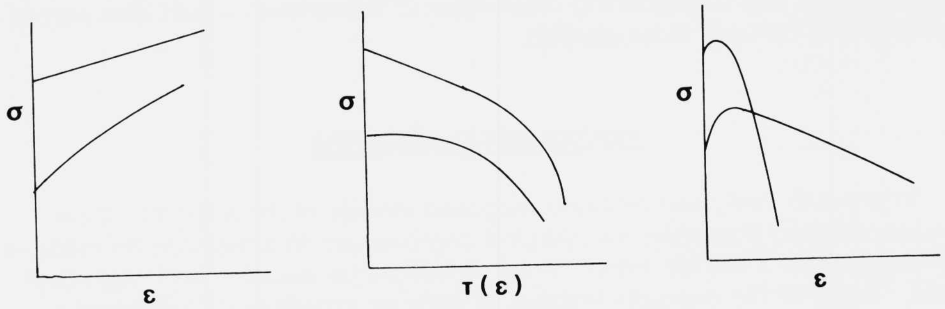

(a) (b) (c)

FIGURE 4. Generic illustration of the dependence of (a) flow stress on strain, (b) on temperature, and (c) on their combined effect. Upper curves refer to high strength steels and lower curves refer to low strength steels.

In selecting values for the material parameters associated with thermal softening, the following comments are considered pertinent. Available (static) elevated temperature tests measuring a wide variety of mechanical strength parameters suggest several trends. First, most of the available strength (90%) appears to be depleted by a temperature roughly one-half of the melting temperature. It is unwise, therefore, to choose melting temperature as T_o. Another observation is that the dependence of flow stress on temperature is not well approximated by a linear behavior from ambient to melt as is occasionally done (5). For a given alloy, materials which have been processed to a higher strength level exhibit a less stable microstructure and a much more rapid early decline with increasing temperature (Figure 4b, upper); those of intermediate and lower strengths have a more moderate early decline (Figure 4b, lower).

After significant temperature increases, there are precipitous drops in strength with the result that these initially separated curves later collapse toward the same low strength value at a common value of temperature, T_o.

The question of the influence of time-at-temperature is both important and yet very difficult to assess for the short time involved in high strain-rate applications. We take the point of view here that long-term temperature data serve as useful guides for initial selection of parameters for the model. Improved values can be determined in an interactive process involving comparisons of experimental results with predictions of computer simulations.

No attempt was made to account for thermal flow effects since, for the applications we have in mind, times are too short to permit any significant heat transfer. The issue of strain-rate hardening effects was also not considered since we wished to isolate the thermal effects for now. It is to be emphasized that although strengthening effects due to elevated strain rates are known to be relatively low for rates up to say 100/sec, it is also true that when localized deformation bands develop, strain rate within such bands becomes very high while dropping essentially to zero outside the band. Whether, and by how much, an accounting for this strengthening mechanism in this context would alter perception of events remains to be clarified.

EXPERIMENTAL METHODS

In order to verify and calibrate proposed models of the adiabatic shear band process so that basic metallurgical improvement in armor can be made, it is important that a flexible experimental procedure be available and well understood. Some of the desirable features of such an experimental procedure for the generation and growth of shear bands are that high strain rates be involved, that there be a prevailing hydrostatic pressure field, and that the experiment be amenable to analysis or numerical solution. Some of the existing experimental procedures in vogue are:

- Exploding but constrained cylinders (SRI).
- Torsional Hopkinson bar (Brown University and others).
- Double shear (Charpy) (Cowie/Olson, MTL).
- Stepped projectile impact (Rogers).

Major drawbacks to the exploding cylinder approach are that it is difficult to perform and analyze (thus inhibiting parameter studies), that it is strictly a postmortem examination and, therefore, offers little in the way of studying the nucleation process. The torsional Hopkinson bar experiment also involves postmortem examination, although Duffy has recently generated very interesting photographic observations of the dynamic process; it does not permit generation of shear bands in the presence of large hydrostatic pressure fields. The double shear experiments of Cowie and Olson do not involve high strain rates and are very limited in the level of prevailing hydrostatic pressure imposed.

On the other hand, a very interesting experimental procedure for the study of shear band nucleation and growth is the stepped projectile test in which one impacts a projectile into a small plate of the specimen material to be studied. The projectile is cylindrical in shape and has a blunt cylindrical tip which is embedded into the specimen. Behind the tip and connected to it is a relatively massive cylinder whose shoulders stop further indentation of the projectile tip when they impact the specimen. Rogers (6) has demonstrated the flexibility and utility of this approach. He has shown it is possible to exercise control over the initiation and development of localized bands in a wide class of materials using this procedure. For example, in an annealed 1018 steel impacted at 100 m/sec, the deformation near the corners of the impact crater left by the projectile tip was quite diffuse and showed little tendency to localize. When the same material was cold rolled 67% and impacted at 94 m/sec, a very localized deformation band was found emanating from the corner of the crater. When the latter material was impacted at 100 m/sec, a transformation shear band was found.

We note that this result is consistent with the ballistic observations of Mescall and Papirno (1) who found that when annealed 4340 steel plates were impacted by small, blunt steel cylinders (not stepped projectiles), the penetration process did not involve shear banding in the target. For much higher strength 4340 plates, however, the penetration process was controlled entirely by transformed shear bands (see Figure 1).

There are major differences between the experimental conditions of References 1 and 6 which are of considerable interest. First, although the target thicknesses were nearly the same (0.635 cm), the velocities involved differed by an order of magnitude: 100 m/sec versus 800 m/sec. Next, projectile masses also differed by more than an order of magnitude: 110 grams versus 2 grams. While the kinetic energies of both types of projectiles were, thus, nearly equal, we believe this is not relevant since, as we shall show later, very little of the stepped projectile energy is deposited near the shear bands which develop. Instead, it is transmitted to the support structure.

EXPERIMENTAL RESULTS

The actual experimental arrangement employed to implement the concept of a stepped projectile indentation of steel targets is shown in Figure 5. This "pill and washer" detail is impacted by a blunt cylinder whose diameter is several times that of the pill. Computer simulations of the test setup have been made to demonstrate that this arrangement is fully equivalent to an integral projectile and tip. Naturally, the test setup shown is much more convenient.

A series of experiments were conducted to explore the process of nucleation and growth of adiabatic shear bands in three steels with differing microstructures. Targets were impacted, sectioned, and examined for the presence of shear bands and their length. Figure 6 shows a plot of the length of a shear band developed in a Pearlitic 4140 steel alloy as a function of the depth of penetration (height of pill). Target thickness was 6.35 mm. The four curves of Figure 6 correspond to four values of the backup hole diameter (BHD), as shown in Figure 5. Figures 7 and 8 are corresponding results for 4140 quenched and tempered at 600°C and at 400°C, respectively.

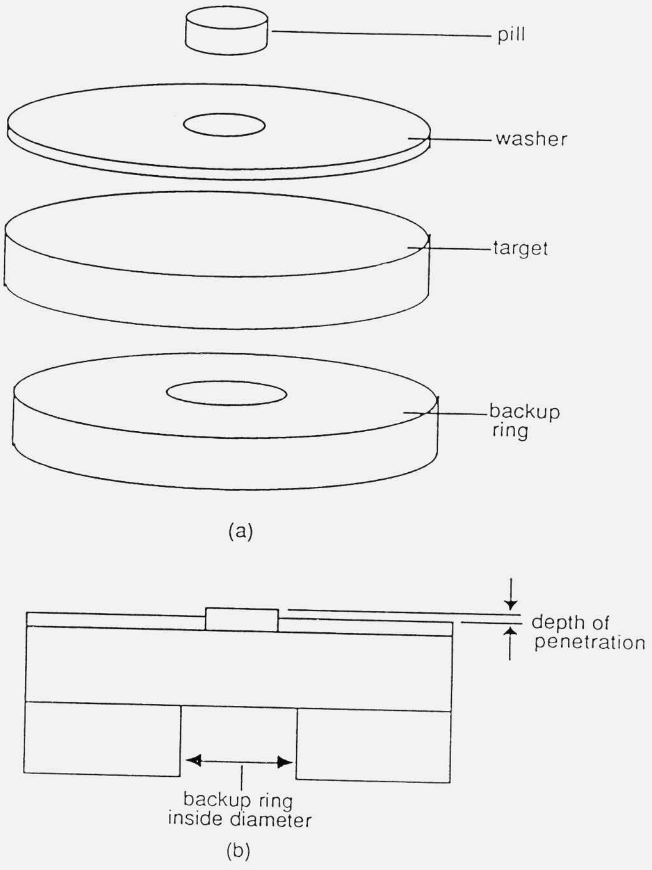

FIGURE 5. Schematic of details of stepped projectile experiment.

These results clearly indicate a dependence on microstructure. Bands tend to nucleate at much lower values of depth of penetration (smaller initial strain) for the material quenched and tempered at 400°C. Furthermore, the growth of bands in this material is much more rapid, since they traverse target thickness at an indentation level corresponding to that at which bands are just beginning to develop in the other two microstructures. In all cases studied, the rate of growth appeared to be exponential once the band had traversed approximately one-half of the target. Figure 8 shows that the higher strength microstructure

(QT at 400°C) was particularly unstable. This is to be expected, however, Figure 8 provides quantitative evidence. Alternatively, the lower strength steels would be expected to resist localization longer because of higher strain hardening rates, smaller flow stress, and smaller temperature rise for a given imposed strain level.

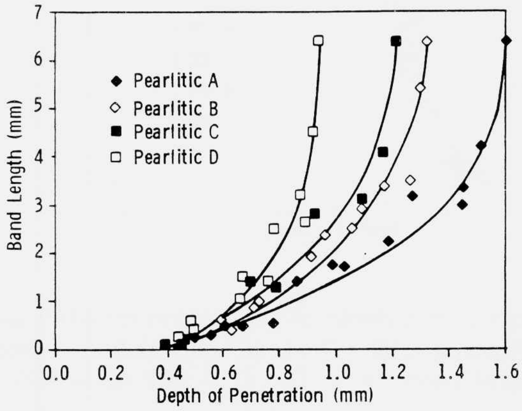

FIGURE 6. Band length versus depth of penetration for Pearlitic 4140 alloy steel. The letter designation of each plot refers to the backup hole diameter used: A = 1/2", B = 3/8", C = 5/16", and D = 1/4".

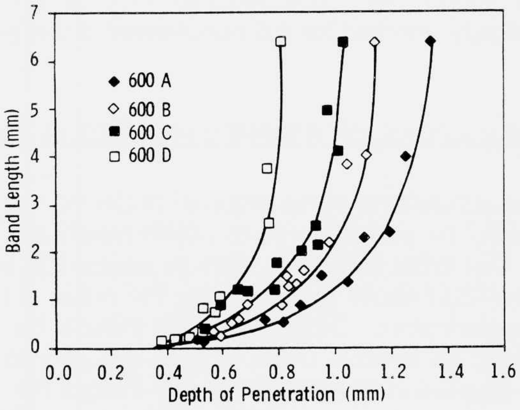

FIGURE 7. Band length versus depth of penetration for 4140 alloy steel quenched and tempered at 600°C. The letter designation of each plot refers to the backup hole diameter used: A = 1/2", B = 3/8", C = 5/16", and D = 1/4".

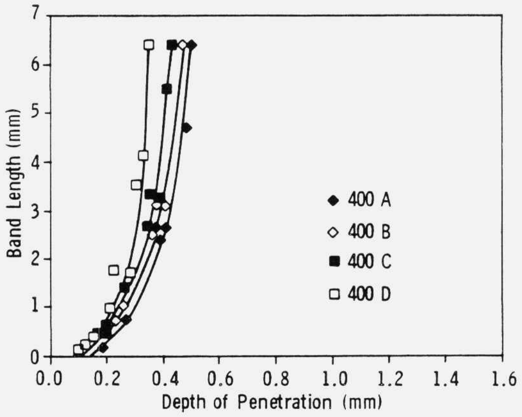

FIGURE 8. Band length versus depth of penetration for 4140 alloy steel quenched and tempered at 400°C. The letter designation of each plot refers to the backup hold diameter used: A = 1/2", B = 3/8", C = 5/16", and D = 1/4".

Figure 9 (a, b, c, and d) provides a cross plot of the data in which band length is plotted versus depth of penetration for a fixed backup hole diameter. It can be seen that there is a greater dependence on geometry details for the lower strength microstructures than for those quenched and tempered at 400°C.

Finally, Figure 10 shows that bands begin to nucleate within a very narrow variation of impact velocity required for full penetration of the pill.

COMPUTER SIMULATIONS OF STEPPED PROJECTILE EXPERIMENTS

Clearly, computer simulations of the stepped projectile test would serve to make it even more useful by permitting us to obtain results not directly observable in experiments. Our initial objectives were to assess the suitability of the constitutive model described above for predicting the onset of localized deformation in such experiments. Other objectives include the extraction of material parameters from an iterative series of tests and simulations. Some general results (before a discussion of detailed results) include the observation that the rear surface of the target should be rigidly supported outside a small circular region whose center coincides with the axis of the projectile; otherwise, the response of the target to impact involves a large amount of structural bending which influences the deformation interaction between target and tip in an undesirable manner. Another observation, which simplifies the simulation details, is that it is permissible to model only the tip and not the projectile with the stipulation that the velocity of the tip rear surface is held at a constant value until its plane reaches the face of the target. The shoulder portion of the projectile is thus considered to behave as an energy reservoir to maintain the imposed velocity on the tip rear surface. Simulations involving a full description of tip and shoulder indicate that no significant error is introduced by this simplification in the region of interest — vis-à-vis the target-tip interface. Questions might also arise concerning possible modifications of the stress field near the site of potential bands after the shoulder makes contact with the target face. It appears that details of target rear surface support and the low velocities involved (100 to 200 m/sec) combine to render such modifications negligible. The energy stored in the projectile body is primarily absorbed by the support system after the tip is embedded and after the bands are formed if, indeed, they do develop.

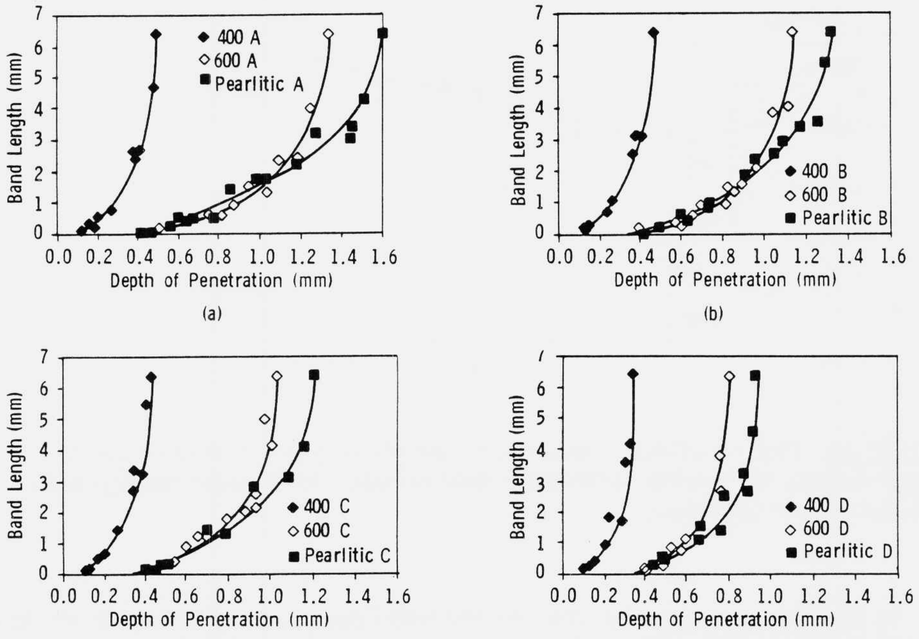

(a) (b) (c) (d)

FIGURE 9. Shear band length versus depth of penetration curves for all three structures of 4140 alloy steel tested for: (a) backup hole diameter "A" (1/2"), (b) backup hole diameter "B" (3/8"), (c) backup hole diameter "C" (5/16"), and (d) backup hole diameter "D" (1/4").

Figure 11 presents results for the indentation of a high strength steel target impacted by a stepped projectile (as discussed) at a velocity of 61 m/sec (200 ft/sec). Material properties employed in this example were Y_o = 20 kbar, n = 0.06, α = 12, β = 1.0, and T_o = 660°C (see Equation 1). Backup hole diameter was one-half inch, or twice the projectile diameter. Figure 11a shows the deformation at 15 microseconds after impact. The indentation process has been established; there is slight bulging on the target rear surface but little evidence of strain localization. There is, of course, a highly nonhomogeneous strain field with levels of 100% being obtained near the corners of the rapidly developing crater. Figure 11b presents macroscopic contours of effective plastic strain; contours of 50% and 25% cover an extensive area, however, values of 75% to 100% remain confined to the immediate area of the penetrator corners. Local temperature rises associated with the material properties employed in this specific illustration are only on the order of 400°C, so the thermal softening effect is just beginning to be felt. A very short distance away from the corner zones, strain and temperature levels are quite modest, dropping rapidly to only a few percent or degrees centigrade.

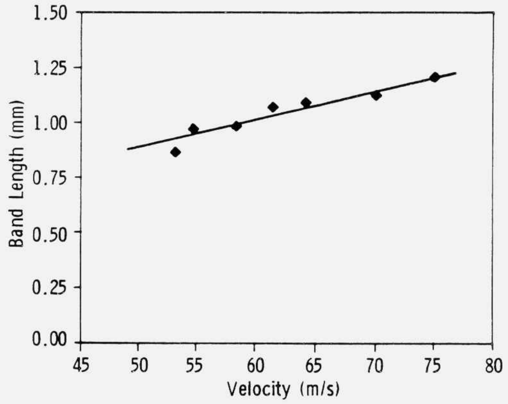

FIGURE 10. Plot of adiabatic shear band length as a function of projectile impact velocity for Pearlitic 4140 alloy steel targets. A constant backup hole diameter of 1/4" was used.

As an aside, we note that the velocity fields developed by this time are ideally suited to develop shear bands in this geometry. The projectile tip maintains an essentially constant velocity. The plug (i.e., the cylindrical region of the target immediately in front of the tip) has been accelerated in a nearly uniform manner to the tip velocity by this time, whereas points outside the plug region are essentially not moving due to the constraints mentioned above. We also note that it is in this context that one finds the greatest differences between the stepped projectile test and the conventional ballistic test. In the latter, one typically fires a smaller projectile at a higher velocity into comparable targets. During the penetration process, the projectile is slowed down considerably and, consequently, details of plug acceleration are quite different. Furthermore, ballistic targets are not supported near the projectile; consequently, the target deformation can be considerably more diffuse.

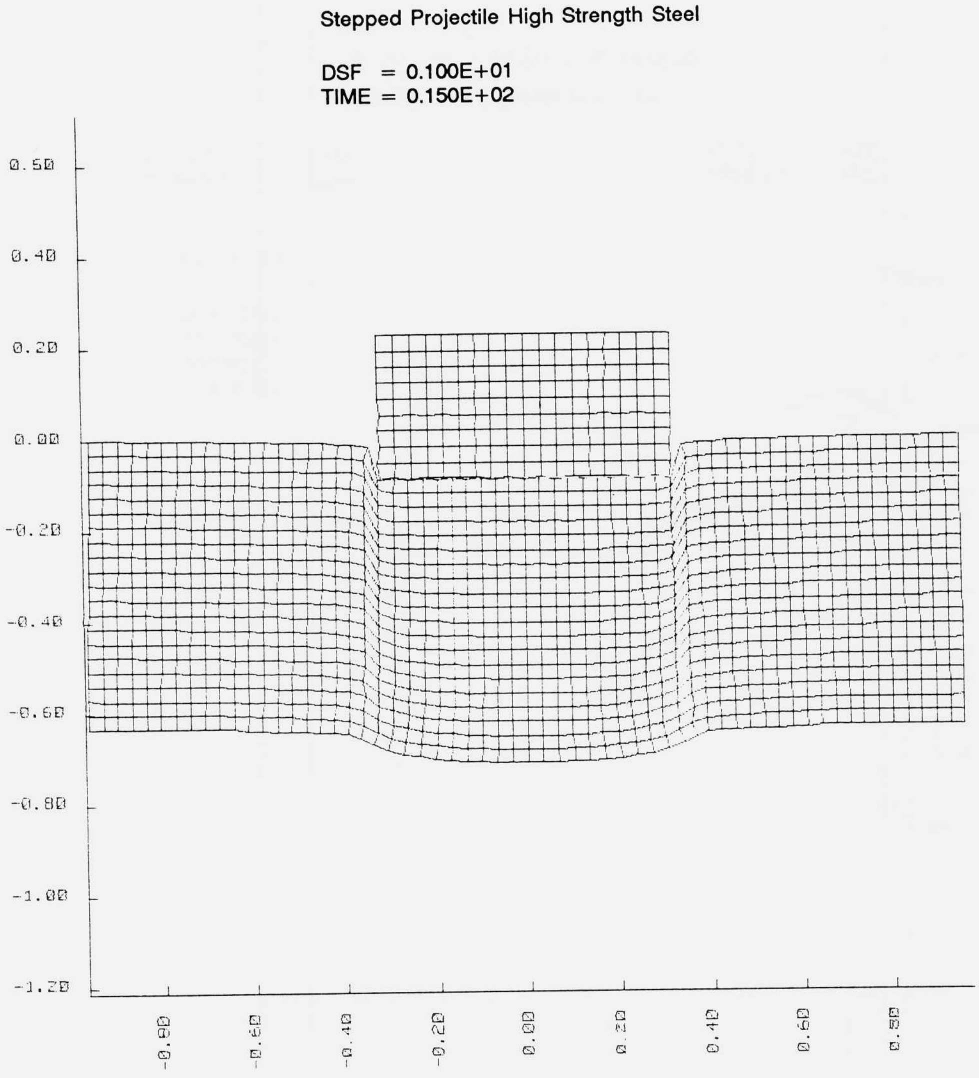

FIGURE 11a. DYNA simulation of stepped projectile indentation of high strength steel target at 15 microseconds after impact at 200 ft/sec. Backup hole diameter is 1/2" and projectile diameter and target thickness is 1/4".

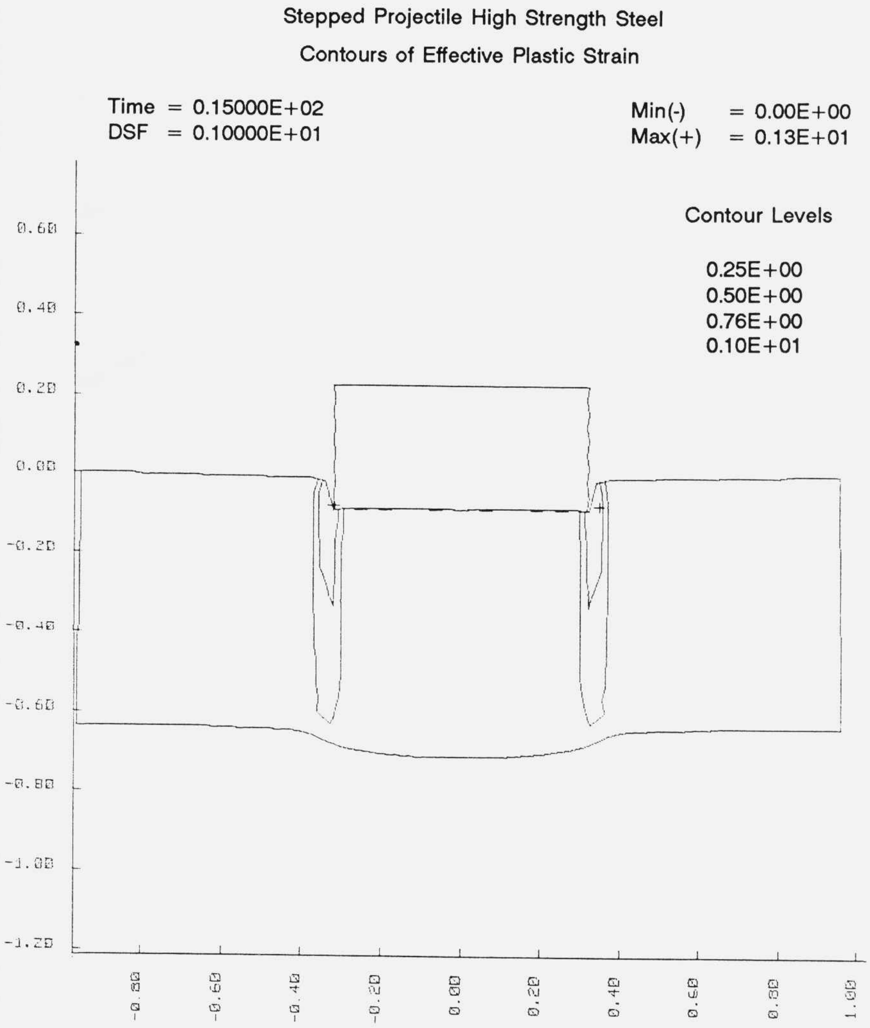

FIGURE 11b. Effective plastic strain contours (25% and 50%) at 15 microseconds after impact.

Figure 11c shows that by 20 microseconds (an indentation of 0.12 cm), localized deformation bands have begun to develop and, in fact, have sufficiently matured so that they reach the rear surface.

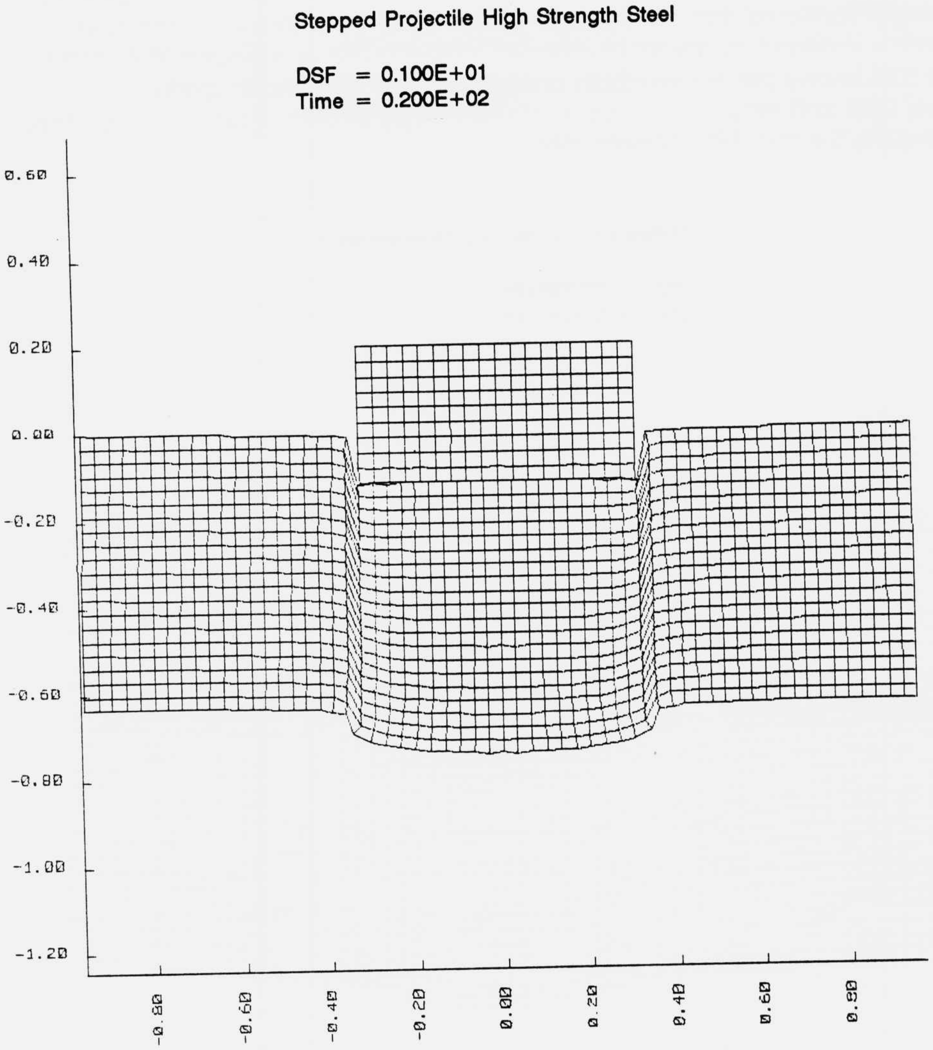

FIGURE 11c. Indentation of high strength steel projectile at 20 microseconds after impact.

Figure 12 presents results for the impact of a low strength steel target at the same velocity and support conditions as the high strength target of Figure 11. Specific target parameters chosen were Y_o = 0.005 Mbar, n = 0:12, α = 400, β = 1.0, and T_o = 660, thus, the strain hardening rate was increased considerably while the thermal softening rate was the same as in the high strength steel. (In practice, one would expect the initial thermal softening rate to be less than in this numerical example.) Figure 12a shows that the deformation pattern developed in the target is much more diffuse for the softer steel and, at this amount of indentation (0.21 cm), shows little, if any, tendency toward localization. Indeed, the zones immediately in front of the projectile tip have strain hardened and are still above their initial yield stress, having been only mildly softened by the strain-induced temperatures of approximately 150°C. Figure 12b shows the macroscopic contours of effective plastic strain – vis-à-vis 25% and 50%. These cover a significantly smaller volume then do their counterparts for the high strength steel.

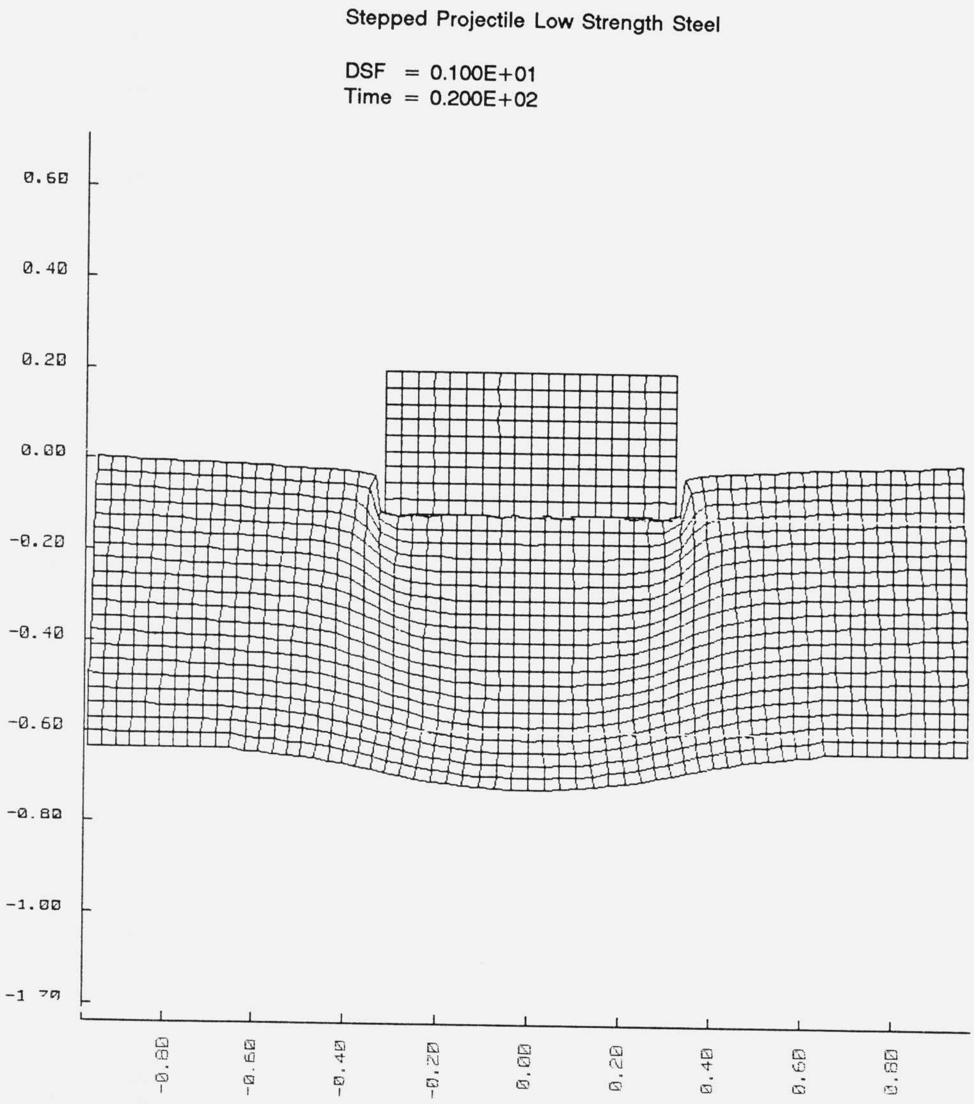

FIGURE 12a. DYNA simulation of stepped projectile indentation of a soft steel target at 20 microseconds after impact at 200 ft/sec.

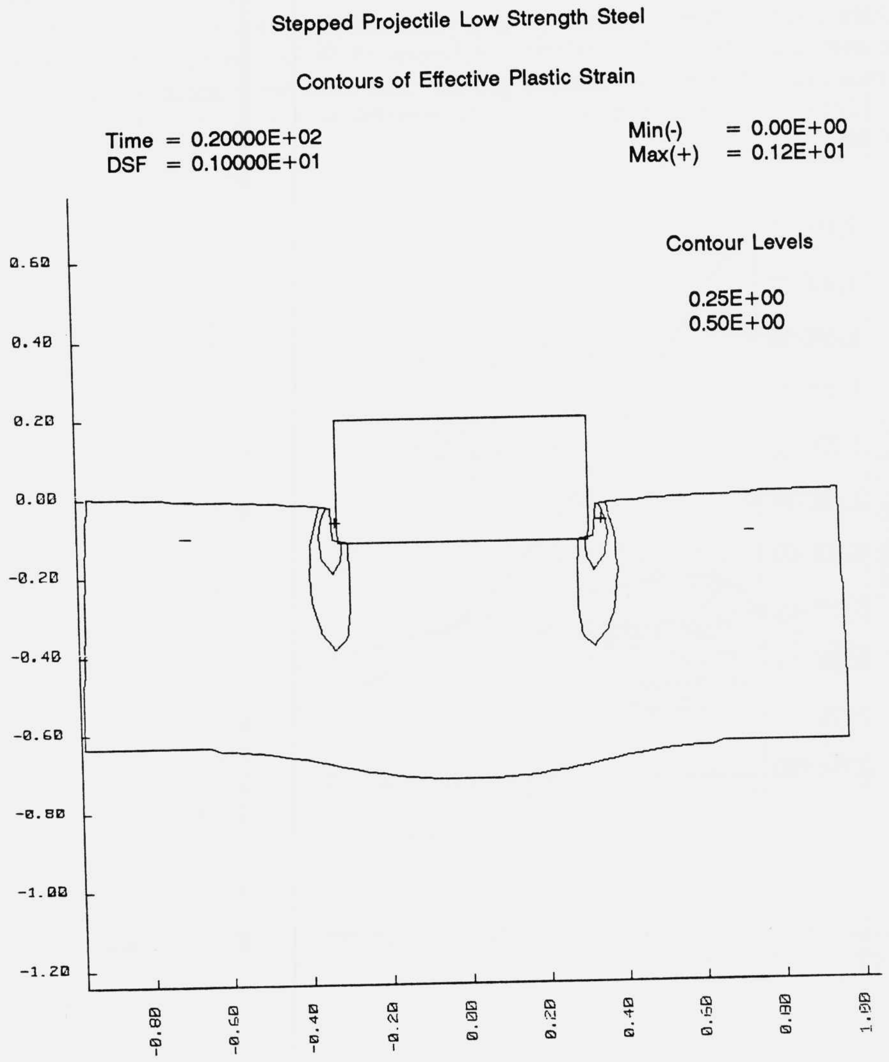

FIGURE 12b. Contours of effective plastic strain at 20 microseconds after impact of low strength steel target.

Figure 13 presents the stress-strain paths actually followed by each material point for hard and soft steels according to the model of Equation 1.

The concept of an instability strain (i.e., a maximum in the stress-strain curve) is one which is frequently invoked to characterize a material's sensitivity to shear band formation. Smaller instability strain implies greater sensitivity.

The value of the instability strain has little to do, however, with the onset and propagation of shear bands. We find, for example, from our simulations of stepped projectile experiments for high strength steels (Figure 11) that the band which does develop does not mature until the local strain level is much higher than the instability strain. Examination of Figure 11 (a, b, and c) shows that at 15 microseconds after impact, strains greater than 50% have occurred prior to the full development of a mature band, whereas the instability strain is on the order of 5%.

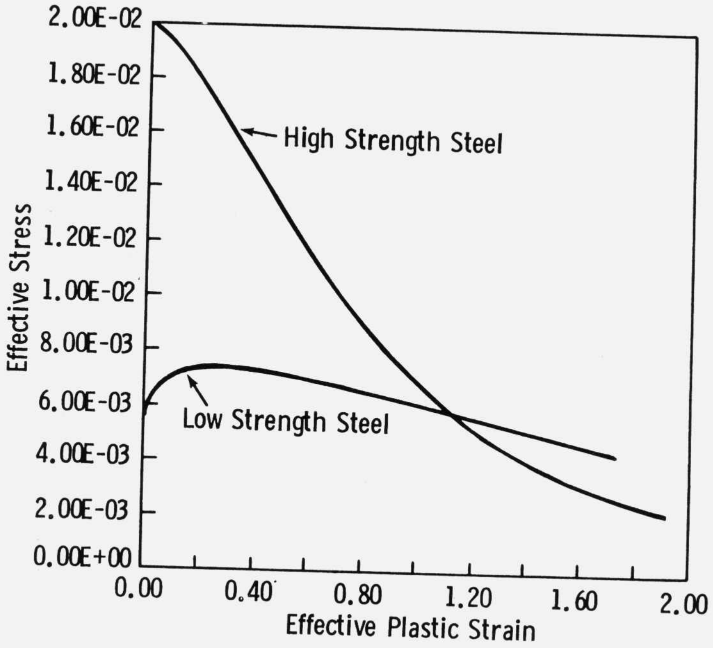

FIGURE 13. Plot of effective stress in Mbar versus effective strain trajectories followed by high and low strength steel targets of Figures 11 and 12.

SUMMARY AND DISCUSSION

After discussing the significance of adiabatic shear bands in penetration mechanics, we described the important details of shock waves in ballistic scenarios. We proposed a constitutive relation for work hardening versus thermal softening in the initiation of localized deformations. It appears to us that a proposed role of void nucleation in the formation of shear bands under ballistic conditions is not a tenable one because of the presence of prevailing states of high hydrostatic compressions. Among several candidate techniques for experimental determination of a material's susceptibility to the formation of adiabatic shear bands, we prefer that of the indentation of a stepped projectile because of its inherently greater control and because of the closer proximity of stress states to the ballistic ones. Computer simulations of the latter experiment add considerable supplementary information and can be used in an iterative fashion to extract relevant information on suitable stress-strain behavior, as well as numerical values pertinent to the nucleation event.

REFERENCES

1. J. Mescall and R. Papirno. Spallation in Cylinder-Plate Impact. Experimental Mechanics, v. 9, 1974, pp. 283-311.

2. C. Zener and J. Holloman. Journal of Applied Physics, 15:22, 1944.

3. J. G. Cowie, M. Azrin, and G. B. Olson. Microvoid Formation During Shear Deformation of Ultrahigh Strength Steels. Proceedings of the Thirty-Fourth Sagamore Army Materials Research Conference, 1987 (in press).

4. J. Mescall. On the Relative Roles of Strain-Hardening and Thermal-Softening in Adiabatic Shear Bands. Metallurgical Applications of Shock-Wave and High Strain-Rate Phenomena, Murr, Staudhammer, and Myers, ed., Marcel Dekker, Inc., 1986.

5. G. Johnson and W. Cook. Fracture Characteristics of Three Metals Subjected to Various Strains, Strain-Rates, Temperatures and Pressures. Journal of Engineering Fracture Mechanics, v. 21, no. 1, 1985, pp. 31-48.

6. H. Rogers. Adiabatic Shearing – General Nature and Material Aspects. Material Behavior Under High Stress and Ultra-High Loading Rates, J. Mescall and V. Weiss, ed., New York: Pelham Press, 1983, pp. 101-118.

APPENDIX

As an example of how computer simulations can be used to provide insight into both kinematic and material property issues associated with penetration mechanics, consider the problem of a long-rod penetrator made of high density material impacting a thick steel target at a velocity of 4,000 ft/sec (2 cm/μsec). Under these conditions, experiments show that penetration of the target takes place primarily by an erosion mechanism in which a deep crater is formed whose diameter is roughly twice the projectile diameter, and within which both projectile and target material flow back toward the impact face. Experimental observations referred to may be either static postmortem examinations of targets or dynamic shadow graphs which provide information on such things as the velocity of a projectile while external to the target, or data on behind-the-armor debris. What is not observable, generally, of course, is detail concerning the interaction of projectile and target at their moving interface within the target. Thus, the specific advantage provided by computer simulations is that they provide quantitative information on internal states of stress and strain which are not obtainable from other sources. Although the simulation we shall discuss concerns a specific ballistic event and mechanism (erosion), nevertheless, many of the characteristics to be detailed below are common to other impact conditions.

Details of the progression of deformation in both target and penetrator are shown (Figures A-1 through A-4) for times 2, 10, 18, and 22 microseconds after impact. Neither the rear of the target (3 cm thick) nor the aft of the penetrator (5 cm long) is visible in these figures which focus on the impact area. From the simulation we find that the interface velocity drops quickly from its "initial" value of 0.12 cm/μsec to a value of 0.07 at 10 μsec and 0.06 at 22 μsec. At this time, points in the penetrator approximately one diameter to the left of the interface are moving with 98% of their initial velocity. Approximately 30% of the rod length has been consumed by the erosion process.

Details of the dynamic stress fields developed by these impact conditions are shown in Figure A-5. We plot values of constant hydrostatic pressure, neglecting deviatoric stress components, simply for convenience.

The stress history within both target and projectile can be divided into three phases. There is an initial shock-propagation phase whose local stress levels are extremely high near the impact zone. These are well approximated by Equation 1 of the text. This first phase does not propagate in space and is extremely short in duration (in the present example, about 2 microseconds). The immediate availability of free surfaces on the target impact face and on the outside diameter of the penetrator induces rare faction waves for attenuation of the initial impact stress fields. These relief waves may be clearly traced in the pressure contours of Figure A-5.

Following the first phase, there is a relatively long second phase depending on the projectile length and target thickness. Stresses in this quasi steady-state phase are well approximated by Equation 2. In the present example, stress amplitudes are 40 to 50 kbars. There is, finally, a third stage which is characterized by a lower amplitude stress level which is more oscillating in nature and which corresponds to the first stages of the structural vibration phase of target response.

Another feature of the dynamic stress field associated with penetration, which may be determined by study of these figures, is the existence of a highly localized spatial region, which we have chosen to call a "process zone." Nearly all the events of physical interest occur within the process zone. In the present example, this zone is about one projectile diameter in radius, is centered at the projectile-target interface, and moves with the interface. Once the quasi steady-state second stage of erosion is entered, only elastic waves move away from the process zone. One kinematic consequence of this is that significant deceleration of projectile and acceleration of target material occurs only within the process zone. Deceleration of projectile does **not** occur uniformly along the projectile by means of the propagation of plane waves down the cylinder axis. Recall that the velocity of projectile material points just outside the process zone at 22 μsec is about 98% of the initial velocity.

The question arises, naturally, about what experimental evidence is available to verify these predictions of the HEMP simulation. Sequential flash x-rays taken while a long rod penetrates a thick target show that the projectile tail still moves with very nearly its launch velocity even though nearly 50% of the projectile front end has been eroded away in the penetration process. Of course, the x-ray shadow graphs provide only the exposed projectile outline and, thus, we are unable to distinguish any velocity gradient along the projectile length. Nor are we able, in general, to "see" the projectile-target interface because it is within the cavity. However, the data on the velocity of the projectile rear surface velocity reveals a smooth behavior rather than one with discrete decrements which would correspond to periodic arrivals of large amplitude planar waves, if indeed such waves traversed the penetrator axis. We, thus, consider this evidence as tending to confirm the HEMP analysis.

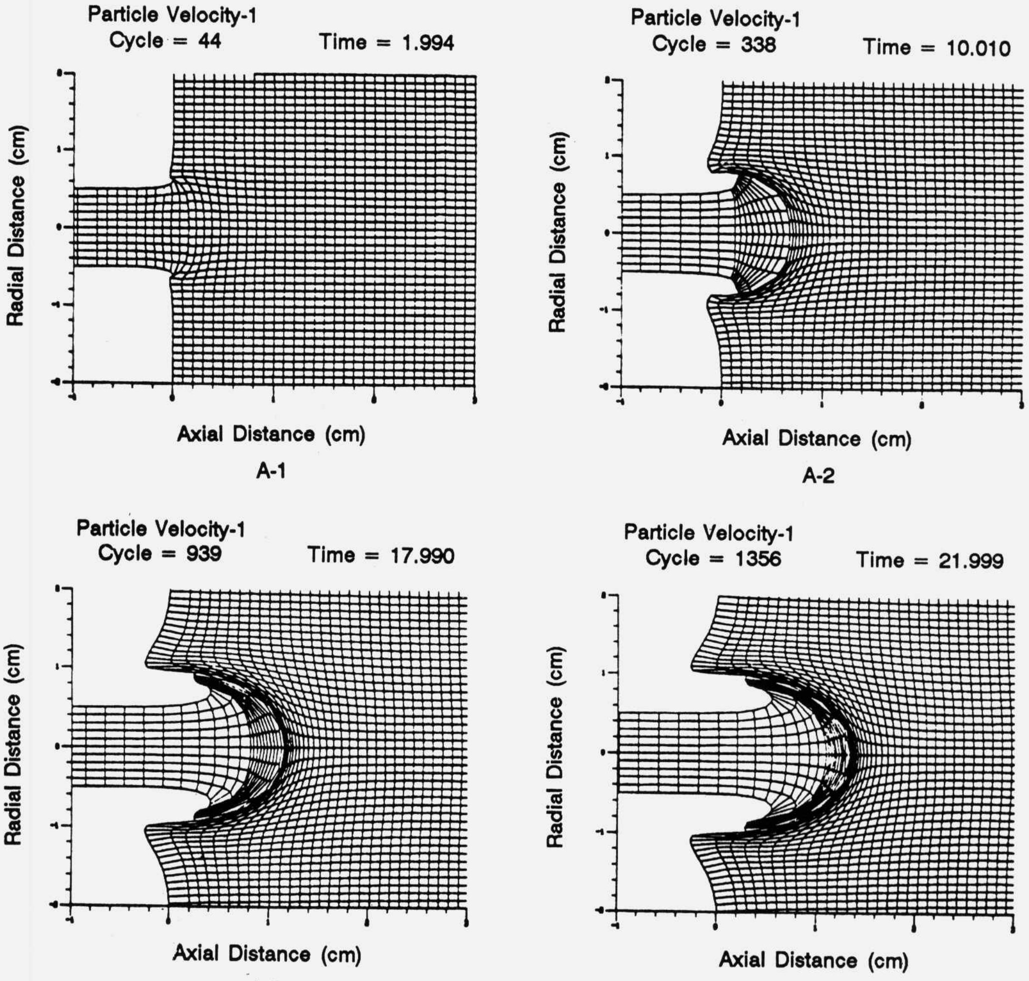

A-1

A-2

A-3

A-4

<u>FIGURES A-1 THROUGH A-4</u>. Computer simulation of penetration of steel target by high density long rod. Impact velocity was 4,000 ft/sec. Figures A-1, A-2, A-3, and A-4 correspond to times 2, 10, 18, and 22 microseconds after impact.

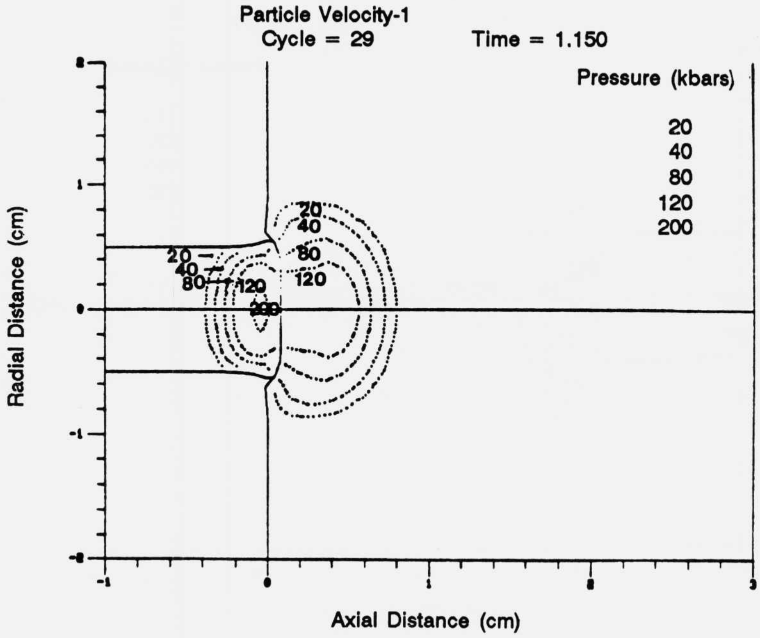

A-5a

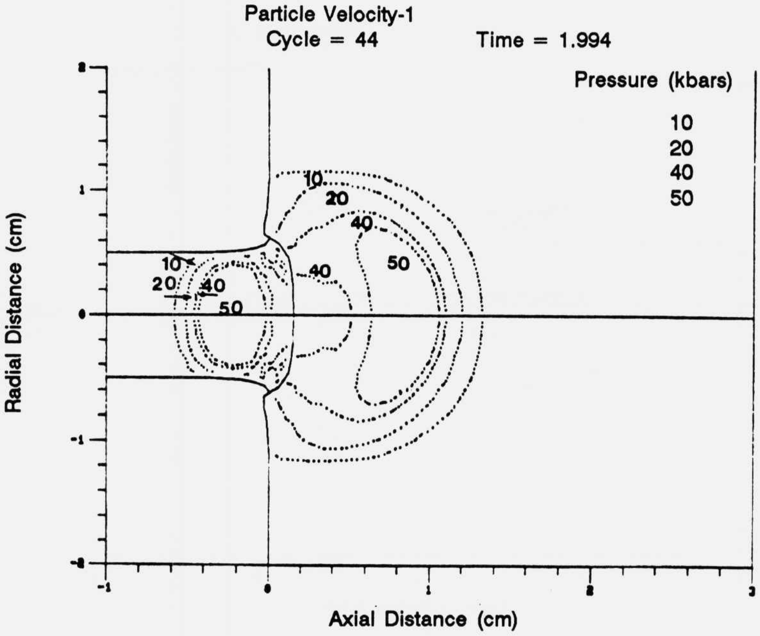

A-5b

FIGURES A-5a AND A-5b. Isobars of constant pressure (in kilobars) developed as a result of penetration of steel target by high density long rod at 4,000 ft/sec. Approximate times are 1 and 2 microseconds after impact for Figures A-5a and A-5b, respectively.

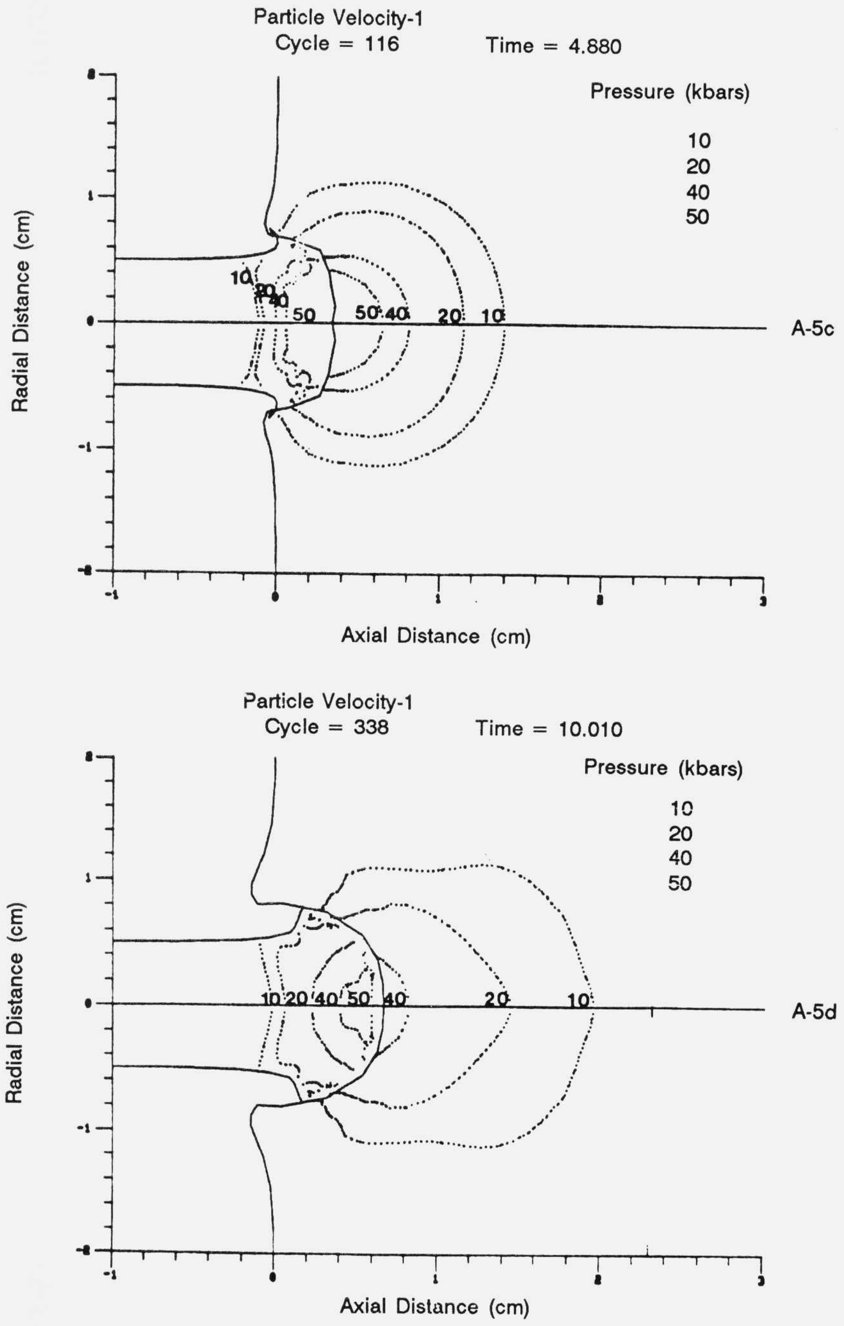

FIGURES A-5c AND A-5d. Isobars of constant pressure (in kilobars) developed as a result of penetration of steel target by high density long rod at 4,000 ft/sec. Approximate times are 5 and 10 microseconds after impact for Figures A-5c and A-5d, respectively.

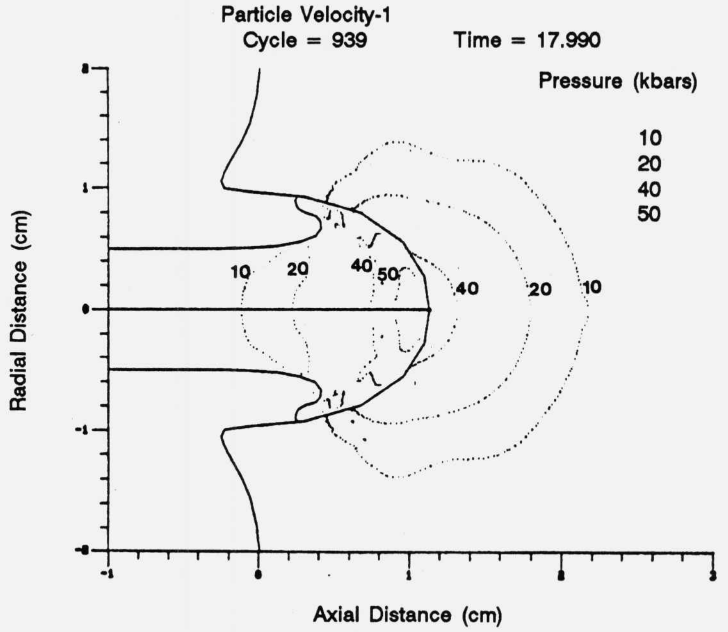

A-5e

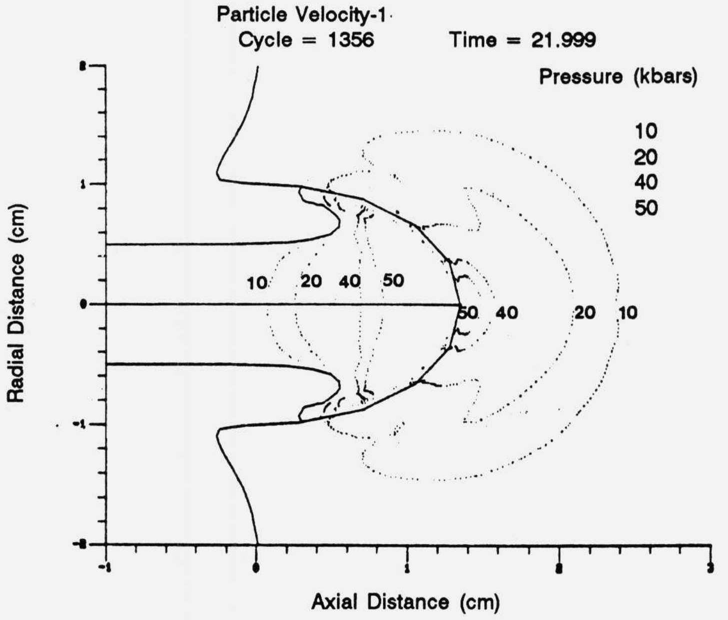

A-5f

<u>FIGURES A-5e AND A-5f</u>. Isobars of constant pressure (in kilobars) developed as a result of penetration of steel target by high density long rod at 4,000 ft/sec. Approximate times are 18 and 22 microseconds after impact for Figures A-5e and A-5f, respectively.

MODELING OF INTERACTIONS IN VOID NUCLEATION AND GROWTH

D. M. TRACEY and P. J. PERRONE
U. S. Army Laboratory Command
Materials Technology Laboratory
Watertown, Massachusetts 02172-0001.

ABSTRACT

Metallographic studies of alloy samples which have been strained plastically commonly show populations of voids which have nucleated at second phase particles. The continued nucleation, deformation, and coalescence of such voids during loading leads to cracking and macroscopic fracture, the details of which depend strongly upon the mode of loading. The mechanics of void softening in ductile metals under hydrostatic tensile stress have been emphasized in the literature. Here we have focused on shear loadings with the objective of developing an understanding of the role of voids in shear localization phenomena. Elastic-plastic finite element analyses of the three-dimensional fields near pairs of interacting voids and also near pairs of interacting particles have been performed and are discussed in the paper. The particle solutions represent data needed in the development of nucleation criteria, while the void pair solutions should assist in developing a quantitative understanding of the void sheet mechanism of damage evolution.

INTRODUCTION

There is a great deal of evidence that ductile fracture of metallic alloys stems from the nucleation of voids at second phase microstructural particles. Nucleation occurs when either critical conditions at the interface are achieved, or when the strength of the particle is reached, causing a fracture of the particle. Either event produces local crack damage which deforms into a void as the plastic deformation of the sample proceeds. Plasticity theory has been applied to the case of void deformation in the presence of triaxial tension, and results have demonstrated that the void surface can experience strain levels far in excess of nominal values when the mean stress is above yield stress levels, Rice and Tracey (1). Consequently, the voids grow and the material progressively weakens as neighboring voids coalesce by impingement in such stress environments.

Evidence shows that under low levels of mean stress, voids coalesce by a mechanism of cracking along void pair ligaments oriented in the maximum shear direction. Cox and Low (2) observed that in a 4340 steel sample processed to an UTS of 1516 MPa, two populations of particles contributed to the void damage leading to fracture: MnS inclusions of the 10 micron size range, and Fe_2C cementite particles of the 1 micron size range. They observed large voids which had nucleated at the inclusions linked by the "void sheet" mechanism, discussed earlier by Rogers (3) for the case of copper. The void sheet consisted of numerous cementite nucleated voids concentrated on void pair ligaments oriented in the maximum shear direction. In recent work, Cowie and Azrin (4) have detected the nucleation of voids at one-half micron sized grain refinement carbide particles in shear tests of RHC56 4340 steel.

In this report three-dimensional elastic-plastic results are given for the stress and strain fields that develop near void pairs, and also near particle pairs. The matrix material has been modeled as a non-hardening elastic-plastic metal, while the particles are considered to be elastic with a modulus twice that of steel. The results vividly demonstrate how nominally uniform shear conditions are perturbed near interacting inhomogeneities. Comparisons with plane strain solutions are made and these demonstrate the importance of including three-dimensional effects into micromechanical computer simulations.

The analyses modeled a sample of metal, nominally under uniform shear loading, containing one inhomogeneity pair (either a pair of voids or a pair of particles) buried within the sample far from its boundaries. Spheres placed at a distance of three diameters is the pair configuration we have limited our discussion to in this paper. Two separate orientations of the pair with respect to the direction of applied shear were considered, as illustrated in Figure 1. As shown in the top quarter section, one orientation has the applied shear directed parallel to the pair centerline. The bottom quarter section illustrates the other orientation which has the applied shear directed perpendicular to the centerline.

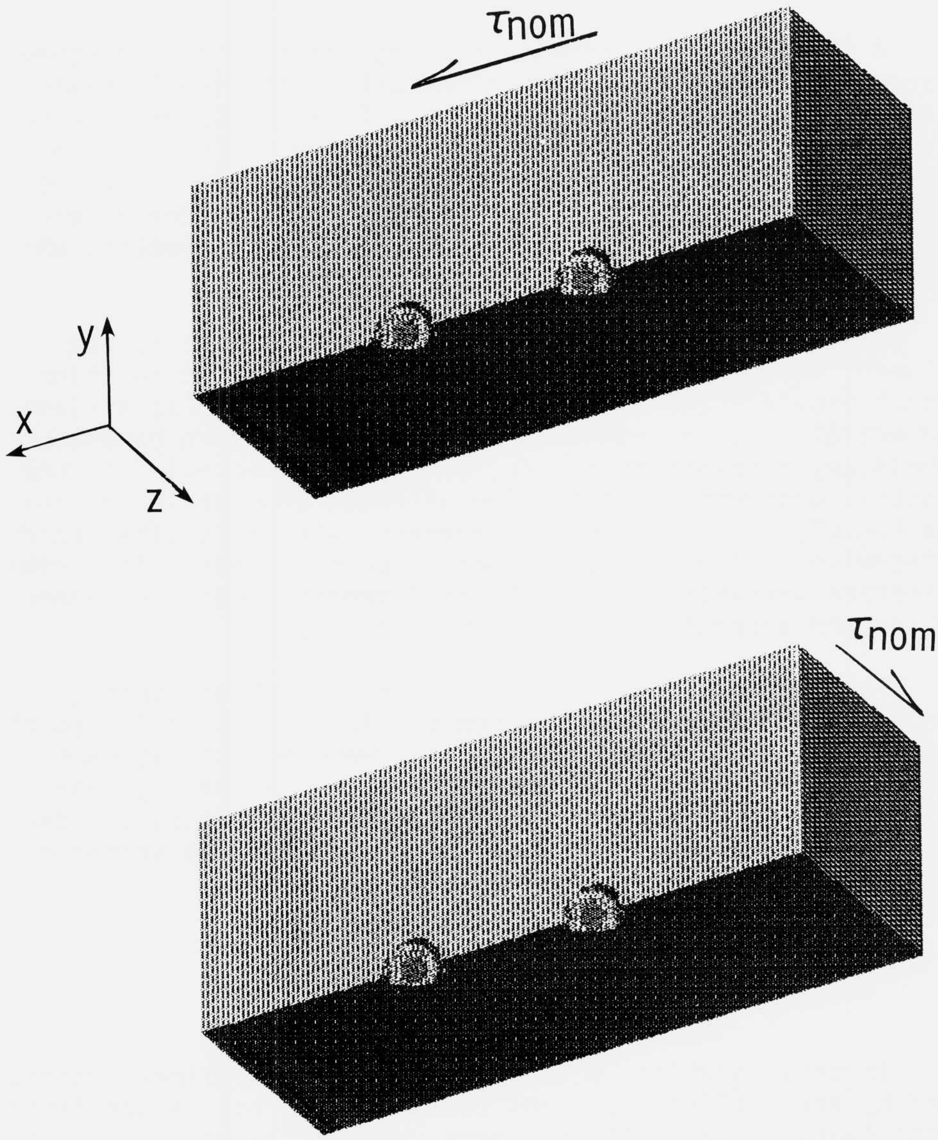

Figure 1. Quarter section of inner region containing void/particle pair under far field simple shear loading. In top drawing, shear load is directed parallel to pair centerline. Bottom drawing has shear load perpendicular to centerline.

NUMERICAL FORMULATION

A finite element formulation was employed in the study to ascertain fully plastic solutions within the small strain theory of non-hardening plasticity. These solutions can be used to approximate the conditions that would prevail near interacting voids and particles at the point of incipient flow localization on the macroscale. Not considered here are solutions representing conditions of large deformation which develop after localization has initiated.

Specifically, an incremental elastic-plastic finite element formulation was used. The fully plastic solution which provides the local flow field of interest is achieved numerically by incrementally tracing the loading parameters (boundary displacements here, as described below) from the initial unstressed state. The approach consists of approximating the undetermined displacement rate field with standard piecewise defined finite element interpolations. The primary discrete variables are nodal displacement rates (increments) which are determined at each step of loading.

To achieve the desired uniform remote strain state, boundary nodes were constrained to displace according to the specified state. These constraints were imposed at each increment and magnitudes were maintained in fixed proportions. If these specified displacement increments are denoted u_1 through u_m, the matrix equation for the vector of undetermined values $\underline{u}$ is given by

$$\underline{K}\ \underline{u} = -\ \underline{K}_1 u_1 - \ldots - \underline{K}_m\ u_m$$

In this equation, $\underline{K}$ is the constrained stiffness matrix and $\underline{K}_i$ are stiffness columns corresponding to the specified components. The stiffness terms vary according to the position of the elastic-plastic boundary and stress state (flow rule). An implicit scheme is used at each step to average the flow rule at each position within the plastic zone. The load history is discretized through an adaptive incrementation procedure discussed by Tracey and Freese (5,6). The planar and three-dimensional versions of this formulation are embodied in the MTL FORTRAN code EPFE which was utilized in this study.

A two-dimensional example which illustrates the approach is provided in Figure 2. The example involves a band with a centrally located pair of cylindrical voids. To display the pair, the local mesh has been omitted in the drawing. Plastic zone results for the three imposed conditions of uniaxial extension, simple shear, and combined strain are drawn below the band. The results can be contrasted with those of Nagpal et al. (7) who analyzed the problem of a periodic array of cylinders by applying the plane strain slipline theory. Their interest was in establishing the load transfer which corresponds to specified relative displacements across bands and using the results for prediction of crack extension by the banding mechanism.

The plastic zones have been illustrated in Figure 2 by drawing those elements which have met the yield condition. It is apparent that the character of the solution depends very strongly upon the nature of the loading. For instance, in extension yield first occurs on the void surfaces at the centerline which is the location of the maximum strain throughout. Whereas, in the case of simple shear, these locations never reach the yield condition. The extensional and combined loading results are for nominal strain levels near general yield. The simple shear results are for a nominal strain of 77% of the yield strain of the material. In this case, with further loading, the distinct plastic zones link by hinges allowing a local mechanism for gross plastic deformation.

Our primary attention in this work has been directed to the solutions for pair interaction in three dimensions. Details of the solutions will be presented below. The quarter sections displayed in Figure 1 contain a pair of quarter spheres which are centered on the x axis. In the top case the nominal shear stress corresponds to the yx stress component while corresponding to the yz component in the bottom case. If the coordinate axes are centered between the spheres, the planes x=y=z=0 then serve to define planes of reflective symmetry of the model. Geometrically, the total region can be viewed as an assembly of eight identical subregions, each containing a single quarter sphere. The regions displayed in Figure 1 are unions of two of these elemental subregions. Actually, only an interior subregion is displayed. The total region had dimensions 13x10x10 relative to the sphere diameter D. By noting conditions of skew anti-symmetry, it was possible to perform the analysis by discretizing a single subregion (octant) of the total model.

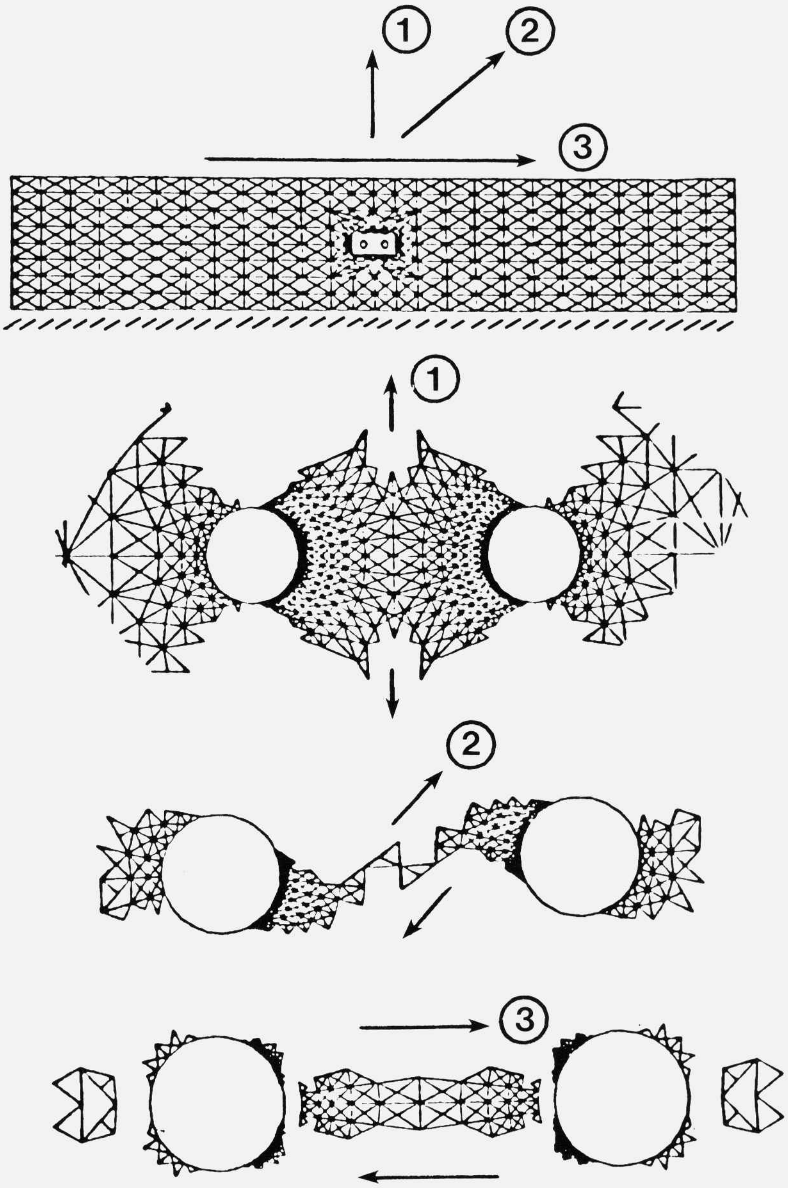

Figure 2. Two-dimensional plane strain results for plastic zones near pair of cylindrical voids for three nominal strain cases: uniaxial extension (top), simple shear (bottom), combined extension and shear (middle).

If the entire region were to be modeled, the simple shear state would be enforced in the top problem of Figure 1 in the following way. The two yz boundary faces would have the x displacement varying linearly with y, and on these faces the y component of displacement would be zero. The xz faces would have a constant value for the x displacement and a zero value of y displacement. The z component of traction would be zero on these four faces, corresponding to zero valued xz and yz shear stresses. Finally, the xy faces would be completely traction free.

When the skew anti-symmetry conditions are invoked on the planes of geometric symmetry, the following boundary conditions produce the state of nominal simple shear. In the top problem, on x=0 the y component of displacement as well as the x and z components of traction are zero. On y=0, the x component of displacement and the y and z traction components are zero. Finally, on z=0 the z displacement and x and y tractions are zero. Similar conditions can be applied to the faces of the elemental octant in the bottom problem where the applied shear is directed perpendicular to the centerline.

The finite element mesh used over the octant consisted of constant strain tetrahedra. The mesh was generated by first developing a field of eight-node brick elements which were individually subdivided into five tetrahedra. The mesh refinement was different in the analysis of the two void problems. The case of parallel shear had a mesh consisting of 4500 elements and 1200 nodes, each with three degrees of freedom. The perpendicular shear analysis was more refined in that there were 7100 elements and 1800 nodes in the mesh. The analysis of the pair of particles was conducted using the refined mesh for both load orientations. The additional complexity in the particle analysis involved discretization of the particles themselves. The quarter particle appearing in the octant was represented by 1300 elements to give a total mesh of 8400 elements and 2000 nodes.

PAIR INTERACTION IN 3D

The elastic solution for an isolated spherical void in simple shear has been described by Love (8). Referring to Figure 1, the maximum stress occurs at the two points on the void surface on the xz plane with tangent in the direction of applied shear. For a Poisson's ratio of 0.3, the stress

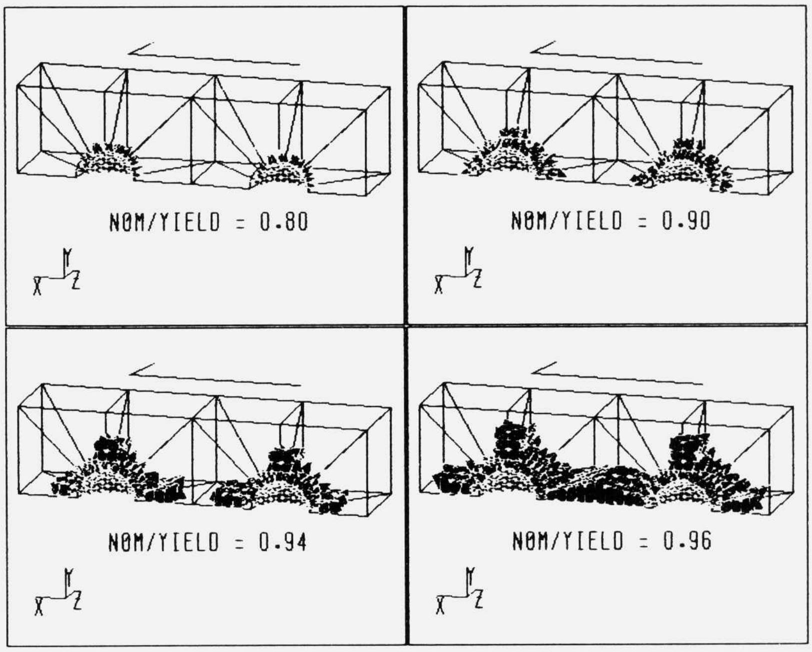

FIGURE 3. Plastic zone growth near spherical void pair before general yield conditions are achieved for shear parallel to centerline of voids.

concentration factor at these locations is 1.91, suggesting that void surface yielding should commence when the nominal shear level equals 1/1.91=0.52 times the material's yield strain in shear.

Four stages of the elastic-plastic solution are illustrated in Figure 3 for a pair of spherical voids spaced at a distance of three diameters under a remote shear directed parallel to the centerline. Plastic zones are represented in a quadrant by regions consisting of tetrahedron elements which have met the yield condition at the load level indicated. As anticipated from the classical elasticity solution, yielding first occurs in this quadrant at the void surfaces 90^{o} from the pair centerline in the xz plane. As load is increased, plasticity spreads from these locations. In the top left, corresponding to a remote strain of 80% of general yield, most of the void surfaces have yielded, but there is no yielding between voids. Significant yielding between the voids has occurred at 94% of yield, as demonstrated in the bottom left. This 3D solution differs in character from the plane strain solution, in that the plastic zones from the voids merge without development of an independent ligament plastic zone. As can be seen in the bottom right drawing, at 96% of general yield this merger is completed, leading the way for a mechanism of extensive plastic straining between voids.

The strain intensification that occurs along the centerline of the void pair is summarized in Figure 4. Data are plotted for the two spherical void pair problems and also for the cylindrical void pair problem. These problems are individually considered in the two top and the bottom left plots of Figure 4. The results of the three problems are contrasted in the bottom right plot which has peak local strain plotted against nominal strain level.

The component of strain that is plotted for each case corresponds to the nominal simple shear state, e.g. yz component for the top left problem. The data are presented relative to the material's yield strain in shear. The distributions along the centerline are plotted for x/D values from 0.5 to 2.5, which corresponds to the distance between void surfaces.

When the applied shear is directed perpendicular to the pair centerline (top left), the centerline strain maxima occur on the void surfaces. The results for incipient yield (nominal strain = 0.49 times yield strain) demonstrated the extremely localized effects of inhomogenities in elasticity. As can be seen, the strain is elevated over the nominal value only within a distance of one void radius from the void surfaces. The strain maxima equal approximately twice the nominal value in the elastic solution. At general yield, the maxima have increased to about three times the nominal value and interaction is evident with mid-centerline strain magnitudes significantly exceeding the nominal value.

The analysis of the spherical void pair with shear parallel to the centerline was conducted using a mesh that was too coarse to adequately capture the shear free condition which holds at x=0.5 D and 2.5 D. Nonetheless, the character of the elastic-plastic solution is thought to be reasonably represented in the top right plot. As in the other case, the elastic solution shows strain variations only within one radius of the void surfaces, with the nominal strain value realized over the middle half of the span between the voids. At general yield, the strain exceeds the nominal value over the entire ligament. The plot shows a modest peak at roughly

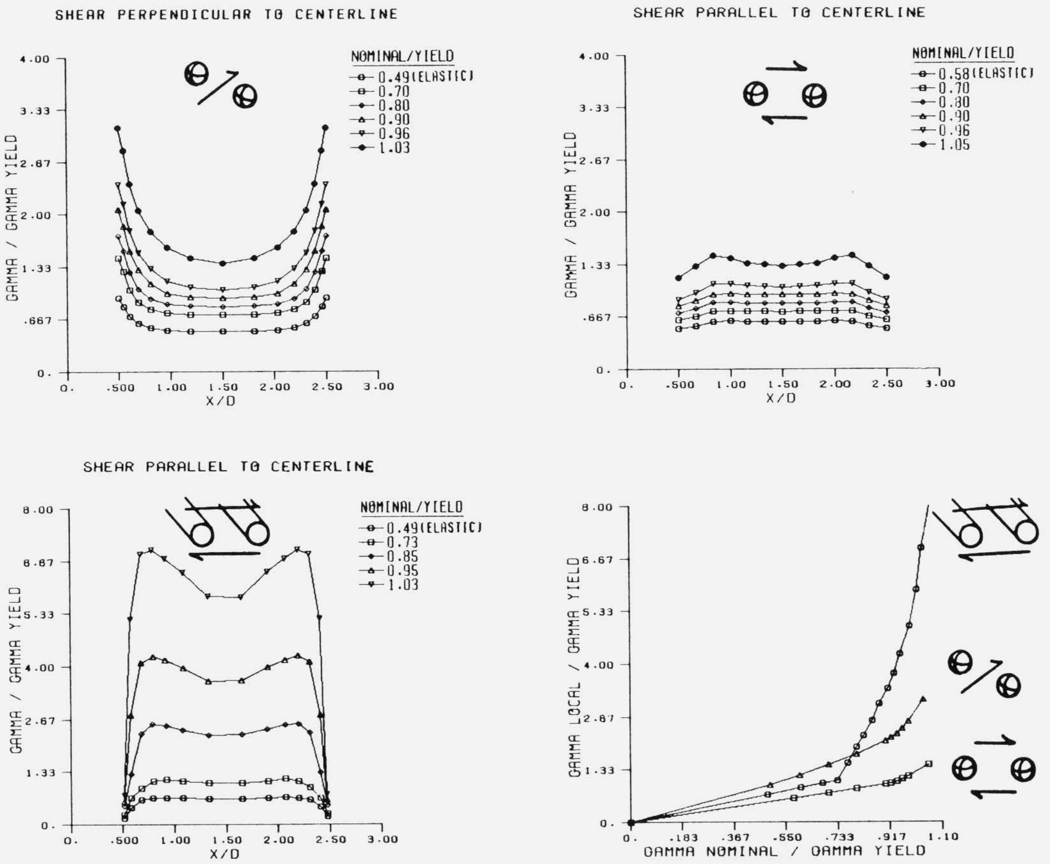

Figure 4. Strain variation along centerline for the spherical void problems (top) and cylindrical void problem (bottom left). In bottom right, peak local strain is plotted versus nominal strain.

3/4 of a radius from the surfaces and strain levels roughly 30% over the nominal strain.

The cylindrical void pair analysis shows strain amplification levels greatly exceeding those found in the spherical void analyses. For this plane strain case, the mesh refinement was adequate to capture the shear free conditions at x= 0.5 D and 2.5 D. There is interaction from the beginning of loading in this case. The elastic data indicate a near uniform state over the centerline with a magnitude roughly 50% higher than the nominal value. When the ligament and void surface plastic zones link, distinct maxima develop at positions roughly 3/4 of a void radius from the surfaces. At general yield, the local strain level greatly exceeds nominal. For instance, at 1.03 times yield, the mid-ligament strain is 5.6 and the maximum is 7.0 times the material's yield strain.

The comparison plot in the bottom right of Figure 4 consists of curves for the variation of the peak strain on each pair centerline as a function of applied shear for the three problems. In the early stages of applied shear, when the plastic zones are small, the spherical voids oriented perpendicular to the load is the most severe case with the highest levels of strain intensification. This is the most severe orientation of the two 3D cases throughout loading, both as regards strain and strain rate levels. Once plastic zone size becomes significant, the cylindrical void pair develops strain which greatly exceeds that found for the 3D problems. For this plane strain case, strain rate intensification reaches a value of 30 at general yield. Smaller strain rate values were found for the 3D cases, as suggested by the slopes of the curves plotted.

The void pair analyses obviously have neglected the presence of nucleating particles, and thus are applicable to the study of post nucleation effects resulting from the creation of interior traction free surfaces. The effect of perfectly bonded elastic spherical particles was studied by performing an elastic-plastic finite element analysis which modeled particles as elastic with infinite yield strength and a modulus twice that of the elastic modulus of the elastic-plastic matrix in which they reside. As in the void pair analyses, a particle pair with a three diameter spacing was considered.

Figure 5 shows the strain intensification history along the particle pair centerline through each particle as well as the matrix for two nominal simple shear loading cases; shear perpendicular to the pair centerline and shear parallel to the pair centerline. The shear strains are normalized with respect to the shear yield strain of the matrix. According to the abscissae in Figure 5, the centerline passes through the inclusions at -0.5 thru 0.5 and 2.5 thru 3.5.

The left plot of Figure 5 shows the results for a remote simple shear loading perpendicular to the pair centerline. Incipient yield occurs at a nominal shear strain equal to 77% of the shear yield strain. It can be expected from Eshelby's (9) analysis of isolated ellipsoidal particles, that the strain would be near uniform in our analysis. As shown in the plot, up to a nominal shear strain of 111% of the shear yield strain, although the matrix has yielded plastically, the shear strain in both particles remains fairly uniform with magnitude below the nominal shear strain value. At incipient yield the shear strain of the particles is approximately 50% of the shear yield strain of the matrix corresponding to the modulus difference. The distribution is continuous across the particle/matrix interface, increasing to the nominal value of shear strain along the middle of the pair's centerline within one particle diameter into the matrix. As the loading progresses, the shear strain along the centerline in the matrix remains fairly uniform at a value equal to the nominal shear strain at any point in the loading. Concurrently, the shear strain along the centerline in the particles does not increase at as high a rate as the imposed nominal shear strain.

The right plot of Figure 5 displays the shear strain intensification for the case of particles oriented in the direction of the applied load. Throughout the loading the shear strain along the centerline in the inclusion is relatively uniform and has a subnominal magnitude. At incipient yield the magnitude is slightly higher than 50% of the shear yield strain of the matrix and at a load slightly greater than general yield the magnitude is approximately 70% of the shear yield strain. Across the interface the shear strain is discontinuous and jumps from a subnominal value in the particle to the maximum value found in the matrix. At incipient yield, when the nominal shear strain is 77% of the shear yield strain of the matrix, this maximum value of strain is equal to the shear yield strain of the matrix. The severe gradient shows a decrease to the nominal value of shear strain within one half of a particle radius into the matrix.

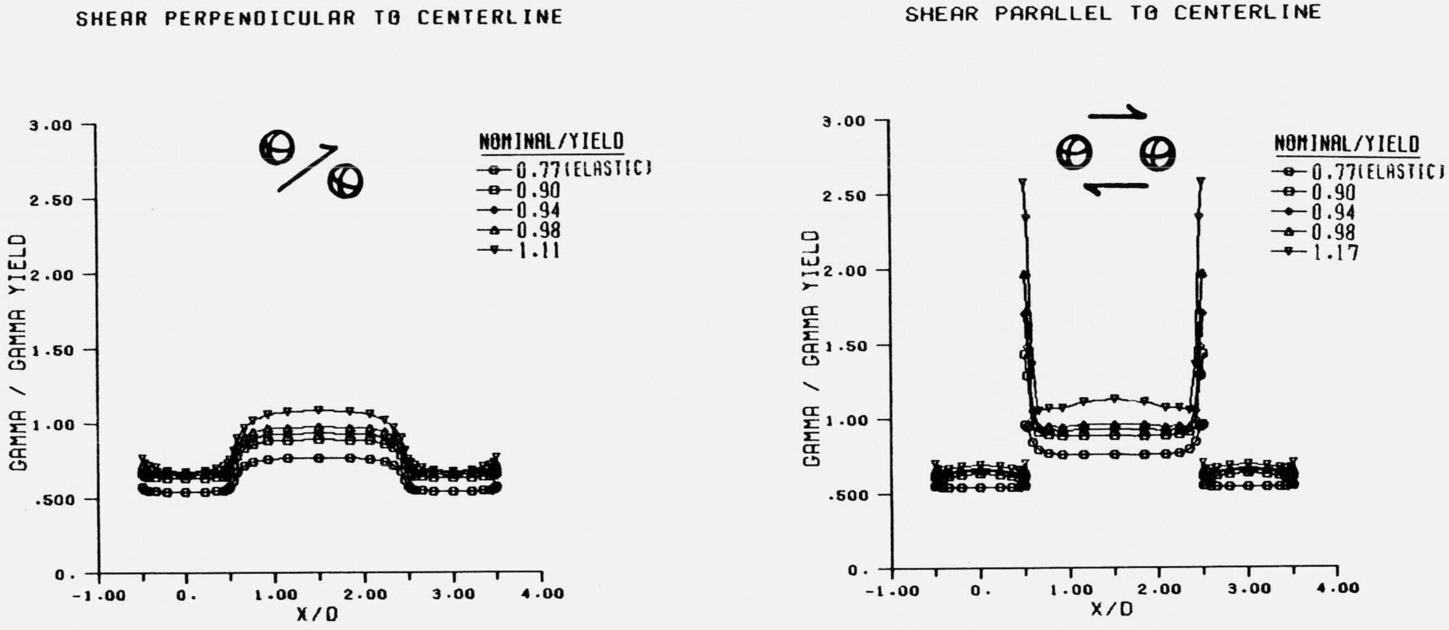

Figure 5. Strain distributions within elastic spherical particles and elastic-plastic matrix for shear loadings perpendicular and parallel to pair centerline. Distributions are plotted for nominal strain levels from incipient to general yield.

As loading progresses, the shear strain rate intensifies on the matrix side of the interface corresponding to the occurrence of extensive plastic deformation.

SUMMARY

Results have been presented for the three-dimensional aspects of interaction of pairs of voids and particles in shear. While the work has been motivated by metallurgical needs, particularly the need to develop microstructures for the delay of void nucleation, clearly, much remains to be done to guide alloying from a mechanics basis. Past mechanics research on void effects in metals has concentrated on triaxial fields. The work of Gurson (10) resulted in constitutive equations, including yield criterion and flow rule, for materials which dilate from the void growth mechanism. Hutchinson and Tvergaard (11) and Needleman (12) have considered issues of nucleation, the former treating post-nucleation particle interference and the latter treating the interface decohesion problem. These works were pursued within the model of a periodic arrangement of spherical inhomogeneities under axisymmetric loadings.

Future work on pair interaction in shear must address the spacing issue and a more complete assessment of orientation effects. Ultimately, the goal is to consolidate the simulation features, so that the necessary data and methodology will be available to allow microstructural design for ultra-high strength and toughness.

ACKNOWLEDGEMENTS

The authors acknowledge many informative metallurgical and simulation discussions with Prof. Greg Olson and the guidance provided by Colin Freese concerning the computer simulations.

REFERENCES

1. D.M. Tracey and C.E. Freese, "Adaptive Load Incrementation in Elastic-Plastic Finite Element Analysis," Computers and Structures, Vol. 13, 1981, pp. 45-53.

2. T.B. Cox and J.R. Low, Jr., "An Investigation of The Plastic Fracture of AISI 4340 and 18 Nickel-200 Grade Maraging Steels, "Metallurgical Transactions, Vol. 5, 1974, pp. 1457-1470.

3. H.C. Rogers, "The Tensile Fracture of Ductile Metals." Transaction of The Society of AIME, Vol. 218, 1960, pp. 498-506.

4. J.G. Cowie, M. Azrin, and G.B. Olson, "Microvoid Formation During Shear Deformation of Ultrahigh Strength Steels," Innovations in Ultrahigh-Strength Steel Technology, Proceedings of the 34th Sagamore Army Materials Research Conference, 1987.

5. J.R. Rice and D.M. Tracey, "On The Ductile Enlargement of Voids in Triaxial Stress Fields," Journal of the Mechanics and Physics of Solids, Vol. 17, 1969, pp. 201-217.

6. D.M. Tracey and C.E. Freese, "A Variable Load Stop Solution Approach for Incremental Tangent Modulus Finite Element Analysis," AMMRC TR 79-47, 1979.

7. V. Nagpal, F.A. McClintock, C.A. Berg, and M. Subudhi, "Traction-Displacement Boundary Conditions For Plastic Fracture by Hole Growth," Foundations of Plasticity, Nordhoff, Leyden, 1973, pp. 365-385.

8. A.E.H. Love, A Treatise on the Mathematical Theory of Elasticity, 4th ed., Dover Publications, New York, 1944.

9. J.D. Eshelby, "The Determination of the Elastic Field of an Ellipsoidol Inclusion, and Related Problems," Proceedings of the Royal Society, A241, 1957, p. 376.

10. A.L. Gurson, "Continuum Theory of Ductile Rupture Void Nucleation and Growth: Part I Yield Criteria and Flow Rules for Porous Ductile Materials, "Journal of Engineering Materials and Technology, Vol. 99, 1977, pp. 2-15.

11. J.W. Hutchinson and V. Tvergaard, "Effect of Particle-Void Interaction on Void Growth in Tension and Shear, "Innovations in Ultrahigh-Strength Steel Technology, Proceedings of the 34th Sagamore Army Materials Research Conference, 1987.

12. A. Needleman, "A Numerical Study of Void Nucleation at Carbides, "Innovations in Ultrahigh-Strength Steel Technology, Proceedings of the 34th Sagamore Army Materials Research Conference, 1987.

A NUMERICAL STUDY OF VOID NUCLEATION AT CARBIDES

ALAN NEEDLEMAN Division of Engineering, Brown University, Providence RI 02912

INTRODUCTION

Void nucleation from inclusions and second phase particles is a key factor in setting ductility and toughness limits for a wide range of steels. There is, therefore, considerable interest in a quantitative characterization of the nucleation process. Large inclusions, such as sulfides, tend to nucleate at rather low strains, often by particle cracking. The smaller carbide particles generally nucleate later in the deformation history and by decohesion of the particle-matrix interface rather than by particle cracking. Senior, Noble and Eyre (1) have recently documented the nucleation of microvoids at carbide particles (mean diameter of order 0.1 μm) in a 9 Cr$-$1 Mo steel subject to uniaxial tension and the calculations here are related to their observations.

Theoretical descriptions of void nucleation from second phase particles have been developed based on both continuum and dislocation concepts, e.g. Brown and Stobbs (2), Argon, Im and Safoglu (3), Chang and Asaro (4), Goods and Brown (5), Fisher and Gurland (6), Hutchinson and Tvergaard (7) and Needleman (8). The analyses here are based on the continuum model for void nucleation by interface decohesion introduced in (8) and used by Nutt and Needleman (9) to analyze void nucleation at fiber ends in Al-SiC composites. Within this framework, constitutive relations are specified independently for the matrix, the inclusion and the interface. The constitutive equation for the interface is such that, with increasing interfacial separation, the traction across the interface reaches a maximum, decreases and eventually vanishes so that decohesion occurs. Since the mechanical response of the interface is specified in terms of both a critical interfacial strength and the work of separation per unit area, dimensional considerations introduce a characteristic length.

As in (8), the specific boundary value problem analyzed is one simulating a periodic array of rigid spherical inclusions in an isotropically hardening elastic-viscoplastic matrix. Material properties representative of the 9 Cr$-$1 Mo steel studied experimentally by Senior et al. (1) are used. The aggregate is subject to both axial and radial stresses and a circular cylinder surrounding each inclusion is required to remain cylindrical throughout the deformation history in order to simulate the constraint of the surrounding material. In the present calculations, the ratio of radial to axial stress is specified to give a history of stress triaxiality much like that in the center of a necked round tensile bar.

INTERFACE MODEL

The analyses are based on the continuum model for void nucleation by interface decohesion introduced in (8), but here the presentation is specialized to consideration of rigid inclusions and axisymmetric deformation fields. Unit vectors normal and tangential to the inclusion in the reference configuration are introduced. The displacement of a matrix material point initially along the interface is resolved into components by

$$u_n = \mathbf{n} \cdot \mathbf{u} \ , \ u_t = \mathbf{t} \cdot \mathbf{u} \tag{2.1}$$

and

$$T_n = \mathbf{n} \cdot \mathbf{T} \ , \ T_t = \mathbf{t} \cdot \mathbf{T} \tag{2.2}$$

where **T** is the nominal traction vector (force per unit reference area).

The interfacial tractions are derived from a potential, which is taken to depend only on the displacement difference across the interface. In the circumstances on which attention is focussed here, the rigid inclusion is constrained from undergoing a rigid body motion so that u_n and u_t are components of the displacement difference across the interface. Positive u_n corresponds to increasing interfacial separation and negative u_n corresponds to decreasing interfacial separation. Note that negative u_n does not necessarily imply interpenetration since the inclusion and matrix do not need to be regarded as being in contact in the initial state.

As the interface separates, the magnitude of the tractions increases, achieves a maximum, and ultimately falls to zero when complete separation occurs. The magnitude of the tractions is taken to increase monotonically for negative u_n. Relative shearing across the interface leads to the development of shear tractions, and the dependence of the shear tractions on u_t is taken to be linear. The specific potential function used is

$$\begin{aligned}\phi(u_n, u_t) = \frac{27}{4}\sigma_{max}\delta\Big\{\frac{1}{2}\left(\frac{u_n}{\delta}\right)^2 \left[1 - \frac{4}{3}\left(\frac{u_n}{\delta}\right) + \frac{1}{2}\left(\frac{u_n}{\delta}\right)^2\right] \\ + \frac{1}{2}\alpha\left(\frac{u_t}{\delta}\right)^2 \left[1 - 2\left(\frac{u_n}{\delta}\right) + \left(\frac{u_n}{\delta}\right)^2\right]\Big\}\end{aligned} \tag{2.3}$$

for $u_n \leq \delta$, where σ_{max} is the maximum traction carried by the interface undergoing a purely normal separation ($u_t \equiv 0$), δ is a characteristic length and α specifies the ratio of shear to normal stiffness of the interface. When $u_n > \delta$, $\phi \equiv \phi_{sep}$, where ϕ_{sep} is the work of separation.

The interfacial tractions are obtained by differentiating (2.3) to give

$$T_n = \frac{-27}{4}\sigma_{max}\left\{(\frac{u_n}{\delta})\left[1-2(\frac{u_n}{\delta})+(\frac{u_n}{\delta})^2\right]+\alpha(\frac{u_t}{\delta})^2\left[(\frac{u_n}{\delta})-1\right]\right\} \tag{2.4}$$

$$T_t = \frac{-27}{4}\sigma_{max}\left\{\alpha(\frac{u_t}{\delta})\left[1-2(\frac{u_n}{\delta})+(\frac{u_n}{\delta})^2\right]\right\} \tag{2.5}$$

for $u_n \leq \delta$ and $T_n \equiv T_t \equiv 0$ when $u_n > \delta$.

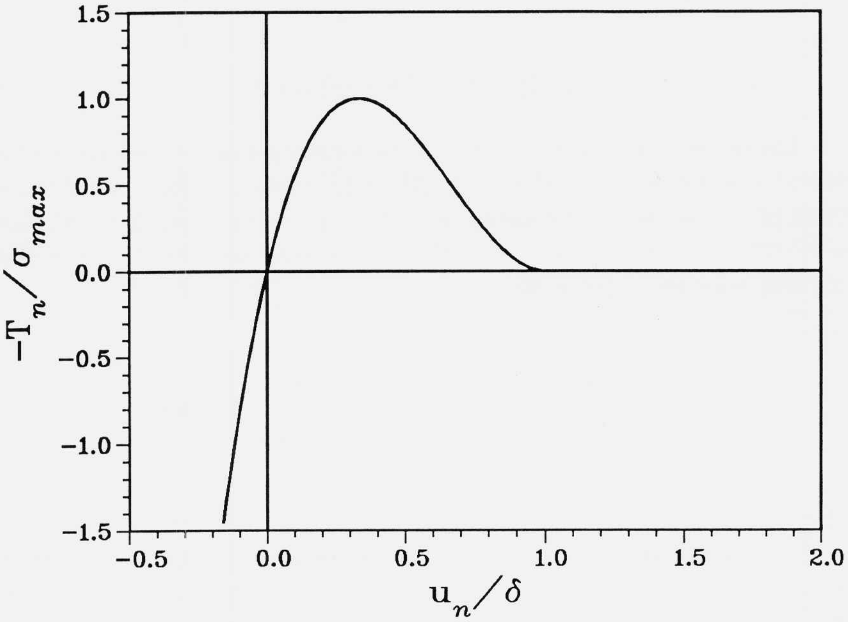

FIGURE 1. Normal traction across the interface as a function of u_n with $u_t \equiv 0$.

The motivation for choosing a potential of the form (2.3) is to obtain a response of the type shown in Fig. 1 where the normal traction, T_n, is plotted as a function of u_n with $u_t \equiv 0$. The particular functional form (2.4) was chosen for analytical convenience; other forms can readily be used in the present framework. As can be seen in Fig. 1, the maximum interfacial stress is achieved at $u_n = \delta/3$ and complete separation occurs when $u_n = \delta$. The work of separation (in Fig. 1, the area under the curve between $u_n = 0$ and $u_n = \delta$) is $\phi_{sep} = 9\sigma_{max}\delta/16$. Even when $u_t \not\equiv 0$, T_n and T_t vanish when $u_n = \delta$ so that, in general, δ serves as a characteristic length. Due to the existence of a potential, the work of separation is independent of the separation path and can be regarded as defining the characteristic interface length δ by

$$\delta = 16\phi_{sep}/9\sigma_{max} \tag{2.6}$$

Although δ has dimensions of length, it does not necessarily correspond to any physical distance.

It is convenient to regard the interface as being characterized by the three parameters σ_{max}, δ, and α, although δ is derived from ϕ_{sep} via (2.6).

PROBLEM FORMULATION

A Lagrangian convected coordinate formulation is used with the initial unstressed state taken as reference. All field quantities are considered to be functions of convected coordinates, x^i, which serve as particle labels, and time t. For quasi-static deformations with body forces neglected, the principal of virtual work can be written as

$$\int_V \tau^{ij}\delta E_{ij}dV + \int_{S_{int}} \delta\phi dS = \int_{S_{ext}} T^i \delta u_i dS \tag{3.1}$$

Here, τ^{ij} are the contravariant components of Kirchhoff stress ($\boldsymbol{\tau} = J\boldsymbol{\sigma}$, with $\boldsymbol{\sigma}$ the Cauchy stress) on the deformed convected coordinate net, V, S_{ext} and S_{int} are the total volume (inclusion plus matrix), external surface and interfacial surface, respectively, of the body in the reference configuration, and

$$T^i = (\tau^{ij} + \tau^{kj}u^i_{,k})\nu_j \tag{3.2}$$

$$E_{ij} = \frac{1}{2}(u_{i,j} + u_{j,i} + u^k_{,i}u_{k,j}) \tag{3.3}$$